Investigations of Quantum Materials: from Topological Insulators to High Temperature Superconductors

A Dissertation presented

by

Ruidan Zhong

to

The Graduate School

in Fulfillment of the

Requirements

for the Degree of

Doctor of Philosophy

in

Materials Science and Engineering

Stony Brook University

August 2017

Stony Brook University

The Graduate School

Ruidan Zhong

We, the dissertation committee for the above candidate for the

Doctor of Philosophy degree, hereby recommend

acceptance of this dissertation

Genda Gu – Dissertation advisor
Adjunct Professor, Materials Science & Chemical Engineering Department
Senior Physicist, Brookhaven National Laboratory

John M. Tranquada – Dissertation advisor
Adjunct Professor, Materials Science & Chemical Engineering Department
Senior Physicist, Brookhaven National Laboratory

T. A. Venkatesh – Chairman of Defense
Associate Professor, Materials Science & Chemical Engineering Department

Weiguo Yin
Physicist, Brookhaven National Laboratory

This dissertation is accepted by the Graduate School

Charles Taber
Dean of the Graduate School

Abstract of the Dissertation

Investigations of Quantum Materials: from Topological Insulators to High Temperature Superconductors

by

Ruidan Zhong

Doctor of Philosophy

in

Materials Science and Engineering

Stony Brook University

2017

In this dissertation, I present experimental investigations on two types of quantum materials – topological insulators and high temperature superconductors. First, I investigated the indium substitution effect on the topological crystalline insulator $\mathrm{Pb}_{1-x}\mathrm{Sn}_x\mathrm{Te}$ family, and found the indium doping leads to significant changes in the superconducting and topological properties. To understand the nature of the indium-induced superconductivity, inelastic neutron scattering was applied to study the anomalies in the phonon density of states in $(\mathrm{Pb}_{0.5}\mathrm{Sn}_{0.5})_{1-y}\mathrm{In}_y\mathrm{Te}$ powders, and the results indicate the bulk superconductivity in indium doped $\mathrm{Pb}_{1-x}\mathrm{Sn}_x\mathrm{Te}$ compounds is driven by phonons, suggesting that they are more likely conventional BCS superconductors instead of topological superconductors. Second, inelastic neutron scattering was used to explore dynamic structural and electronic correlations in the strongly correlated electronic systems of $La_{1.875}Ba_{0.125}CuO_{4+\delta}$ and $La_{1.75}Sr_{0.25}NiO_{4+\delta}$. $La_{2-x}Ba_{x}CuO_{4+\delta}$ is a family of high temperature superconductors, but with 1/8 Ba-doping, the three-dimensional superconductivity is mostly suppressed due to the formation of ordered, static stripes. The static nature is caused by pinning due to the tilting of the CuO_6 octahedra, whose symmetry resembles that of the low-temperature-tetragonal (LTT) phase. To resolve a long-standing dispute on the tilt correlations in the disordered state, I explored the tilting patterns above the transition between the low-temperature-orthorhombic (LTO) and LTT phases in $La_{1.875}Ba_{0.125}CuO_{4+\delta}$, and found the dynamic LTT-like correlations exist even at high temperature. The $La_{2-x}Sr_{x}NiO_{4+\delta}$ materials have a similar stripe structure, and their insulating nature facilitates studying their dynamic stripes. In $La_{1.75}Sr_{0.25}NiO_{4+\delta}$, the anisotropic low-energy dispersion above the stripe-ordering transition has been observed for the first time, providing evidence for the presence of electronic nematic order. With our experiments on these two materials, dynamic correlations related to high temperature superconductors are studied from two aspects: the structural view, obtained from studying the LTT-like tilt fluctuations above the LTO-LTT transition in $La_{1.875}Ba_{0.125}CuO_{4+\delta}$; and the electronic view, obtained from studying dynamic charge stripes above the stripe-ordering transition in $La_{1.75}Sr_{0.25}NiO_{4+\delta}$.

Contents

List of Figures

List of Tables

Acknowledgements

The completion of this dissertation is thanks in large part to the special people who encouraged, inspired, and supported me along the way. First and foremost, I am tremendously fortunate to have Dr. Genda Gu and Dr. John M. Tranquada as my supervisors, whose expertise, understanding, generous guidance and support made it possible for all my accomplishments on my way growing as a junior researcher in the area of condensed matter physics and materials science. Dr. Gu is a renowned crystal grower, with whom I fortunately get the valuable opportunities to learn large single-crystal growth as well as sample characterizations. Dr. Tranquada is a respected and experienced neutron scatterer and taught me about all the neutron scattering skills and knowledge in condensed matter physics with great patience. During the past five years working in the neutron scattering group at Brookhaven National Laboratory, I developed my interest on exploring the mystery of superconductors, inspired by the enthusiasm and rigorous attitude on research from my two great supervisors, which will benefit me for the rest of my life.

I would like to thank all my brilliant and talented colleagues in our neutron scattering group. Dr. John Schneeloch, who has been my officemate in the past years, generously gave me lots of help with experiments and great suggestions on physics based on his abundant knowledge. We have been working together on many projects and experienced a wonderful time. Professor Jinsheng Wen and Dr. Zhijun Xu, who were both former members in our group at BNL, helped and taught me a lot about neutron scattering experiments. They have also been greatest models for me to follow when I am perusing my academic career. I wish to thank other group members, Dr. Stephen Shapiro, Dr. Igor Zaliznyak, Dr. Guangyong Xu and Dr. Markus Hücker, whose help and support were essential during my hours in the lab. I thank Kim Mohanty, Ed Stein for providing technical assistance to our group. I also appreciate all the efficient assistance and support from the group secretaries, Eileen Levine, Arlene Rememter and Sarah Peters, who are all very nice friends of mine.

I am grateful to all my collaborators in other groups at BNL: Advanced Energy Materials group, Dr. Qiang Li, Dr. Xiaoya Shi, Dr. Cheng Zhang, and Dr. Hang Chi; Condensed Matter Theory group, Dr. Wei Ku, Dr. Xugang He, and Dr. Weiguo Yin; X-ray Scattering group, Dr. Emil Bozin, Dr. Mark Dean, Dr. Yue Cao and Dr. Hu Miao. I always seek guidance from these experts and benefited from their expertise. I also want to thank all the instrument scientists in the neutron research facilities at Oak Ridge National Laboratory, Dr. Barry Winn, Dr. Matthew Stone, Ms. Melissa K. Graves-Brook, Dr. Masaaki Matsuda, and Dr. Wei Tian, whose help with great patience was indispensable during all my neutron scattering experiments.

The last but not least, I would thank my family. Words can not express how grateful I am to my parents and parents-in-law for all of their sacrifices they have made in my behalf. Without their unconditional love and support all these years, I would not be able to go this far and finish my PhD study. A special thank to my beloved husband, Hongfei Li. I really appreciate his love, support and understanding for everything, and especially I can not thank enough for encouraging me throughout this experience. I would like to thank all my dear friends I met in the United States, who helped me make it through all these years far away from my homeland.

I dedicate this thesis to
my family, my husband Hongfei,
for their constant support and unconditional love.
I love you all dearly.

Selected Publications

- Ruidan Zhong, Barry Winn, Genda Gu, Dmitry Reznik, and John Tranquada. “Evidence for a nematic phase in $La_{1.75}Sr_{0.25}NiO_{4+\delta}$". *Physical Review Letter*, 118,177601 (2017)
- Ruidan Zhong, John Schneeloch, Qiang Li, Wei Ku, John Tranquada and Genda Gu. “Indium substitution effect on the topological crystalline insulator family $(Pb_{1-x}Sn_x)_{1-y}In_yTe$: Topological and superconducting properties". *Crystals* 7, 55, (2017) special issue: Topological Crystalline Insulators: Current Progress and Prospects. (Invited paper)
- R.D. Zhong, X.G. He, J.A. Schneeloch, C. Zhang, T.S. Liu, I. Pletikosic, T. Yilmaz, B. Sinkovic, Q. Li, W. Ku, T. Valla, J.M. Tranquada, G.D.Gu. “Surface-state-dominated transport in crystals of the topological crystalline insulator In-doped $Pb_{1-x}Sn_xTe$". *Physical Review B*, 91,195321 (2015)
- J.H. Wang* , R.D. Zhong* , S.C. Li, Y. Gan, Z.J. Xu, C. Zhang, T. Ozaki, M. Matsuda, Y. Zhao, Q. Li, G.Y. Xu, G.D. Gu, J.M. Tranquada, R.J. Birgeneau, J.S. Wen. “Substitution of Ni for Fe in superconducting $Fe_{0.98}Te_{0.5}Se_{0.5}$ depress the normal-state conductivity but not the magnetic spectral weight". *Physical Review B*, 91, 014501 (2015) (* The authors contributed equally to this work.)
- R.D. Zhong, J.A. Schneeloch, T.S. Liu, F.E. Camino, J.M. Tranquada, G.D.Gu. “Superconductivity induced by In substitution into topological crystalline insulator $Pb_{0.5}Sn_{0.5}Te$". *Physical Review B*, 90, 020505(R) (2014)

- R.D. Zhong, J.A. Schneeloch, X.Y. Shi, Z.J. Xu, C. Zhang, J.M. Tranquada, Q. Li, G.D. Gu. “Optimizing the superconducting transition temperature and upper critical field of $Sn_{1-x}In_xTe$". *Physical Review B*, 88, 020505(R) (2013)

- Q. Li, D.E. Kharzeev, C. Zhang, Y. Huang, I. Pletikosic, A.V. Fedorov, R.D. Zhong, J.A. Schneeloch, G.D. Gu, T. Valla. “Chiral magnetic effect in $ZrTe_5$". *Nature Physics*, 12, 550 (2016)

- S.J. Cho, B. Dellabetta, R.D. Zhong, J. Schneeloch, T.S. Liu, G.D. Gu, M.J. Gilbert, N. Mason. “Aharonov-Bohm oscillations in a quasi-ballistic three-dimensional topological insulator nanowire". *Nature Communications*, 6, 7634 (2015)

- I. Lee, C.K. Kim, J. Lee, S.J.L. Billinge, R.D. Zhong, J.A. Schneeloch, T.S. Liu, T. Valla, J.M. Tranquada, G.D. Gu. “Imaging Dirac-mass disorder from magnetic dopant atoms in the ferromagnetic topological insulator $Cr_x(Bi_{0.1}Sb_{0.9})_{2-x}Te_3$". *Proceedings of the National Academy of Sciences of the United States of America*, 112, 1316 (2015)

- A. Kogar, S. Vig, A. Thaler, M.H. Wong, Y. Xiao, D. Reig-i-Plessis, G.Y. Cho, T. Valla, Z. Pan, J. Schneeloch, R. Zhong, G.D. Gu, T.L. Hughes, G.J. MacDougall, T.C. Chiang, P. Abbamonte. “Surface collective modes in the topological insulators Bi_2Se_3 and $Bi_{0.5}Sb_{1.5}Te_{3-x}Se_x$". *Physical Review Letters*, 115, 257402 (2015)

- E.S. Bozin, R.D. Zhong, K.R. Knox, G.D. Gu, J.P. Hill, J.M. Tranquada, S.J.L. Billinge. “Reconciliation of local and long-range tilt correlations in underdoped $La_{2-x}Ba_xCuO_4$ ($0\leq x \leq 0.155$)". *Physical Review B*, 91, 054521 (2015)

- S. Benhabib, A. Sacuto, M. Civelli, I. Paul, M. Cazayous, Y. Gallais, M.A. Measson, R.D. Zhong, J. Schneeloch, G.D. Gu, D. Colson, A. Forget. “Collapse of the normal-state pseudogap at a Lifshitz transition in the $Bi_2Sr_2CaCu_2O_{6+\delta}$ cuprate superconductor". *Physical Review Letters*, 114, 147001 (2015)

- Y.F. Lv, W.L. Wang, J.P Peng, H. Ding, Y. Wang, L.L. Wang, K. He, S.J. Ji, R.D. Zhong, J. Schneeloch, G.D. Gu, C.L. Song, X.C. Ma, Q.K. Xue. “Mapping the electronic structure of each ingredient oxide layer of high Tc cuprate superconductor $Bi_2Sr_2CaCu_2O_{6+\delta}$". *Physical Review Letters*, 115, 237002 (2015)

- D. Fobes, I.A. Zaliznyak, Z.J. Xu, R.D. Zhong, G.D. Gu, J.M. Tranquada, L. Harriger, D. Singh, V.O. Garlea, M. Lumsden, B. Winn. “Ferro-orbital ordering transition in iron telluride $Fe_{1-y}Te$". *Physical Review Letters*, 112, 187202 (2014)

- X.X. Xi, X.G. He, F. Guan, Z.X Liu, R.D. Zhong, J.A. Schneeloch, T.S. Liu, G.D. Gu, X. Du, Z. Chen, X.G. Hong, W. Ku, G.L. Carr. “Bulk signatures of pressure-induced band inversion and topological phase transitions in $Pb_{1-x}Sn_xSe$". *Physical Review Letters*, 113, 096401 (2014)

- E.Y. Wang, H. Ding, A.V. Fedorov, W. Yao, Z. Li, Y.F. Lv, K. Zhao, L.G. Zhang, Z.J. Xu, J. Schneeloch, R.D. Zhong, S.H. Ji, L.L. Wang, K. He, X.C. Ma, G.D. Gu, H. Yao, Q.K. Xue, X. Chen, S.Y. Zhou. “Fully gapped topological surface states in Bi_2Se_3 films induced by a d-wave high-temperature superconductor". *Nature Physics*, 9, 620 (2013)

Chapter 1

Prologue

Unveiling the mysterious characteristics and underlying mechanism of superconductivity are always interesting topics in the field of condensed matter physics. In the last ten years, the notion of “topological insulators" has created a great surge of research activities due to their distinct physical properties. Meanwhile, much effort has been made on looking for the real topological superconductors, where one hope to find the elusive Majorana fermions. There are dozens of experimental groups around the world, along with countless theorists, studying all aspects of these materials. Among them, I have worked on the indium doped topological crystalline insulator (Pb, Sn)Te system and studied the indium substitution effect on this quantum material from several aspects. Indium-induced bulk superconductivity, as well as the modified bulk electronic properties that are essential to display topological surface states are summarized in this dissertation. In addition, high temperature superconductivity, first discovered in the strong-correlated system La-Ba-Cu-O, is another major theme of research since its superconducting mechanism has not been well understood, despite the numerous research studies that have been reported in the past three decades. Clarifying the dynamic correlations in these materials provides an alternative way to understand the unconventional superconductivity. With this in mind, I present two strongly-correlated systems in this dissertation, $La_{1.875}Ba_{0.125}CuO_{4+\delta}$ and $La_{1.75}Sr_{0.25}NiO_{4+\delta}$, exploring their dynamic structural or electronic correlations in the disordered state using inelastic neutron scattering.

1.1 Topological insulators

A topological insulator, just like an ordinary insulator, has a bulk energy gap separating the conduction band from the valence band. However, the surface or edge of a topological insulator has gapless states that are protected by the time-reversal symmetry, meaning that electrons can only move along the surface or edge of the material. The topological insulator is closely related to the two-dimensional quantum Hall state, which also has unique edge states. The surface or edge states of a topological insulator lead to a conducting state with unique properties unlike any other known one- or two-dimensional electronic systems [1]. The conducting electrons arrange themselves into spin-up electrons traveling in on direction, and spin-down electrons traveling in the other [2]. In addition to their fundamental interest, these states are predicted to have special properties that could also be useful for applications of quantum computation [1].

Unlike ordinary surface states, the surface states of topological insulators are topologically protected, which means that the spin and propagation directions are locked and thus avoid the back-scattering from impurities or surface imperfections. These special properties make them useful for many applications. The exotic topological insulators are made possible because of two features of quantum mechanics: symmetry under the reversal of the direction of time; and the spin-orbit coupling, which occurs in heavy elements such as mercury and bismuth [2].

The first key experimental discovery in this field was the observation of the 2D quantum spin Hall effect in a quantum-well structure made by sandwiching a thin layer of mercury telluride (HgTe) between layers of mercury cadmium telluride ($\mathrm{Hg}_x\mathrm{Cd}_{1-x}\mathrm{Te}$) [3]. Based on the 2D quantum spin Hall effect, soon the first 3D topological insulator bismuth antimonide ($\mathrm{Bi}_x\mathrm{Sb}_{1-x}$) has been probed by the angle-resolved photoemission spectroscopy (ARPES) [4]. Similarly, bismuth telluride ($\mathrm{Bi}_x\mathrm{Te}_{1-x}$), antimony telluride ($\mathrm{Sb}_2\mathrm{Te}_3$) [5] and bismuth selenide $\mathrm{Bi}_2\mathrm{Se}_3$ [5, 6] are also found to be topological insulators with a large bulk gap and a gapless surface state consisting of a single Dirac cone. These materials are well-known semiconductors with strong spin-orbit interactions and they also have the simplest possible surface-state structure.

In 2011, Fu predicted the existence of "topological crystalline insulators" (TCIs), which is a new category of the existing topological materials. Similar to the topological insulator, where the special topological surface states are protected by the time-reversal-symmetry which is guaranteed by the strong spin-orbit coupling, the special surface states in topological crystal insulators are protected by certain crystal point group symmetries [7]. After the theory prediction, SnTe has been proved to be a TCI both theoretically [8] and experimentally [9]. Generally these materials are made of IV-VI elements and are narrow gap semiconductors with a rock-salt crystal structure. Soon people realized the related system $Pb_{1-x}Sn_xTe$ and $Pb_{1-x}Sn_xSe$ are also TCIs [10–12], as long as the Pb concentration doesn't exceed a critical point.

One of the most exciting potential applications of topological insulators is the creation of *Majorana fermions*, also referred as *Majorana particles*, which is a fermion that is its own antiparticle. The term is used in opposition to a *Dirac fermion*, which describes fermions that are not their own antiparticles. Majorana fermions can occur as quasiparticles in certain special superconductors. This is allowed because a pair of quasiparticles can form a Cooper pair and disappear into the superconductor. Thus it is of high priority in condensed matter physics to engineer a true Majorana fermion, since they are essential to realize the fault-tolerant topological quantum computer.

In 2008, Fu and Kane provided a groundbreaking development by theoretically predicting that Majorana bound states can appear at the interface between topological insulators and superconductors [13, 14]. If a superconductor is placed in contact with a topological insulator, the surface states become superconducting. Since the surface states are half an ordinary 2D electron system, their superconducting state is half an ordinary superconductor. This is indeed what is required to host Majorana fermions [2]. In the effort of looking for the candidates of topological superconductors, we studied the indium-induced superconductivity in the topological crystalline insulator $\mathrm{Pb}_{1-x}\mathrm{Sn}_x\mathrm{Te}$, which will be discussed in detail in Chapter 3.2.

Even though the basic properties of topological insulators have been established, there is still a long way to go in its development. For instance, even when there is an insulating gap in the interior, there is, in practice, always a small bulk conductivity that overwhelms the surface currents, and it is hard to separate the bulk and surface contributions to the overall current. This is a challenging problem since narrow gap semiconductors are very sensitive to doping. Our studies on the indium doped $\mathrm{Pb}_{1-x}\mathrm{Sn}_x\mathrm{Te}$ reveal a true bulk insulating topological crystalline insulator, which will be discussed in detail in Chapter 3.3.

1.2 High temperature superconductors

The discovery of high-temperature superconductivity in the copper oxides triggered a huge amount of innovative scientific research activities. In the past 30 years, much has been learned about the novel forms of quantum matter that are shown in these strongly correlated electron systems. However, there are still many unresolved issues including the superconducting mechanism, the unprecedented prominence of various forms of collective fluctuations, and those co-existing, or otherwise competing orders, due to the astonishing complexity of the electronic structure and phase diagram.

In 1986, J. G. Bednorz and K. A. Muller discovered the first superconductor with T_c higher than 30 K: lanthanum barium copper oxide (LBCO) [15], which earned them the Nobel Prize in Physics in 1987. This discovery of 30 K (high T_c relative to the predicted upper limit of T_c from BCS theory) superconductivity in the La-Ba-Cu-O system aroused great interest in seeking new superconductors with higher T_c in oxide compounds, and a series of high T_c superconductors, such as YBCO (90 K) [16], Bi-Sr-Ca-Cu-O (105 K) [17], Tl-Ba/Ca-Cu-O (120 K) [18], and $HgBa_2Ca_2Cu_3O_{8+\delta}$ under high pressure (150 K) [19] have been discovered since then.

In fact, according to the theory of “conventional" superconductors, the copper oxides would have seemed the least likely materials in which to look for superconductivity: at room temperature they are such poor conductors that they can hardly be classified as metals and if their chemical composition is very slightly changed they become highly insulating antiferromagnets. Magnetism arises from strong repulsive interactions between electrons, whereas conventional superconductivity arises from induced attractive interactions, making magnetism and superconductivity seemingly antithetical forms of order [20]. Therefore, the Bardeen-Cooper-Schrieffer (BCS) theory that works successfully to understand the conventional superconductors is no longer suitable to address many features in the copper oxide superconductors, such as the high transition temperature (T_c). Therefore, there is still a long way to go in order to unveil the mysterious origin of high temperature superconductivity.

The first theoretical description of these materials, using the resonating valence bond (RVB) theory, came up in 1987 [21]. These superconductors are now known to have a d-wave pair symmetry, which was first proposed in 1987 by Bickers, Scalapino and Scalettar [22]. It was followed by three subsequent theories using spin-fluctuation theory identifying d-wave pairing as a natural consequence of the RVB theory [23–25]. The d-wave nature of the cuprate superconductors was confirmed by a variety of experiments, including the direct observation of the d-wave nodes in the excitation spectrum through Angle Resolved Photoemission Spectroscopy (ARPES), the observation of a half-integer flux in tunneling experiments, and indirectly from the temperature dependence of the penetration depth, specific heat and thermal conductivity.

The Coulomb repulsion between electrons is amplified by the chemistry of the copper oxides. The two-dimensional copper oxide layers are separated by ionic, electronically inert, buffer layers [20]. The states formed in the CuO_2 unit cells are well localized such that it takes a large energy to remove an electron from one site and add it to another, leading to a “Mott insulator" [21]. However, even a localized electron has a spin whose orientation remains a dynamical degree of freedom. Virtual hopping of these electrons produces an antiferromagnetic interaction between neighboring spins. This leads to a simple ordered phase below room temperature, in which there are static magnetic moments on the Cu sites with a direction that reverses from one Cu to the next [26, 27].

An increasingly well-documented feature of high temperature superconductors is a tendency towards a variety of orders in addition to superconductivity, which involve ‘crystallization’ of the electrons in the form of stripes and other forms of charge order [20]. The undoped antiferromagnetic (AF) domains separated by hole-rich walls, self-organized into atomic-scale patterns with the form of *stripes* is considered as the key consequence of doping a layered transition-metal oxides. The discovery of stripe-like spin order (SO) and charge order (CO) in Nd-codoped

$La_{2-x}Sr_xCuO_4$[28, 29] gives a new perspective on understanding the nature of high T_c superconductors. The stripe order was initially found in the underdoped versions of LSCO, where a low-temperature-tetragonal (LTT) lattice deformation apparently pins the stripes [28]. Given the strong response of the electronic properties to the crystal symmetry, it is of considerable interest to understand the nature of the structural transitions in cuprates. Both powder [30, 31] and single-crystal diffraction [32, 33] studies clearly demonstrate that the transition to the low-temperature structure involves a change in tilt direction of the CuO_6 octahedra. A surprisingly different perspective is given by short-range probes such as pair-distribution-function (PDF) analysis [34] and x-ray absorption fine structure study [35], which indicate that the local structure appears to be unaffected by warming through the transition, retaining the low-temperature tilt pattern to higher temperature. In Chapter 4.2, inelastic neutron scattering studies will be presented to resolve this apparent conflict between local and long-range measures of the structural dynamics in $La_{2-x}Ba_xCuO_{4+\delta}$.

Generally, the formation of static stripes is believed to be a competitor with three-dimensional superconductivity. Evidence has emerged that materials with static stripes form a “pair density wave": the charge stripes result in planar two-dimensional superconductivity, but the phase reverses from stripe to stripe [36]. Given that the stripe orientation changes as one moves from one layer to the next, this frustrates the Josephson coupling between layers, and thus suppresses the onset of bulk superconductivity [37, 38]. Progress has been made on exploring the dynamic magnetic correlations in strongly correlated systems, and the survival of dynamic incommensurate spin stripes above the ordering temperature implies that the dynamic charge stripes correlations should play an underlying role in the high temperature superconductivity [39, 40]. Although there has been considerable experimental work characterizing the static spin and charge order of nickelates $La_2NiO_{4+\delta}$ and $La_{2-x}Sr_xNiO_{4+\delta}$ [41–43], and theoretical calculations have captured various aspects of the ground states, the situation is much less clear when one considers the state from which the stripes develop on cooling [44–48]. In this dissertation, dynamic correlations of charge stripes will be discussed in detail in Chapter 4.3.

References

[1] M. Z. Hasan and C. L. Kane. Colloquium: Topological insulators. *Rev. Mod. Phys.*, 82:3045–3067, Nov 2010.

[2] Charles Kane and Joel Moore. Topological insulators. *Physics World*, 24(02):32, 2011.

[3] B. Andrei Bernevig, Taylor L. Hughes, and Shou-Cheng Zhang. Quantum spin hall effect and topological phase transition in HgTe quantum wells. *Science*, 314(5806):1757–1761, 2006.

[4] D. Hsieh, D. Qian, L. Wray, Y. Xia, Y. S. Hor, R. J. Cava, and M. Z. Hasan. A topological Dirac insulator in a quantum spin Hall phase. *Nature*, 452(7190):970–974, 04 2008.

[5] Haijun Zhang, Chao-Xing Liu, Xiao-Liang Qi, Xi Dai, Zhong Fang, and Shou-Cheng Zhang. Topological insulators in Bi_2Se_3, Bi_2Te_3 and Sb_2Te_3 with a single dirac cone on the surface. *Nat Phys*, 5(6):438–442, 06 2009.

[6] Y. Xia, D. Qian, D. Hsieh, L. Wray, A. Pal, H. Lin, A. Bansil, D. Grauer, Y. S. Hor, R. J. Cava, and M. Z. Hasan. Observation of a large-gap topological-insulator class with a single Dirac cone on the surface. *Nat Phys*, 5(6):398–402, 06 2009.

[7] Liang Fu. Topological crystalline insulators. *Phys. Rev. Lett.*, 106:106802, Mar 2011.

[8] Timothy H. Hsieh, Hsin Lin, Junwei Liu, Wenhui Duan, Arun Bansil, and Liang Fu. Topological crystalline insulators in the SnTe material class. *Nat Commun*, 3:982, 2012.

[9] Y. Tanaka, Zhi Ren, T. Sato, K. Nakayama, S. Souma, T. Takahashi, Kouji Segawa, and Yoichi Ando. Experimental realization of a topological crystalline insulator in SnTe. *Nat Phys*, 8(11):800–803, 2012. 10.1038/nphys2442.

[10] P. Dziawa, B. J. Kowalski, K. Dybko, R. Buczko, A. Szczerbakow, M. Szot, E. Łusakowska, T. Balasubramanian, B. M. Wojek, M. H.

Berntsen, O. Tjernberg, and T. Story. Topological crystalline insulator states in $Pb_{1x}Sn_xSe$. *Nat Mater*, 11(12):1023–1027, 12 2012.

[11] Su-Yang Xu, Chang Liu, N. Alidoust, M. Neupane, D. Qian, I. Belopolski, J. D. Denlinger, Y. J. Wang, H. Lin, L. A. Wray, G. Landolt, B. Slomski, J. H. Dil, A. Marcinkova, E. Morosan, Q. Gibson, R. Sankar, F. C. Chou, R. J. Cava, A. Bansil, and M. Z. Hasan. Observation of a topological crystalline insulator phase and topological phase transition in $Pb_{1-x}Sn_xTe$. *Nat Commun*, 3:1192, 11 2012.

[12] Chenhui Yan, Junwei Liu, Yunyi Zang, Jianfeng Wang, Zhenyu Wang, Peng Wang, Zhi-Dong Zhang, Lili Wang, Xucun Ma, Shuaihua Ji, Ke He, Liang Fu, Wenhui Duan, Qi-Kun Xue, and Xi Chen. Experimental observation of Dirac-like surface states and topological phase transition in $Pb_{1-x}Sn_xTe$ (111) films. *Phys. Rev. Lett.*, 112:186801, May 2014.

[13] Liang Fu and C. L. Kane. Superconducting proximity effect and Majorana fermions at the surface of a topological insulator. *Phys. Rev. Lett.*, 100:096407, Mar 2008.

[14] Liang Fu and C. L. Kane. Josephson current and noise at a superconductor/quantum-spin-hall-insulator/superconductor junction. *Phys. Rev. B*, 79:161408, Apr 2009.

[15] J. G. Bednorz and K. A. Müller. Possible high Tc superconductivity in the Ba-La-Cu-O system. *Zeitschrift für Physik B Condensed Matter*, 64(2):189–193, 1986.

[16] M. K. Wu, J. R. Ashburn, C. J. Torng, P. H. Hor, R. L. Meng, L. Gao, Z. J. Huang, Y. Q. Wang, and C. W. Chu. Superconductivity at 93 k in a new mixed-phase Y-Ba-Cu-O compound system at ambient pressure. *Phys. Rev. Lett.*, 58:908–910, Mar 1987.

[17] Hiroshi Maeda, Yoshiaki Tanaka, Masao Fukutomi, and Toshihisa Asano. A new high-Tc oxide superconductor without a rare earth element. *Japanese Journal of Applied Physics*, 27(2A):L209, 1988.

[18] Z. Z. Sheng and A. M. Hermann. Bulk superconductivity at 120 K in the Tl-Ca/Ba-Cu-O system. *Nature*, 332(6160):138–139, 03 1988.

[19] C. W. Chu, L. Gao, F. Chen, Z. J. Huang, R. L. Meng, and Y. Y. Xue. Superconductivity above 150 K in $HgBa_2Ca_2Cu_3O_{8+\delta}$ at high pressures. *Nature*, 365(6444):323–325, 09 1993.

[20] B. Keimer, S. A. Kivelson, M. R. Norman, S. Uchida, and J. Zaanen. From quantum matter to high-temperature superconductivity in copper oxides. *Nature*, 518(7538):179–186, 02 2015.

[21] P. W. Anderson. The resonating valence bond state in La_2CuO_4 and superconductivity. *Science*, 235(4793):1196–1198, 1987.

[22] NE Bickers, DJ Scalapino, and RT Scalettar. CDW and SDW mediated pairing interactions. *International Journal of Modern Physics B*, 1(03n04):687–695, 1987.

[23] Masahiko Inui, Sebastian Doniach, Peter J. Hirschfeld, and Andrei E. Ruckenstein. Coexistence of antiferromagnetism and superconductivity in a mean-field theory of high-T_c superconductors. *Phys. Rev. B*, 37:2320–2323, Feb 1988.

[24] C. Gros, D. Poilblanc, T.M. Rice, and F.C. Zhang. Superconductivity in correlated wavefunctions. *Physica C: Superconductivity*, 153:543 – 548, 1988.

[25] Gabriel Kotliar and Jialin Liu. Superexchange mechanism and d-wave superconductivity. *Phys. Rev. B*, 38:5142–5145, Sep 1988.

[26] D. Vaknin, S. K. Sinha, D. E. Moncton, D. C. Johnston, J. M. Newsam, C. R. Safinya, and H. E. King. Antiferromagnetism in La_2CuO_{4-y}. *Phys. Rev. Lett.*, 58:2802–2805, Jun 1987.

[27] Sudip Chakravarty, Bertrand I. Halperin, and David R. Nelson. Low-temperature behavior of two-dimensional quantum antiferromagnets. *Phys. Rev. Lett.*, 60:1057–1060, Mar 1988.

[28] J. M. Tranquada, B. J. Sternlieb, J. D. Axe, Y. Nakamura, and S. Uchida. Evidence for stripe correlations of spins and holes in copper oxide superconductors. *Nature*, 375(6532):561–563, 06 1995.

[29] J. M. Tranquada, J. D. Axe, N. Ichikawa, A. R. Moodenbaugh, Y. Nakamura, and S. Uchida. Coexistence of, and competition between, superconductivity and charge-stripe order in $\mathrm{La}_{1.6-x}\mathrm{Nd}_{0.4}\mathrm{Sr}_x\mathrm{CuO}_4$. *Phys. Rev. Lett.*, 78:338–341, Jan 1997.

[30] S. J. L. Billinge, G. H. Kwei, A. C. Lawson, J. D. Thompson, and H. Takagi. Superconductivity and the low-temperature orthorhombic to tetragonal phase transition in $\mathrm{La}_{2-x}\mathrm{Ba}_x\mathrm{CuO}_4$. *Phys. Rev. Lett.*, 71:1903–1906, Sep 1993.

[31] Takashi Suzuki and Toshizo Fujita. Structural phase transition in $(\mathrm{La}_{1-x}\mathrm{Ba}_x)_2\mathrm{CuO}_{4-\delta}$. *Physica C: Superconductivity*, 159(1-2):111–116, 1989.

[32] Y. Zhao, B. D. Gaulin, J. P. Castellan, J. P. C. Ruff, S. R. Dunsiger, G. D. Gu, and H. A. Dabkowska. High-resolution x-ray scattering studies of structural phase transitions in underdoped $\mathrm{La}_{2-x}\mathrm{Ba}_x\mathrm{CuO}_4$. *Phys. Rev. B*, 76:184121, Nov 2007.

[33] M. Hücker, M. v. Zimmermann, G. D. Gu, Z. J. Xu, J. S. Wen, Guangyong Xu, H. J. Kang, A. Zheludev, and J. M. Tranquada. Stripe order in superconducting $\mathrm{La}_{2-x}\mathrm{Ba}_x\mathrm{CuO}_4$ $(0.095 \leqslant x \leqslant 0.155)$. *Phys. Rev. B*, 83:104506, Mar 2011.

[34] S. J. L. Billinge, G. H. Kwei, and H. Takagi. Local octahedral tilts in $\mathrm{La}_{2-x}\mathrm{Ba}_x\mathrm{CuO}_4$: Evidence for a new structural length scale. *Phys. Rev. Lett.*, 72:2282–2285, Apr 1994.

[35] D. Haskel, E. A. Stern, F. Dogan, and A. R. Moodenbaugh. XAFS study of the low-temperature tetragonal phase of $\mathrm{La}_{2-x}\mathrm{Ba}_x\mathrm{CuO}_4$: Disorder, stripes, and T_c suppression at $x = 0.125$. *Phys. Rev. B*, 61:7055–7076, Mar 2000.

[36] Eduardo Fradkin, Steven A Kivelson, and John M Tranquada. Colloquium: Theory of intertwined orders in high temperature superconductors. *Reviews of Modern Physics*, 87(2):457, 2015.

[37] Q. Li, M. Hücker, G. D. Gu, A. M. Tsvelik, and J. M. Tranquada. Two-dimensional superconducting fluctuations in stripe-ordered $\mathrm{La}_{1.875}\mathrm{Ba}_{0.125}\mathrm{CuO}_4$. *Phys. Rev. Lett.*, 99:067001, Aug 2007.

[38] S Tajima, T Noda, H Eisaki, and S Uchida. C-axis optical response in the static stripe ordered phase of the cuprates. *Physical review letters*, 86(3):500, 2001.

[39] S.-H. Lee, J. M. Tranquada, K. Yamada, D. J. Buttrey, Q. Li, and S.-W. Cheong. Freezing of a stripe liquid. *Phys. Rev. Lett.*, 88:126401, Mar 2002.

[40] P. Bourges, Y. Sidis, M. Braden, K. Nakajima, and J. M. Tranquada. High-energy spin dynamics in $\mathrm{La}_{1.69}\mathrm{Sr}_{0.31}\mathrm{NiO}_4$. *Phys. Rev. Lett.*, 90:147202, Apr 2003.

[41] Hans B Brom and Jan Zaanen. Magnetic ordering phenomena and dynamic fluctuations in cuprate superconductors and insulating nickelates. *Handbook of Magnetic Materials*, 15:379–496, 2003.

[42] Holger Ulbrich and Markus Braden. Neutron scattering studies on stripe phases in non-cuprate materials. *Physica C: Superconductivity*, 481:31 – 45, 2012. Stripes and Electronic Liquid Crystals in Strongly Correlated Materials.

[43] John M Tranquada, Adolfo Avella, and Ferdinando Mancini. Spins, stripes, and superconductivity in hole-doped cuprates. 1550(1):114–187, 2013.

[44] J Zaanen and PB Littlewood. Freezing electronic correlations by polaronic instabilities in doped $\mathrm{La}_2\mathrm{NiO}_{4+\delta}$. *Physical Review B*, 50(10):7222, 1994.

[45] Takashi Hotta and Elbio Dagotto. Orbital ordering, new phases, and stripe formation in doped layered nickelates. *Phys. Rev. Lett.*, 92:227201, Jun 2004.

[46] Marcin Raczkowski, Raymond Frésard, and Andrzej M. Oleś. Microscopic origin of diagonal stripe phases in doped nickelates. *Phys. Rev. B*, 73:094429, Mar 2006.

[47] Susumu Yamamoto, Takeo Fujiwara, and Yasuhiro Hatsugai. Electronic structure of charge and spin stripe order in $\mathrm{La}_{2-x}\mathrm{Sr}_x\mathrm{NiO}_4$ (x=1/3, 1/2). *Physical review B*, 76(16):165114, 2007.

[48] U. Schwingenschlögl, C. Schuster, and R. Frésard. Magnetic ordering in the striped nickelate la 5/3 sr 1/3 nio 4 : A band structure point of view. *EPL (Europhysics Letters)*, 81(2):27002, 2008.

Chapter 2

Experimental Background Information

2.1 Materials Synthesis and Characterizations

In this section, two major single crystal growth method will be mentioned – traveling solvent floating zone method and the modified floating zone method. The former method has been used to grow large-size single crystals of high temperature superconducting cuprates for neutron scattering, such as $La_{2-x}Sr_xCuO_{4+\delta}$, $La_{2-x}Ba_xCuO_{4+\delta}$, and $La_{2-x}Ca_{1+x}Cu_2O_{6+\delta}$. The later method has been used to grow single crystals of the topological crystalline insulators, indium doped SnTe and $Pb_{1-x}Sn_xTe$. The physical properties of the materials are closely related to the chemical composition and crystal structure. Thus the basic characterizations on the as-grown crystals are essential for later studies.

2.1.1 Floating zone method

The floating zone technique has been employed for crystal growth of a wide range of oxide materials, including high-temperature superconductors and new magnetic materials [1, 2]. Since the halogen lamps and ellipsoidal mirror are essential components for the floating zone (FZ) technique, it often called **optical floating zone** method. The crystal growth process performed by the optical floating zone starts by melting the tips of polycrystalline feed/seed rods, bringing them together and establishing a liquid zone called the *floating zone* between the bottom seed rod and top feed rod[3].

In this thesis, we used an improved optical floating zone method, called **traveling solvent floating zone** method, where we used a flux as a starting material to build up the initial floating zone and achieve steady growth state much faster, leading to better, more stable growth.

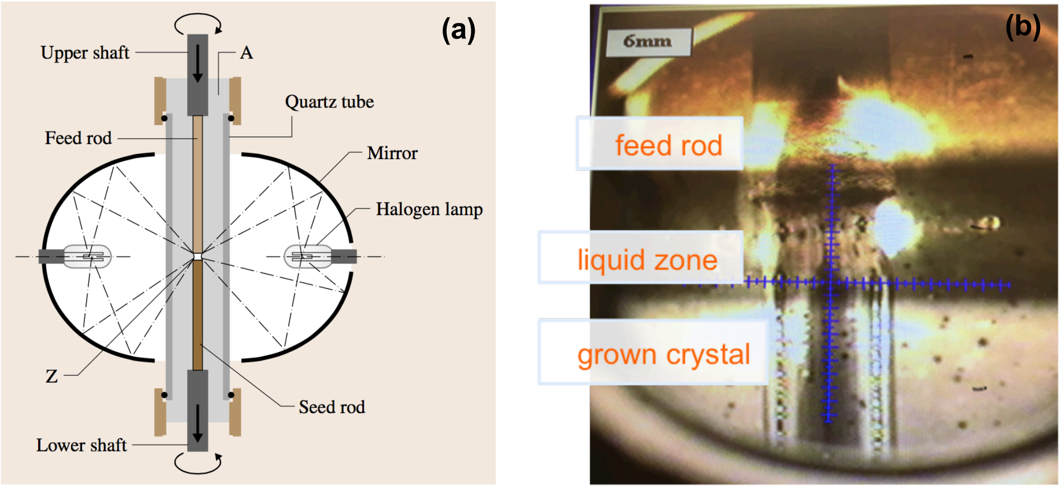

Figure 2.1: (a) Schematic diagram of optical floating zone apparatus [3]. (b) A photo of the floating zone growth of $La_{2-x}Sr_xCuO_{4+\delta}$.

After the floating zone is created, the previously aligned, feed and seed rods start moving downwards, the liquid cools and the materials eventually crystallizes on the seed rod. During growth the roads rotate in the opposite directions (typically, 30 rpm) in order to achieve a homogeneously mixed and stable liquid zone. During the growth process there are a few parameters can be adjusted from the control computer, such as the moving speed of the two rods, the lamp power, and the rotation speed. The environment (gas atmosphere, chamber pressure) of the growth can be controlled by adjusting the inlet and outlet valves. The schematic diagram of the floating zone and a photo of the growing $La_{2-x}Sr_xCuO_{4+\delta}$ crystal in the furnace are shown in Figure 2.1.

Successful preparation of the starting polycrystalline feed/seed rod is the key to stable FZ growth. Initial ingredients (*e.g.* La_2O_3, $CaCO_3$, $SrCO_3$ and CuO) are ground into fine powders, mixed together, loaded into a latex tube, and made straight and uniform. Then the latex tube is loaded into a steel rod with many holes on it, and put into a hydro-static oil press for pressing under a pressure of 60 kpsi. After the straight and compact powder rod is obtained from pressing, we hang it inside a high temperature furnace and sinter it for 72 hr at as high as a possible temperature to reduce porosity. In the meantime, the temperature should not be higher than the melting point of the feed rod to avoid repositioning of the low-melting point composition.

The greatest advantages of the FZ technique come from the fact that no crucible is necessary and that both congruently and incongruently melting materials can be grown [3]. This allows for growth of large-size single crystals for neutron scattering experiments. The typical growth velocity of the cuprates is optimized experimentally and varies from 0.4–1.0 mm/hr, thus a single crystal large enough for neutron scattering experiment usually takes a few weeks to grow. Figure 2.2 shows a photo of the as-grown cuprate $La_{1.875}Ba_{0.125}CuO_{4+\delta}$ and nickelate $La_{1.75}Sr_{0.25}NiO_{4+\delta}$, which are the crystals used in neutron experiments mentioned in Chapter 4.

There are some limitations to the growth of crystals by the FZ method. As a rule this method is not suitable for materials with high vapor pressure, low surface tension or high viscosity as well as for materials that undergo a phase transition during cooling, because such crystals usually crack after growth [4, 5]. The small volume of the liquid in the zone makes the stability of this growth method susceptible to power fluctuations and gas pressure oscillations. Together with very high thermal gradients at the liquid-solid interface this leads to difficulties in achieving and maintaining a flat crystallization front and stable growth rate, which can result in many defects and growth instabilities [6]. Thermal and mechanical stresses limit the size and quality of the obtained crystals. This problem is reduced if the post-annealing process is applied [3, 7, 8].

(a) $La_{1.875}Ba_{0.125}CuO_{4+\delta}$

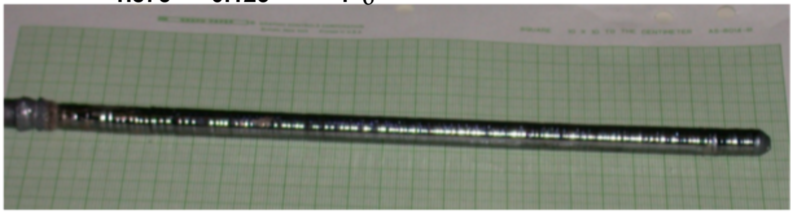

(b) $La_{1.75}Ni_{0.25}CuO_{4+\delta}$

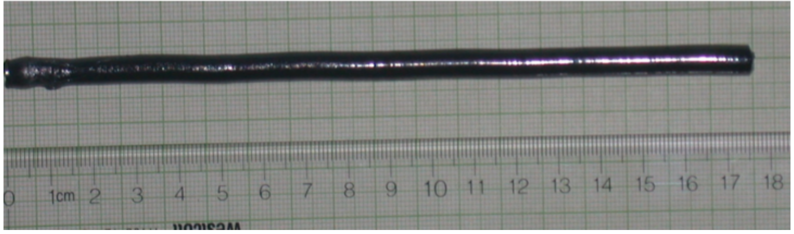

Figure 2.2: As-grown single crystals of cuprate $La_{1.875}Ba_{0.125}CuO_{4+\delta}$ (a) and nickelates $La_{1.75}Sr_{0.25}NiO_{4+\delta}$ (b).

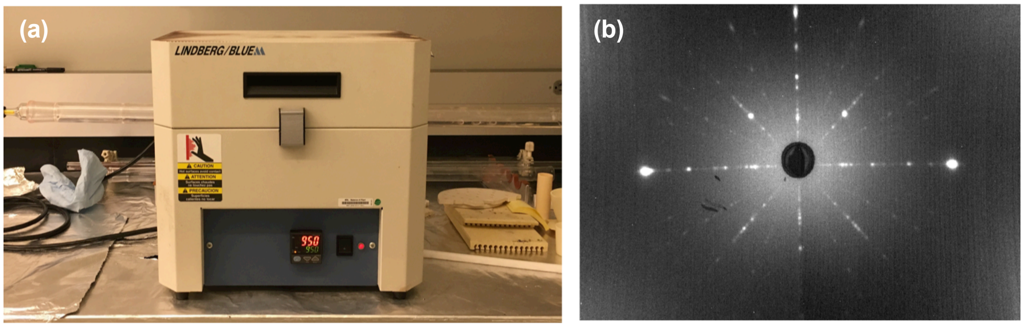

Figure 2.3: (a) Post-annealing procedure using a tube furnace. (b) Typical x-ray back-Laue diffraction pattern for the tetragonal *La-214* single crystal, with c-axis aligned in horizontal plane.

After the crystal growth, a few more procedures are sometimes necessary. Because some of the La_2O_3 has not been fully reacted and aggregates in the crystal domain boundary, the as-grown crystal (or the un-reacted La_2O_3) would gradually absorb the moisture in air and finally decompose into powders. As a result, the post annealing procedure is needed, not only to complete the solid reaction, but also to fill up the oxygen vacancies and to remove the strain in the sample. For the post annealing, the as-grown crystal is loaded into a long quartz tube, put inside a tube furnace. In the meantime, oxygen gas runs through the quartz tube and reacts with the crystal under high temperature (Figure 2.3*(a)*). Details of the domain structure of the crystal will be investigated by the X-ray back-Laue diffraction, from which we know whether or not the crystal is a single domain (Figure 2.3*(b)*). This method is also used to align the crystal with the desired crystal orientation before doing neutron scattering experiments.

2.1.2 Modified floating zone method

As mentioned in section 2.1.1, one limitation of the FZ method comes from the requirement of the materials' low vapor pressure. In preparation of the indium doped SnTe and $Pb_{1-x}Sn_xTe$ topological crystalline insulator materials, due to the high vapor pressure of element indium, the FZ technique seems unsuitable. However, traditional ceramic synthesis would result in smaller size single crystals. A possible way to grow single crystals of $(Pb_{1-x}Sn_x)_{1-y}In_yTe$ materials would be the vertical Bridgman (VB) method [9], in which the solidification takes place in a temperature gradient that cools uniformly with time. For this purpose, the Bridgman furnace has many zones that can be set with a temperature gradient to create a custom temperature profile.

Since the optical floating zone furnace we have provides a more precise thermal gradient compared to a commercial three-zone furnace, we could take advantage of the FZ furnace and adapt this technique to crystal growth of materials with high vapor pressure. The modified FZ method has lots in common with the traditional FZ technique, except that the starting materials are sealed in a quartz ampoule and fixed to the bottom shaft.

In preparation of crystals for experiments mentioned in Chapter 3, single crystal samples with nominal composition, $(Pb_{1-x}Sn_x)_{1-y}In_yTe$ (x_{norm}=0.2-0.5, 1.0, y_{norm}=0-0.5), were prepared via the vertical Bridgman method. Stoichiometric mixtures of high-purity (99.999%) elements were sealed in double-walled evacuated quartz ampoules, as shown in Figure 2.4*(a)*. The ampoules were set in a vertical position, heated at 950°C in a three-zone vertical box furnace, with rocking to achieve homogeneous mixing of the ingredients. The crystal growth took place via slow cooling from 950 to 760 °C at the rate of 1.5 °C/hr, and then the samples were gradually cooled down to room temperature over another 3 days[10]. Figure 2.4*(b)* shows examples of the resulting crystals (before removal from the quartz tubes).

For a few compositions, where we needed large crystals, we used the modified floating-zone method [11, 12]. The outer quartz tube was then removed, and the inner tube (~15 cm) together with the solidified materials would be mounted in the FZ furnace, surrounded by an atmosphere of 1 bar Ar to avoid oxygen diffusion through the quartz. During the growth, the molten zone is not in contact with any container. The solidified, cylindrical ingot was first pre-melted at a velocity of 200 mm/hr, and then crystal growth was performed at 0.5–1.0 mm/hr, so that the new crystal gradually grew from the bottom of the starting ingot, resulting in a sample such as that shown in Figure 2.4*(c)*. Because the segregation coefficient k_{sg} of In

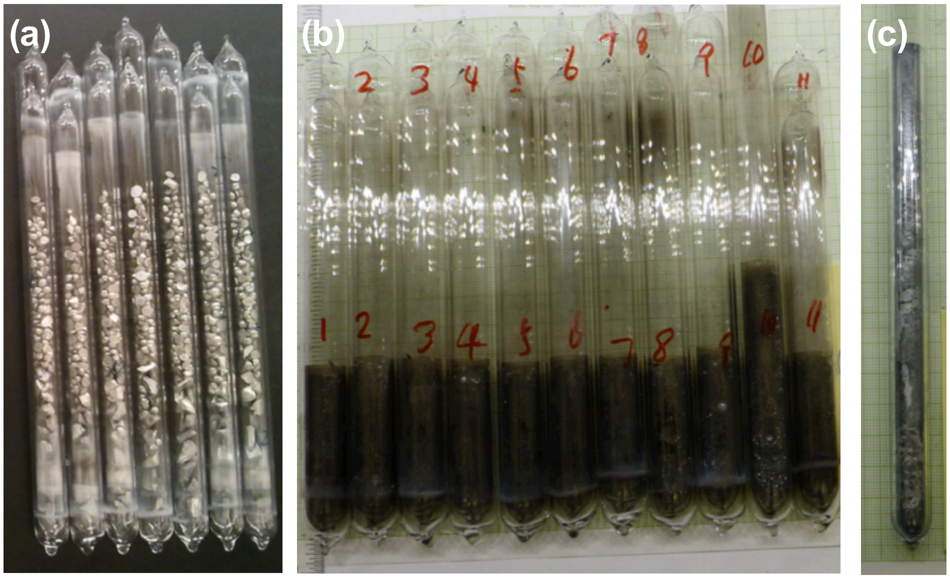

Figure 2.4: (a) Raw materials sealed in double-walled quartz ampoules. (b) Single crystal rods of $(Pb_{1-x}Sn_x)_{1-y}In_yTe$ alloy grown by vertical Bridgman method. (c) Large-size single crystal of $(Pb_{1-x}Sn_x)_{1-y}In_yTe$ grown by the modified floating zone method.

is less than 1, the In contained in the feed material would prefer to remain in the liquid zone, and thus the In concentration gradually grows with time. As a result, we anticipate an In concentration gradient along the length of the as-grown crystal rod, with a typical total length of 150 mm. To account for this, the ends of each crystal were removed and discarded; the central 100 mm was then cut into 20-mm sections. Because of the concentration distribution along the as-grown ingot, the compositional characterization is necessary for each individual sample before any further investigations.

2.1.3 Materials characterization methods

Microstructural and compositional investigations

Due to the inevitable composition gradient in the crystal growth method, identifying the chemical composition of each exact sample is important before further studies. Microstructural and compositional investigations of the crystals were performed using an analytical high-resolution scanning electron microscope (SEM) equipped for energy-dispersive x-ray spectroscopy (EDS), model JEOL 7600F, located at the Center for Functional Nanomaterials (CFN) at Brookhaven National Laboratory. For each crystal piece characterized, EDS was measured at 10 positions to get an average value of the whole sample, and the variation in the composition x was generally found to be <2% of the mean value. SEM images have also been taken to illustrate the typical microstructures of the cleaved surface.

Crystal structure

In order to identify the room-temperature crystal structures of the grown samples, single-crystal samples with known composition were ground to fine powder and investigated by X-ray diffraction, using Cu $K\alpha$ radiation from a model Rigaku Miniflex II, located at the CFN. The obtained powder diffraction patterns will then be compared with the standard Powder Diffraction File (PDF) card and to the crystal structure.

Magnetization and transport measurement

To study the effect of the superconducting properties, we performed both magnetization and resistivity measurements. The dc magnetic susceptibility measurements were performed using a commercial superconducting quantum interference device (SQUID) magnetometer (MPMS, Quantum Design), for temperatures down to 1.75 K. The sample pieces measured had an approximately cubic shape.

For the electrical resistivity measurements, nearly rectangular parallelepiped-shaped samples were prepared by polishing, with a typical geometry of 5 mm long, 1.5 mm wide, and 0.5 mm thick. Electrical resistance was measured in the standard four-probe configuration, using gold wires and silver fast-drying paint for the ohmic contact on the top side, performed with a Keithley digital multimeter (model 2001), where a Quantum Design MPMS was used for temperature control. Measurement errors due to the contact geometry were estimated to be less than 10%.

2.2 Neutron scattering

Neutron scattering is a powerful probe for studying condensed matter. Neutrons have no charge, and their electric dipole moment is either zero or too small to measure [13]. For these reasons, neutrons can penetrate matter far better than charged particles, such as electrons. Furthermore, neutrons interact with atoms through nuclear rather than electrical forces, and nuclear forces are very short range – on the order of a few femtometers. Thus, as far as the neutron is concerned, solid matter is not very dense because the size of a scattering center (i.e. nucleus) is typically 100,000 times smaller than the distance between centers. As a consequence, neutrons can travel large distances through most materials without being scattered or absorbed. Due to this advantage, much structural information can be obtained by neutron scattering, such as the changes in the crystal structure, and information on lattice vibrations.

Another unique advantage of neutron scattering compared to other scattering probes such as X-rays is that neutrons are sensitive to magnetic correlations in addition to structural correlations. Their sensitivity to magnetic moments in materials make them suitable for detecting the magnetic correlations in materials.

Besides, neutrons have a momentum-energy relation which is convenient for detecting lattice vibrations and magnetic excitation. Solids often have interesting behavior on length scales of 10^{-10}m or greater and energies in the meV range. Thermal neutrons can have the momentum necessary to probe these length scales. The relative energy resolution is also achievable to measure those common features in materials. On the contrary, X-ray scattering would require energies of at least $\approx$10 keV to be able to probe momentum transfers of several reciprocal lattice units, which means with x-rays one needs much finer δE/E in order to resolve phonons, and their relative energy resolution would be much worse compared to the neutron scattering techniques.

However, neutrons are only weakly scattered once they do penetrate, and the available neutron beams have inherently low intensities compared to synchrotron X-ray sources, which make neutron scattering a signal-limited technique. Thus large-size single crystals are needed to get meaningful data from neutron scattering experiment, which is a major constraint of this powerful technique.

In this section I will first introduce some basics of neutron scattering, and then focus on the neutron scattering of single crystals with triple-axis spectrometer and time-of-flight methods. At last, the Hybrid Spectrometer (HYSPEC) at the Spallation Neutron Source located at Oak Ridge National Laboratory will be introduced, since this instrument is the one for all three neutron experiments mentioned in this thesis.

2.2.1 Neutron scattering basics

In order to understand diffraction and scattering measurements, it is useful to establish the notations based on the reciprocal lattice of the solid. In reciprocal space, the general wave vector **Q**=(h,k,l) is in reciprocal lattice units (r.l.u) of (a^*,b^*,c^*)=(2π/a, 2π/b, 2π/c), where a, b, c are lattice constants of the crystal.

When neutrons are scattered by matter, the process can alter both the momentum and energy of the neutrons and the matter. For neutrons used in a scattering experiment, the wavelength, λ, is usually between 0.1 nm and 1 nm. In terms of the neutron wave vector, $\overrightarrow{k}$, which s a vector of magnitude 2π/λ that points along the neutron's trajectory. The magnitude of the wave vector, $\overrightarrow{k}$, is related to the neutron velocity by the equation

$$|\overrightarrow{k}| = |\mathbf{k}| = 2\pi m\nu/h, \tag{2.1}$$

where h is Plank's constant and m is the mass of the neutron.

The law of momentum and energy conservation governing all diffraction and scattering experiments are well known:

$$\mathbf{Q} = \mathbf{k}_f - \mathbf{k}_i \quad (momentum\ conservation) \tag{2.2}$$

$$|\mathbf{Q}| = k_i^2 + k_f^2 - 2k_i k_f cos\theta_s \tag{2.3}$$

$$\hbar\omega = E_i - E_f \quad (energy\ conservation). \tag{2.4}$$

In these equations, the subscript i refers to the beam incident on the sample and f the final or diffracted beam. The angle between the incident and final beams is $2\theta_s$ and the energy transferred to the sample is $\hbar\omega$. Because of the finite mass of the neutron, the dispersion relation for the neutron is :

$$E = \frac{\hbar^2 k^2}{2m_n}, \tag{2.5}$$

and the energy conservation law can be written as

$$\hbar\omega = \frac{\hbar^2}{2m_n}(k_i^2 - k_f^2). \tag{2.6}$$

When $\hbar\omega$=0 the scattering is elastic. When $\hbar\omega \neq$0 the scattering is inelastic. For $\hbar\omega$>0, the neutrons lose energy, while for $\hbar\omega$<0, the neutrons gain energy. In elastic scattering, |$\mathbf{k}_i$|=|$\mathbf{k}_f$|=k. The conservation of momentum gives:

$$\mathbf{Q} = 2ksin\theta, \tag{2.7}$$

where θ is half the angle between k_i and k_f. When the scattering meet the

(a) Elastic Scattering ($k' = k$)

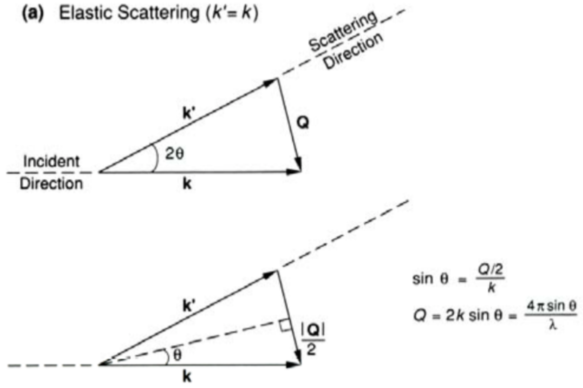

(b) Inelastic Scattering ($k' \neq k$)

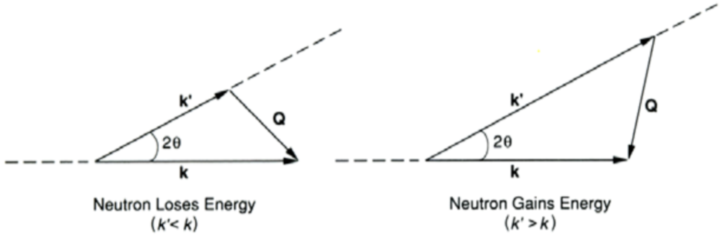

Figure 2.5: Scattering triangles are depicted for both (a) elastic scattering in which the neutron is deflected without any energy lose or gain and (b) inelastic scattering in which the neutron either loses energy or gains energy during the interaction with the sample. In both elastic and inelastic scattering, the neutron is scattered through the angle 2θ, and the scattering vector is given by the vector relationship $\mathbf{Q}$=$\mathbf{k}_f$-$\mathbf{k}_i$. For elastic scattering, simple trigonometry shows that $Q = 4\pi sin\theta/\lambda$. Figure from Ref. [13]

Bragg condition:

$$2dsin\theta = \lambda, \tag{2.8}$$

Since k=$2\pi/\lambda$ and |**Q**|=|**G**|, **G** is a reciprocal-lattice vector with **G**=$2\pi/d$, where d is the interplanar spacing. By adjusting the scattering angle θ, the energy and direction of scattered neutrons are determined.

The differential scattering cross section of monoenergetic neutrons can be obtained by Fermi's golden rule. The differential cross section of nuclear scattering can be expressed as [14]:

$$\frac{d^2\sigma}{d\Omega_f dE_f} = N\frac{k_f}{k_i}b^2S(\mathbf{Q},\omega) \tag{2.9}$$

where N is the number of unit cells, b is the scattering length and S(**Q**,ω) is the scattering function. An elegant way to write the scattering function was given by Van Hove (1954):

$$S(\mathbf{Q},\omega) = \frac{1}{2\pi\hbar N}\int_{-\infty}^{+\infty} dte^{-i\omega t}\langle\rho_{\boldsymbol{Q}}(0)\rho_{-\boldsymbol{Q}}(t)\rangle \tag{2.10}$$

where the angle brackets denote an average over configurations of time t and ρ_Q is the atomic density operator:

$$\rho_{\mathrm{Q}}(t) = \sum_l e^{i\boldsymbol{Q}\boldsymbol{r}_l(t)}. \tag{2.11}$$

The scattering function only depends on the momentum and energy transferred from neutron to the sample, and gives information on both positions and motions of atoms in the sample. Therefore, measuring $S(\mathbf{Q},\omega)$ in neutron scattering experiment can give us information of the microscopic properties of the solid system.

For elastic nuclear Bragg scattering in a Bravais lattice, the intensity I

of Bragg peaks generalizes to :

$$I(\mathbf{G}) \propto N|F_N(\mathbf{G})|^2 \tag{2.12}$$

where $F(\boldsymbol{G})$, the static **nuclear structure factor**, is given by:

$$F_N(\boldsymbol{G}) = \sum_j b_j e^{i\boldsymbol{G}\cdot\boldsymbol{d}_j} e^{-W_j} \tag{2.13}$$

where jth atom within the unit cell at position $\mathbf{d}_j$ with scattering length b_j and e^{-W_j} is the Debye-Waller factor. The crystal structure can be determined by measuring structure factor at enough reflections.

For elastic magnetic scattering from a magnetically ordered crystal, the intensity of magnetic Bragg peaks $I_M(\mathbf{G}_\mathrm{M})$ can be expressed by:

$$I_M(\boldsymbol{G}_M) \propto N_M|F_M(\boldsymbol{G}_M)|^2 \tag{2.14}$$

where N_M is the number of magnetic atoms and $F_M(\mathbf{G}_M)$ is the static **magnetic structure factor**, given by

$$F_M(\boldsymbol{G}_M) = \sum_j p_j S_{\perp j} e^{\boldsymbol{G}_M\cdot\boldsymbol{d}_j} e^{-W_j} \tag{2.15}$$

where jth magnetic atom within the unit cell at position $\mathbf{d}_j$ with magnetic scattering amplitude p_j, magnetic interaction vector $S_{\perp j}$, which is component of S perpendicular to $\mathbf{Q}$ and e^{-W_j} is the Debye-Waller factor. With crystal structure obtained above, the magnetic structure can be determined from the static magnetic structure factor.

For inelastic scattering, $S(\mathbf{Q},\omega)$ is related to the imaginary part of the dynamical spin susceptibility, $\chi''(\mathbf{Q},\omega)$ via the fluctuation-dissipation theorem,

$$S(\boldsymbol{Q},\omega) = \frac{\chi''(\boldsymbol{Q},\omega)}{1 - e^{-\hbar\omega/k_B T}} \tag{2.16}$$

where $(1 - e^{-\hbar\omega/k_B T})^{-1}$ is referred as Bose factor, or detail-balance factor.

In conclusion, by neutron scattering we can obtain information of lattice structure and magnetic structure as well as phonon and magnetic excitations in the crystals.

2.2.2 Triple-axis spectrometer and time-of-flight spectrometer

For our experiments, the two most common neutron scattering methods are the triple-axis spectrometer and the time-of-flight spectrometer, which differ according to how energy transfer is measured. Triple-axis allows one to probe nearly any coordinates in energy and momentum space in a precisely controlled manner. The three axes correspond to the axes of rotation of the monochromator, the sample, and the analyzer. The monochromator defines the direction and magnitude of the momentum of the incident beam and the analyzer performs a similar function for the scattered or final beam. Inside the large semi-cylindrical structure is the monochromator, and neutrons diffracted by it hit the sample. Those neutrons scattered by the sample are Bragg reflected by the analyzer, which lies within the white shielding. The ability to focus neutrons onto the sample with a curved monochromator provides advantages for studies concentrating on a small region of ω-**Q** space. The various components of the three-axis spectrometer are shown in Figure 2.5*(a)* [14].

In the time-of-flight (TOF) technique, a burst of polychromatic neutrons is produced, and the times taken by the neutrons to travel from the source

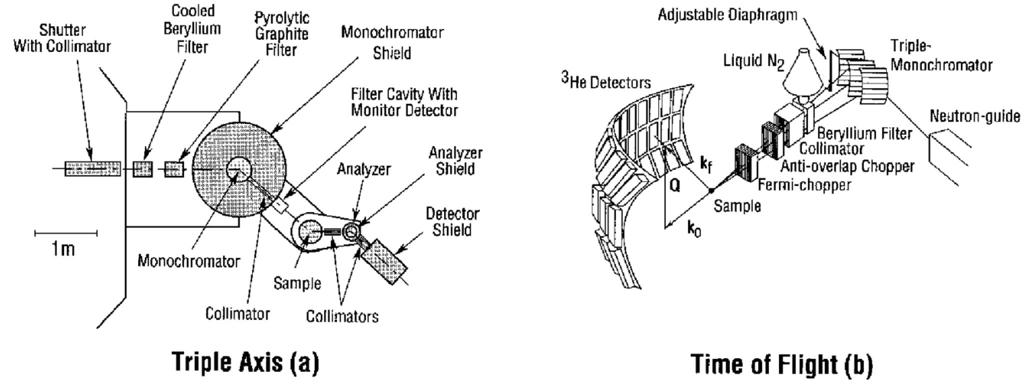

Figure 2.6: (a) Triple-axis spectrometer. (b) Time-of-flight spectrometer.

of the burst to the detector are measured. After interacting with the sample, the neutron will gain or lose energy, resulting in a velocity change. The arrival time at the detector will therefore vary (Figure 2.5*(b)*). Thus the incident beam of neutrons is shaped into monochromatic pulses of times on the order of milliseconds. The time between the pulse hitting the sample and each neutron hitting a detector determines the energy transfer. With the use of large arrays of position-sensitive detectors, it is possible to measure large regions of energy transfer, $\hbar\omega$, and momentum transfer, $\hbar\mathbf{Q}$, simultaneously. A schematic plot of the TOF spectrometer is shown in Figure 2.5*(b)* [14].

2.2.3 HYSPEC at Spallation Neutron Source at Oak Ridge National Laboratory

The neutrons used in a scattering experiment can be obtained from a nuclear reactor, where the neutrons arise from the spontaneous fission of ^{235}U, or from a spallation source, where the neutrons are produced by bombarding a heavy target (*e.g.*, U, W, Ta, Pb, or Hg) with high-energy protons [14]. In the former case, the neutrons are produced continuously in time, while in the latter, they typically come as pulses. The continuous flux is generated by high-flux reactors such as High Flux Isotope reactor (HFIR) at oak Ridge National Laboratory (ORNL) and High Flux Reactor (HFR) at the Institute Laue-Langevin (ILL). The pulsed sources neutrons are produced at the Spallation Neutron Source (SNS) at ORNL, and the pulsed beam from a spallation source is well suited to TOF techniques.

The instrument that will be described in this section is the HYbrid SPECtrometer (HYSPEC) at SNS, which is the major instrument used for this thesis work. HYSPEC is the first polarized TOF spectrometer at SNS, and provides an unprecedented range of capabilities for elastic and inelastic neutron scattering studies of novel magnetic states and excitations [15]. Traditionally, inelastic neutron experiments were carried out using triple-axis spectrometers, with narrow and collimated beams. However, much of the recent progress in neutron spectroscopic techniques has been associated with the development of TOF direct geometry chopper spectrometers at spallation sources, with large detector arrays covering a large range of scattering angles. HYSPEC is a consequence of the combination of triple-axis and the TOF techniques, which provides a wide-angle, broad-band scattered polarization analysis.

HYSPEC is a high-intensity, medium-resolution thermal neutron TOF spectrometer. For the experiment on HYSPEC, the crystal was mounted in a Displex closed-cycle cryostat. To achieve a best combination of neutron flux and energy resolution, an incident energy and a chopper frequency are chosen. For a typical measurement, the position-sensitive detector tank was placed at a particular mean scattering angle, and then measurements were collected for a series of sample orientations, involving

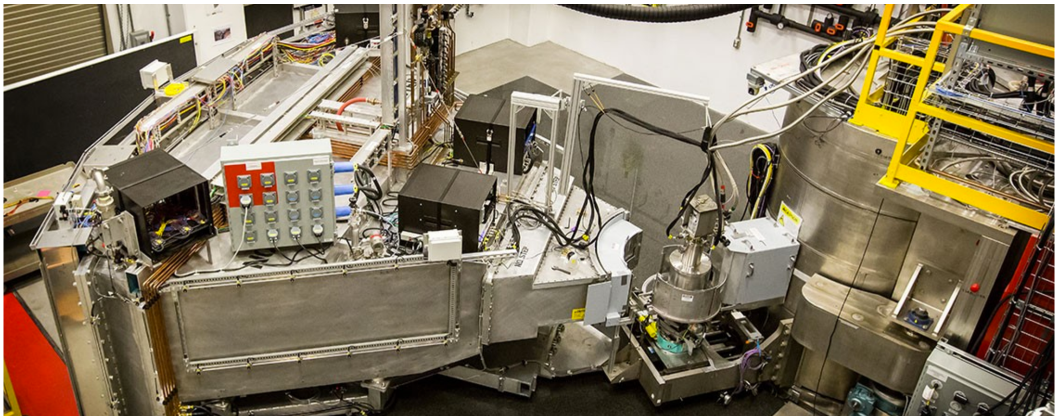

Figure 2.7: Photo of HYSPEC at BL-14B of SNS.

sample rotations about the vertical axis. From such a set of scans, a four-dimensional data set was created and analyzed with the MANTID [16] and DAVE [17] software packages. Slices of data corresponding to particular planes in energy and wave vector space can then be plotted from the larger data set. At HYSPEC, in order to improve the resolution along $\mathbf{Q}_z$, the graphite-crystal array in the incident beam can be set in the flat mode (no vertical focusing).

References

[1] GD Gu, T Egi, N Koshizuka, PA Miles, GJ Russell, and SJ Kennedy. Effect of growth conditions on crystal morphology and superconductivity of Bi-2212 oxide. *Physica C: Superconductivity*, 263(1-4):180–184, 1996.

[2] A Revcolevschi and J Jegoudez. Growth of large high-Tc single crystals by the floating zone method: A review. *Progress in Materials Science*, 42(1-4):321–339, 1997.

[3] Hanna A Dabkowska and Antoni B Dabkowski. Crystal growth of oxides by optical floating zone technique. pages 367–391, 2010.

[4] K Byrappa, AK Subramani, KM Lokanatha Rai, B Basavalingu, S Ananda, and S Srikantaswamy. Crystal growth of technologically important electronic materials. 2003.

[5] Isao Tanaka, Takeshi Obuchi, and Hironao Kojima. Growth and characterization of titanite (CaTiSiO5) single crystals by the floating zone method. *Journal of Crystal Growth*, 87(2-3):169–174, 1988.

[6] Jyh-Chen Chen, Yeou-Chang Lee, and Chieh Hu. A simple method of examining the propagation of defects in the floating-zone solidification process of lithium niobate. *Journal of crystal growth*, 166(1-4):151–155, 1996.

[7] Hironao Kojima, Minoru Watanabe, and Isao Tanaka. Crystal growth of strontium-substituted barium titanate ($Ba_{1-x}Sr_xTiO_3$) by the floating zone method. *Journal of crystal growth*, 155(1-2):70–74, 1995.

[8] Wataru Itoyama, Kazuake Iishi, and Sin'ichi Sakata. Growth of βII-Li_3VO_4 single crystals by the floating zone technique with the aid of a heat reservoir. *Journal of crystal growth*, 158(4):534–539, 1996.

[9] Thierry Duffar. *Crystal growth processes based on capillarity: Czochralski, floating zone, shaping and crucible techniques*. John Wiley & Sons, 2010.

[10] R. D. Zhong, J. A. Schneeloch, X. Y. Shi, Z. J. Xu, C. Zhang, J. M. Tranquada, Q. Li, and G. D. Gu. Optimizing the superconducting transition temperature and upper critical field of $Sn_{1-x}In_xTe$. *Phys. Rev. B*, 88:020505, July 2013.

[11] R. D. Zhong, J. A. Schneeloch, T. S. Liu, F. E. Camino, J. M. Tranquada, and G. D. Gu. Superconductivity induced by in substitution into the topological crystalline insulator $Pb_{0.5}Sn_{0.5}Te$. *Phys. Rev. B*, 90:020505, Jul 2014.

[12] Ruidan Zhong, John Schneeloch, Qiang Li, Wei Ku, John Tranquada, and Genda Gu. Indium substitution effect on the topological crystalline insulator family $(Pb_{1-x}Sn_x)_{1-y}In_yTe$: topological and superconducting properties. *Crystals*, 7(2):55, 2017.

[13] GL Squires and Jeffrey W Lynn. *Introduction to the theory of thermal neutron scattering*. AIP, 1979.

[14] Gen Shirane, Stephen M. Shapiro, and John M. Tranquada. *Neutron Scattering with a Triple-Axis Spectrometer: Basic Techniques*. Cambridge University Press, 2002.

[15] Igor A Zaliznyak, Andrei T Savici, V Ovidiu Garlea, Barry Winn, John Schneeloch, John M Tranquada, Genda Gu, Aifeng Wang, and Cedomir Petrovic. Polarized neutron scattering on HYSPEC: the HYbrid SPECtrometer at SNS. *arXiv preprint arXiv:1610.06018*, 2016.

[16] O. Arnold, J.C. Bilheux, J.M. Borreguero, A. Buts, S.I. Campbell, L. Chapon, M. Doucet, N. Draper, R. Ferraz Leal, M.A. Gigg, V.E. Lynch, A. Markvardsen, D.J. Mikkelson, R.L. Mikkelson, R. Miller, K. Palmen, P. Parker, G. Passos, T.G. Perring, P.F. Peterson, S. Ren, M.A. Reuter, A.T. Savici, J.W. Taylor, R.J. Taylor, R. Tolchenov, W. Zhou, and J. Zikovsky. MantidâĂŤData analysis and visualization package for neutron scattering and {SR} experiments. *Nuclear Instruments and Methods in Physics Research Section A: Accelerators, Spectrometers, Detectors and Associated Equipment*, 764:156 – 166, 2014.

[17] Richard Tumanjong Azuah, Larry R Kneller, Yiming Qiu, Philip LW Tregenna-Piggott, Craig M Brown, John RD Copley, and Robert M Dimeo. Dave: a comprehensive software suite for the reduction, visualization, and analysis of low energy neutron spectroscopic data. *Journal of Research of the National Institute of Standards and Technology*, 114(6):341, 2009.

Chapter 3

Indium Substitution Effect on the Topological Crystalline Insulator (Pb,Sn)Te

In this Chapter, I present our research on the indium substitution effect on the topological crystalline insulator $Pb_{1-x}Sn_xTe$ on both superconducting and topological properties. This Chapter is largely reprinted from my published articles, Ref. [1–4]; copyright is held by the American Physical Society.

3.1 Introduction to topological insulators and extended topological materials

Topological insulators (TIs) are a class of materials that are currently the focus of considerable attention, since they represent a new state of matter in which the bulk is an insulator with an “inverted” energy gap induced by a strong spin–orbit coupling (SOC) which leads to the emergence of unusual gapless edge or surface states protected by time-reversal-symmetry [5–8]. They are made possible because of two major features of quantum mechanics: symmetry under the reversal of the direction of time; and the spin-orbit interaction, which occurs in heavy elements such as mercury and bismuth [8]. To explain the properties of these special insulators, a short review of the historical developments that led to the theoretical predictions and experimental confirmations of the existence of topological insulators is necessary.

3.1.1 Theoretical basics

A great discovery in the 1980s was that electrons that are restricted to a two-dimensional (2D) system and subject to a strong magnetic field show a topological feature – a completely different type of order, which underlies the quantum Hall effect. In its interior, the motions of electrons would curve into a circle under the Lorentz force, just like in a normal insulator (Figure 3.1*a*). However, at the boundary, the circular orbits can bounce off the edge, leading to these continuous half-circle motions, which makes the boundary conducting. In the quantum Hall (QH) state, the bulk of the 2D sample is insulating, and the electric current is carried only along the edge of the sample (Figure 3.1*b*). Normally, electrons can scatter off impurities, but given that those electrons cannot move backwards under a given magnetic field, the electrons have no choice but to propagate forwards when they hit an impurity. This is known as “dissipationless" transport by the edge states – no electrons scatter and so no energy is lost as heat. The QH state provided the first example of a quantum state which is topologically distinct from all states of matter known before.

Topological insulators are similar to the quantum Hall state in that they exhibit “topological order", namely, different order. However, a strong magnetic field is not necessary in the case of topological insulators because the spin-orbit coupling plays the role of magnetic filed. SOC is the interaction of an electron’s intrinsic angular momentum, or spin, with the orbital motion of the electrons through space. In atoms with a high atomic number, such as mercury (Hg) and bismuth (Bi), the spin-orbit force is strong so that when electrons travel through these materials they feel as if they are in a strong magnetic field.

The simplest 2D topological insulator is the quantum *spin* Hall state, which was first predicted in 2005 [9, 10]. As in an ordinary insulator there is thus a gap separating the occupied and empty states in the interior, but there are edge states in which the spin-up and spin-down electrons propagate in opposite directions(Figure 3.1*c*). The Hall conductance of this state

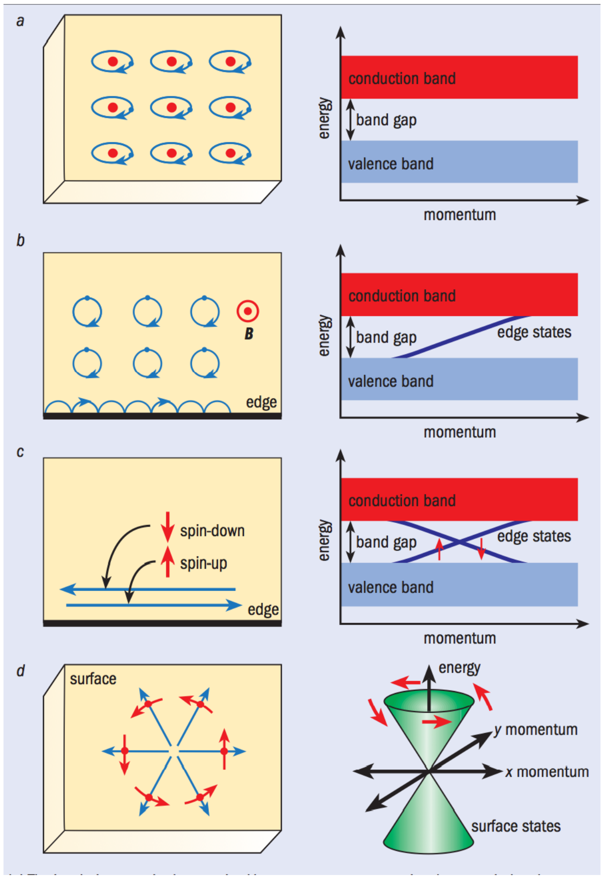

Figure 3.1: (a) In insulating state the energy gap separates the occupied and empty electronic states. (b) In the quantum Hall effect, the circular motion of electrons in a magnetic field, B, is interrupted by the sample boundary. At the edge, the circular orbits bounce off the edge, leading to “skipping orbits” as shown, resulting to perfect conduction in one direction along the boundary. (c) At the edge of 2D topological insulators or quantum spin Hall effect state, two kind of spins moving oppositely so electrons can propagate in both directions. (d) The surface of a 3D topological insulator supports electronic motion in any direction, so that the energy-momentum relation has a “Dirac cone" structure.

is zero because the spin-up and spin-down electrons cancel each other. However, the edge states can conduct. In the quantum Hall effect, the bulk conductance is zero, while the edge states are conducting with current flowing in one direction around the edge of the system. Similarly, in the quantum-spin-Hall state, the bulk is still insulating while edge-state electrons with opposite spins propagate in opposite directions, consistent with time-reversal symmetry. Time reversal switches both the direction of propagation and the spin direction, interchanging the two counter-propagating modes. The first experimental discovery in this field was the observation of the 2D quantum spin Hall effect in a quantum-well structure made by sandwiching a thin layer of mercury telluride (HgTe) between layers of mercury cadmium telluride ($Hg_xCd_{1-x}Te$).

Theoretical concepts were soon generalized to three dimensions and shown experimentally in materials such as $Bi_{1-x}Sb_x$ [11]. As in the 2D case, the direction of an electron's motion along the surface of a 3D topological insulator is locked to the spin direction, which now changes continuously as a function of propagation direction, resulting in an unusual "planar metal". In the bulk of a TI, the electronic band structure resembles that of an ordinary band insulator, with the Fermi level falling between the conduction and valence bands. On the surface of a TI, there are special states that fall within the bulk energy gap and allow surface metallic conduction (Figure3.1*d*). Although ordinary band insulators can also support conductive surface states: the locking of the spin and propagation directions eliminates the possibility of back-scattering from nonmagnetic impurities.

3.1.2 Topological insulators (TIs)

The first key experiment in this field was the observation of the 2D quantum spin Hall effect in a quantum-well structure made by sandwishing a thin layer of mercury telluride (HgTe) between layers of mercury cadmium telluride ($Hg_xCd_{1-x}Te$). Earlier theoretical work by Bernevig, *et al.* predict that a 2D topological insulator with quantized charge conductance along the edges would be realized in (Hg,Cd)Te quantum well [10]. Experimental results published in 2007 by a research group from the University of Würzburg, Germany, led by Laurens Molenkamp measured the electrical transport properties of such structures and observed the predicted $2e^2/h$ conductance. However, measurements of electrical transport, which are ideal for probing the 2D quantum spin Hall effect, are problematic for 3D topological insulators because it is hard to separate the bulk and surface conductivity and their contributions to the current. Therefore, a probe that couples mainly to the surface would be better and researchers turned to angle-resolved photoemission spectroscopy (ARPES), which is ideally suited to the task. ARPES uses the photoelectric effect: high-energy photons are shone onto the sample and electrons are ejected. By analysing the energy, momentum and spin of these electrons, the electronic structure and spin polarization of the surface states can be directly measured.

The first 3D topological insulator to be probed using ARPES was the semiconducting alloy bismuth antimonide Bi_xSb_{1-x} [12]. Simpler versions of the 3D TI were theoretically predicted in Bi_2Se_3, Sb_2Te_3 [13] and Bi_2Se_3 [13, 14]–compounds with a large bulk gap and a gapless surface state consisting of a single Dirac cone. Later ARPES experiments indeed observed the linear dispersion relation of these surface states [14, 15]. Those discoveries confirmed the ubiquitous existence in nature of this new topological state. It is also remarkable that such topological effects can be realized in common materials without requiring extreme conditions. These materials, which are well-known semiconductors with strong spin-orbit interactions, have a relatively large bulk energy gap (0.3 eV for Bi_2Te_3), which means that they work at room temperature. They also have the simplest possible surface-state structure. The advantages of these materials have unleashed a worldwide experimental effort to understand their electrical and magnetic properties and to find other classes of topological insulators.

These materials have been named topological insulator because they behave as an insulator in the interior but with special conducting states on the surface[9], and the wave functions describing their electronic states span a Hilbert space that has a nontrivial topology [7]. Although ordinary band insulators can also support conductive surface states, the surface states of topological insulators are special since they are topological protected by particle number conservation and time reversal symmetry [16–18], which means that unlike ordinary surface states they cannot be eliminated by disorder or chemical passivation.

Topological insulators and superconductors offer a chance to test many novel ideas in particle physics. It would be interesting to explore the possibility of electronic devices with low power consumption based on the dissipationless edge channels of the QSH state, spintronics devices based on the unique current-spin relationship in the topological surface states, infrared detectors, and thermoelectric applications.

After those pioneering theoretical and experimental works on the prototype topological materials HgTe, $Bi_{1-x}Sb_x$, Bi_2Se_3, and Sb_2Te_3, people have devoted great enthusiasm in exploring new topological insulator materials and the field is now expanding at a rapid pace. Beyond the topological materials mentioned above, more than 50 new compounds have been predicted to be topological insulators. The nontrival topological property of topological insulators originates from the inverted band structure induced by SOC. Therefore, it is more likely to find topological insulators in materials which consist of covalent compounds with narrow band gaps and heavy atoms with strong SOC. Based on such a guiding principle, more than 50 new compounds have been proposed to be topological insulator materials.

The first group is the thallium-based III-V-VI ternary chalcogenides, including $\mathrm{TlBi}Q_2$ and $\mathrm{TlSb}Q_2$ with Q=Te, Se, and S [19, 20]. These materials have the same rhombohedral crystal structure as the tetradymite semiconductors. Among them, $\mathrm{TlBiSe_2}$, $\mathrm{TlBiTe_2}$ have recently been experimentally observed to be topological insulators [21, 22]. The second group is the ternary heusler compounds with distorted crystal structure [23, 24], and around 50 of them are found to exhibit band inversion. Thanks to the diversity of Heusler materials, multifunctional topological insulators can be realized with additional properties ranging from superconductivity to magnetism and heavy-fermion behavior [23, 24]. The third group of new topological insulators is related to the electron correlation effects. An example is the case of Ir-based materials, such as $\mathrm{Na_2IrO_3}$, and $Ln_2\mathrm{IrO_7}$ with Ln=Nd, Pr [25–27].

3.1.3 Topological crystalline insulators (TCI): $\mathrm{Pb}_{1-x}\mathrm{Sn}_x\mathrm{Te}$

In 2011, the notion of “topological crystalline insulators” (TCIs) was introduced to describe a new category of topological materials. Similar to the topological insulator, where the special topological surface states are protected by the time-reversal-symmetry which is guaranteed by the strong spin-orbit coupling, the special surface states in topological crystal insulators are protected by certain crystal point group symmetries [28]. These topological crystalline insulators are the counterpart of topological insulators in materials without spin-orbit coupling. Instead, an electron's orbital degrees of freedom play a role similar to spin. Unlike the linearly dispersing Dirac surface states of topological insulators, the (001) surface states of topological crystalline insulators have quadratic band degeneracy protected by time-reversal and discrete rotational symmetry. This new state of matter features metallic surface states with quadratic band dispersion on high symmetry crystal surfaces, and it was shown that such a situation is realized in an insulating crystal having rocksalt structure. This has caused quite a sensation, since the first example, SnTe, has been theoretically [29] and experimentally [30] confirmed to exhibit topological surface states in <001>, <110>, and <111> surfaces. Soon after this discovery, the topological surface state in the Pb-doped $Pb_{1-x}Sn_xTe$ and $Pb_{1-x}Sn_xSe$ were verified by ARPES and Landau level spectroscopy using scanning tunneling microscopy and spectroscopy [31–33], thus expanding the range of relevant materials. Alongside SnTe and the related alloys $Pb_{1-x}Sn_xSe/Te$, other chalcogenides such as SnS and SnSe that incorporate lighter elements have also been predicted to be TCIs, even without the SOC [34]. In theory, by applying external pressure, normal IV-VI rocksalt chalcogenides can be tuned into TCIs [35]. Besides the materials with rocksalt crystal structure, Hsieh et al. predicted that the antiperovskite family are also promising materials for exploring the topological and other related properties [36]. More recently, a new phase of Bi stabilized by strain has been found to be a TCI based on mirror symmetry, similar to SnTe [37].

3.1.4 Topological Superconductors (TSCs) and Superfluids

The discovery of TIs and TCIs has also stimulated the search for a superconducting analogue, a time-reversal-invariant topological superconductor (TSC) [22, 38–41]. TSCs are accompanied by gapless states at the edge or surface, which characterize the nontrivial topological nature of the bulk state and are often composed of *Majorana fermions* [40]. The superfluidity has been proved in the superfluid ^{3}He-B-phase, with experimentally measurable surface states protected by the time-reversal symmetry. These states have a full pairing gap in the bulk, gapless counter-propagating Majorana states at the boundary, and a pair of Majorana zero modes associated with each vortex[39]. The half-Heusler alloys YPtBi, LaPtBi, and LuPtBi are classified as TIs and are also known to be superconducting [42–44]. These materials have also been identified as possible candidates for 3D topological superconductors based on the band inversion that they exhibit [42, 44].

Superconductors derived from TIs by doping have been considered as TSC candidates, such as $Cu_xBi_2Se_3$ [45, 46]. Since the topological surface states are protected from back-scattering by disorder, it should be safe to tune the chemical potential through chemical substitution. By intercalating with copper, $Cu_xBi_2Se_3$ displays superconductivity with a maximum transition temperature T_c of 3.8 K at accessible temperatures in a certain doping range ($0.10 \leq x \leq 0.3$) [46–50]. Zero resistivity and a diamagnetic shielding fraction of up to 56% have been achieved in samples obtained by quenching [50].

$TlBiTe_2$ is observed to be a superconductor with p-type carriers [20]. Compared to the $Cu_xBi_2Se_3$ superconductor, the coexistence between topological surface states and bulk superconductivity in $TlBiTe_2$ is much better defined, because of the clear separation of the surface and bulk states in momentum space.

Indium-doped tin telluride ($Sn_{1-x}In_xTe$), a low-carrier density superconductor based on a narrow-gap IV-VI semiconductor, has been proposed to be a new type of TSC with the experimental evidence to support the existence of topological surface states [51]. ARPES studies performed on $Sn_{1-x}In_xTe$ (SIT) at x = 0.045 confirmed that the topological surface states remain intact after In doping [51]. Earlier studies of superconductivity in $Sn_{1-x}In_xTe$ have shown that one can vary T_c from < 1 K at $x =$0.02 to 2.6 K at $x =$0.2 [52–54]. Later studies including our group achieved the optimal T_c to 4.5 K by further increasing the In concentration [1, 55, 56]. Similarly, doping the TCI $Pb_{0.5}Sn_{0.5}Te$ with indium also induces superconductivity[2]. This spurs interest in searching for a topological superconductor in the SnTe and $Pb_{1-x}Sn_xTe$ systems.

A challenge for characterizing the transport properties of surface states in TI/TCI materials such as Bi_2Se_3 and SnTe is the dominance of a pronounced bulk conductance [57, 58]. Despite considerable efforts to reduce the bulk carrier density, such as modifying crystal growth method [59], reducing sample thickness [60], and chemical counterdoping [61–63], bulk conduction has proven difficult to suppress. Inspired by the goal of finding truly bulk-insulating topological materials, we have found that indium doping the TCI materials (Pb,Sn)Te can yield a huge bulk resistivity while maintaining topological surface states [3], which will be discussed in detail in the following section 3.3.

3.2 Indium substitution effect on (Pb,Sn)Te: Crystal structure and superconductivity

Unlike the two-dimensional electron gas or quantum Hall systems, three-dimensional topological insulators can harbor superconductivity and magnetism, making it possible to study the interplay between topologically ordered phases and broken-symmetry states. Previous observations of superconductivity in the doped topological crystalline insulators SnTe and $Pb_{0.5}Sn_{0.5}Te$ led to speculations that these compounds may be topological superconductors that provide platforms for studying the interplay between topological and broken-symmetry order.

It has been reported that indium doped on the Sn site yields superconductivity in ferroelectric semiconductor SnTe with critical temperature T_c up to 2 K[52]. To investigate the effect of the indium concentration on the crystal structure and superconducting properties of the topological crystalline insulators (Pb,Sn)Te, we have grown high-quality single crystals and have performed systematic studies for indium content in the range $0 \leq x \leq 0.5$. In this section, the indium induced superconductivity in the (Pb,Sn)Te system will be presented and discussed in details.

3.2.1 Crystal structure of indium doped (Pb,Sn)Te

SnTe is a IV-VI semiconductor that crystallizes in the cubic rocksalt structure at room temperature, and maintains this structure after a certain degree of substitution of Sn with Pb and/or In (Figure 1a). Due to the unchanged crystal structure, the crystal point group symmetries that are essential to maintain the topological surface states remain the same. Because of the difference in lattice constants of the end members (PbTe > SnTe > InTe), the lattice parameters of $(\mathrm{Pb}_{1-x}\mathrm{Sn}_x)_{1-y}\mathrm{In}_y\mathrm{Te}$ compounds vary with x and y.

X-ray diffraction (XRD) was used to investigate the crystal structure. For parent compound SnTe, as shown in Figure 3.2*a*, the peaks of the indium-free sample (SnTe) can be indexed well to the rocksalt structure (space group $Fm\bar{3}m$) with a lattice constant of a=6.318Å, consistent with previous studies[29, 64]. Similarly, XRD patterns were obtained for each of the polycrystalline samples (x=0.1–1.0) as shown in Figure 3.2*a*. Only the cubic phase is detected for $x \leq 0.3$, while the x=0.4 sample shows a trace amount ($\leqslant$ 2%) of a secondary phase (tetragonal InTe). For x=0.5, an undertermined secondary phase is present, while the tetragonal InTe phase becomes substantial for $x \geq 0.6$.

The XRD patterns for the single-crystal SnTe are plotted in Figure 3.2*b*. There is no detectable second phase for for $x \leq 0.4$. For x=0.45, there is a small second phase, while x=0.5 exhibits asymmetrically broadened diffraction peaks but no obvious second phase. The lattice parameter a determined for the cubic phase in the polycrystalline and single-crystal sample is illustrated in Figure 3.2*c*. According to Vegard's law, the lattice parameters of the alloy samples should vary linearly between the values of the end members. There is a complication in the present case in that the stable phase of InTe is tetragonal. The cubic phase is stable at high pressure, and it can be retained as a metastable phase at ambient pressure with reported a=6.177Å at room temperature [66].

We find that the lattice parameters of the single-crystal samples follow a straight line but with a slightly reduced slope. The polycrystalline samples follow the same line up to x=0.4, but deviate from it for $x \geq 0.5$, where substantial amounts of the second phase are evident. Clearly, the

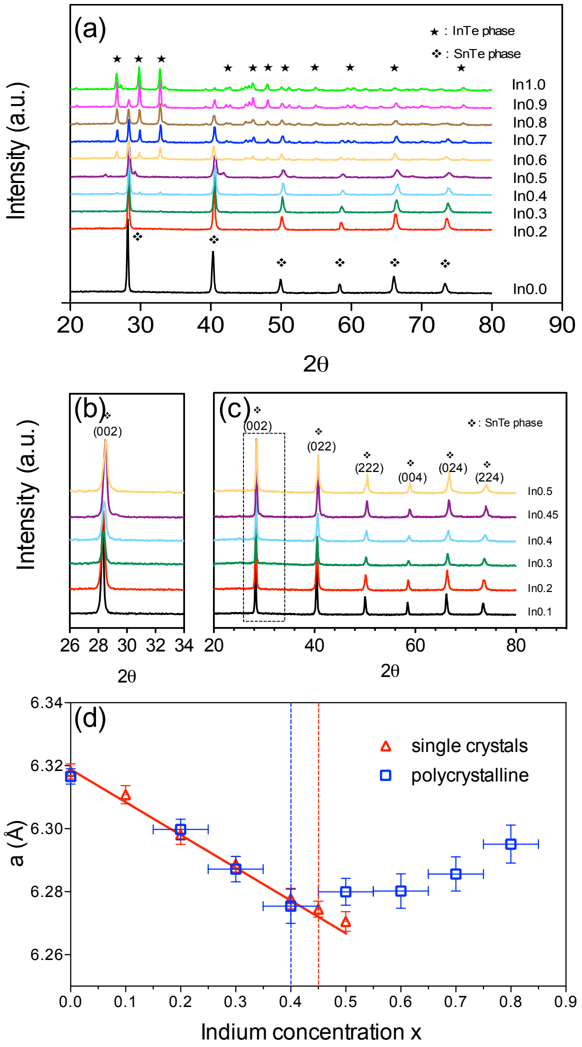

Figure 3.2: (a) X-ray diffraction spectra for $Sn_{1-x}In_xTe$ (Inx) polycrystalline samples with nominal compositions x=0–1.0. (b) Zoomed in angle range between 26–34° to illustrate (002) peak of the cubic structure for single crystals with varies In concentrations. (c) XRD patterns for $Sn_{1-x}In_xTe$ single crystals doped with In (x=0.1–0.5). (d) Lattice parameters a derived from Rietveld analysis of XRD patterns of the cubic phases in polycrystalline (blue squares) and single crystal (red triangles) samples as a function of the nominal indium concentration x.

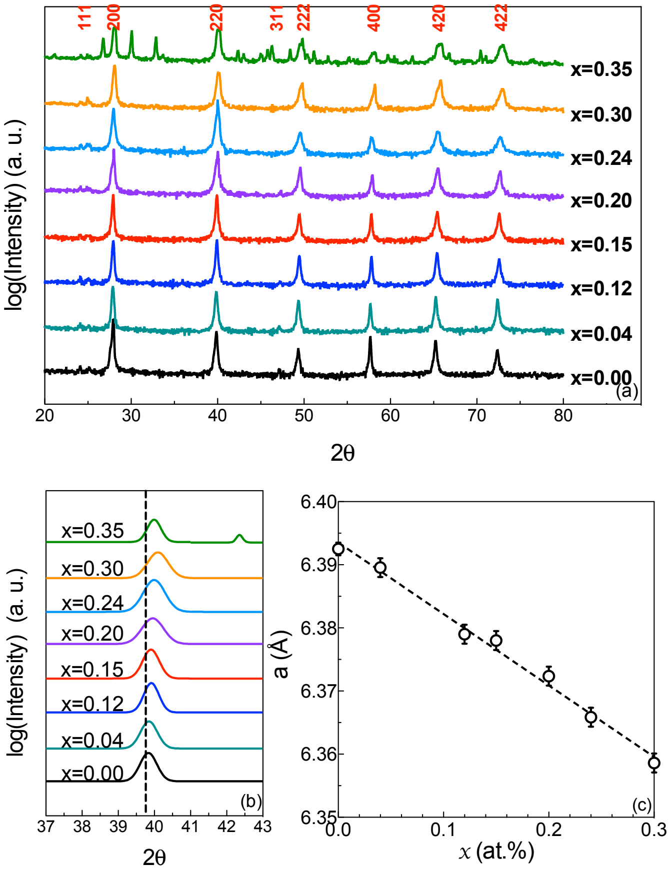

Figure 3.3: (a) X-ray diffraction patterns for the $(Pb_{0.5}Sn_{0.5})_{1-x}In_xTe$ single crystals with composition x=0–0.35, with intensity plotted on a logarithmic scale. The data have been smoothed using the Savitzky-Golay algorithm, and the $K\alpha_2$ component have been removed [65]. The Miller indices of major peaks in the cubic phase have been identified. (b) Gaussian fitted curves for the (220) peak in the cubic phase. (c) Lattice parameters a of the cubic phase as a function of the indium concentration x.

In concentration in the cubic-phase alloy reaches its maximum at $x \approx 0.5$ in the single crystal samples, and that saturation leads to the presence of the InTe second phase for larger x. Given the linear evolution of a and the single-phase behavior for $x < 0.5$, we conclude that the actual In concentration is approximately equal to the nominal concentration in cubic phase $Sn_{1-x}In_xTe$ for $x \leq 0.5$.

Indium-doping has similar effect on the crystal structure of $Pb_{0.5}Sn_{0.5}Te$. Figure 3.3*a* presents the measured XRD patterns, with the intensity plotted on a logarithmic scale. As can be seen, the peaks of the samples with $0 \leq x \leq 0.30$ can be indexed well to the rocksalt structure. The tetragonal InTe impurity phase only becomes substantial for x=0.35. Thus, compared to the solubility limit of In in pure SnTe, which is about 45%, the solubility limit of In in the $Pb_{0.5}Sn_{0.5}Te$ alloys is approximately 0.30, which is about 50% higher than the limit found in samples prepared by the conventional metal-ceramic technique [67–69]. In these solid solutions, Pb/Sn and Te form two separate *fcc* sublattices, with successive substitution of Pb.Sn by In. Figure 3.3*b* shows the Gaussian fitted (220) peaks, illustrating that the peak position shifts gradually to larger angle before reaching the solubility limit. The x dependence of the corresponding lattice constant a is displayed in Figure 3.3*c*. We find that a=6.392 Å for x=0, decreasing linearly to a=6.359 Å for x=0.30 sample.

The solubility limit of In in the $Pb_{0.5}Sn_{0.5}Te$ can be further confirmed by microstructural investigation of the crystals using an analytical high-resolution scanning electron microscope (SEM) equipped for energy-dispersive X-ray spectroscopy (EDS). SEM images in Figure 3.4 show typical microstructures of the $(Pb_{0.5}Sn_{0.5})_{1-x}In_xTe$ cleaved surface. Figure 3.4*a* is representative for $x \leq 0.3$, with a dense uniform microstructure having few voids, consistent with single-phase behavior. In contrast, the x=0.35 sam-

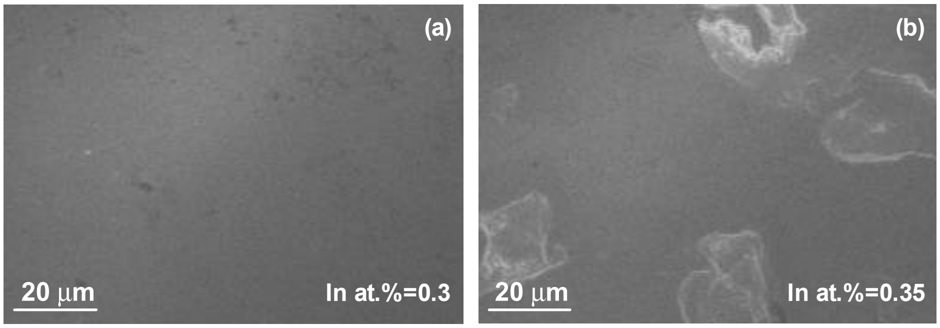

Figure 3.4: Scanning electron microscope (SEM) images for (a) 30% and (b) 35% In substituted $(Pb_{1-x}Sn_x)_{1-y}In_yTe$ crystals. Insets are enlarged images.

ple shown in Figure 3.4*b* exhibits a secondary phase, confirmed as InTe by EDS analysis, dispersed randomly in the majority phase.

Figure 3.5*b* shows the XRD patterns of SnTe (x =1, y =0, black), $Pb_{0.5}Sn_{0.5}Te$ (x =0.5, y =0, blue) and $(Pb_{0.5}Sn_{0.5})_{0.7}In_{0.3}Te$ ($x = 0.5$, $y = 0.3$, red), respectively. Compared to the parent compound SnTe, with a lattice constant $a = 6.32$ Å, Pb-doping increases the lattice constant ($a = 6.39$ Å for $Pb_{0.5}Sn_{0.5}Te$). Subsequent In-doping can then decrease the lattice constant ($a = 6.36$ Å for $(Pb_{0.5}Sn_{0.5})_{0.7}In_{0.3}Te$). Similarly, a systematic shrinking of the unit cell as a function of In content has been observed in previous studies of SIT[1, 70]. The measured lattice parameters listed on the figure for the various compositions are qualitatively consistent with Vegard's law and the differences in radii of the ionic components. With more Sn or Pb atoms being replaced by In, the local distortion of the crystal structure gets larger, and eventually the solubility limit is reached, indicated by the appearance of the secondary phase InTe.

Common tools to characterize the surface states include angle-resolved photoemission spectroscopy (ARPES) and scanning tunneling microscopy

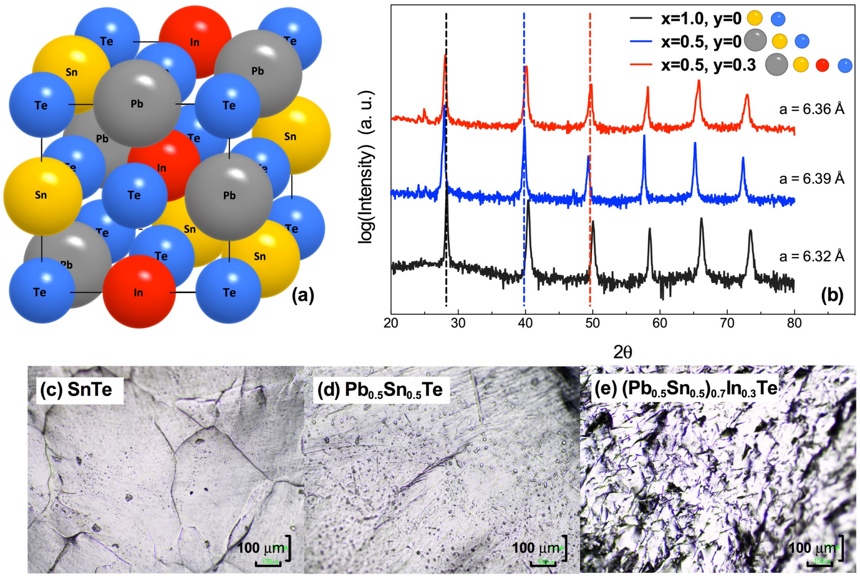

Figure 3.5: (a) A sketch of the crystal structure of SnTe with Sn atoms (yellow) partially replaced by Pb (grey) and In (red). (b) X-ray powder diffraction (XRD) patterns for SnTe (black), $Pb_{0.5}Sn_{0.5}Te$ (blue) and $(Pb_{0.5}Sn_{0.5})_{0.7}In_{0.3}Te$ (red), respectively. Each dashed line marks the position of an XRD peak of a compound with the same color. (c-e) Optical microscope photos of the pristine surface of SnTe (c), $Pb_{0.5}Sn_{0.5}Te$ (d) and $(Pb_{0.5}Sn_{0.5})_{0.7}In_{0.3}Te$ (e).

(STM). To apply these techiques, one typically needs atomically-flat and well-oriented surfaces. For the topological insulator Bi_2Se_3, this is not a problem, since it can be easily cleaved due to weak coupling between its layers. In the case of SnTe related compounds, however, the situation is more challenging due to their isotropic cubic structures. To illustrate, Figures 3.4*c*-*e* show microscope photos of pristine surfaces. The flat, shiny planes are cleaved surfaces, and they become smaller with increasing Pb/In substitution. Thus, it appears that substitution of Pb or In atoms introduces lattice distortion and leads to smaller cleaved surfaces for surface-sensitive studies. STM studies of SIT single crystal samples have been successfully performed[51], as discussed in Sec. 3.4.1. Direct ARPES studies of PSIT single crystals are few, and it has proved more practical to perform measurements on thin films evaporated from previously characterized bulk samples[3, 71].

3.2.2 Indium induced superconductivity in SnTe

The superconducting transition temperature of each sample was determined by magnetization measurements. Figure 3.6*a* shows the temperature dependence of the zero-field-cooled (ZFC) and field-cooled (FC) magnetization for the $Sn_{0.55}In_{0.45}Te$ single crystal measured between 1.75 and 6 K under an applied field of 1 mT. The onset of the Meissner signal occurs at T_c=4.5 K. The magnetic hysteresis (M–H) loops for representative x=0.2 and 0.45 single crystal samples measured at 1.75 K are compared in Figure 3.6*b*. Clearly the M–H curve for In0.45 includes a larger area than that of In0.2, indicating stronger flux pinning for 45% indium substitution. The lower critical field H_{c1}, defined by the deviation point of the

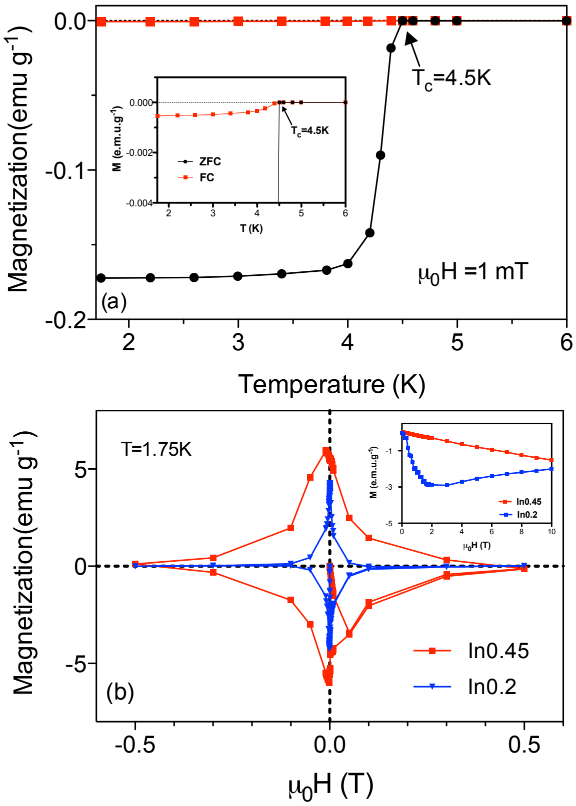

Figure 3.6: (a) Temperature dependence of magnetic susceptibility for $Sn_{0.55}In_{0.45}Te$ single crystal measured under conditions of Fc (ZFC) in an applied field of 1 mT at a cooling (heating) rate of 0.1 K/min. (b) Hysteresis loop of a $Sn_{0.55}In_{0.45}Te$ single crystal measured at 1.75 K. The inset shows the initial M–H behavior at a field less than 10 mT and 1.75 K. For magnetization measurements, samples are cut into roughly cubiclike small chunks. The demagnetization factor can be taken as 1 considering that the crystal structure is isotropic.

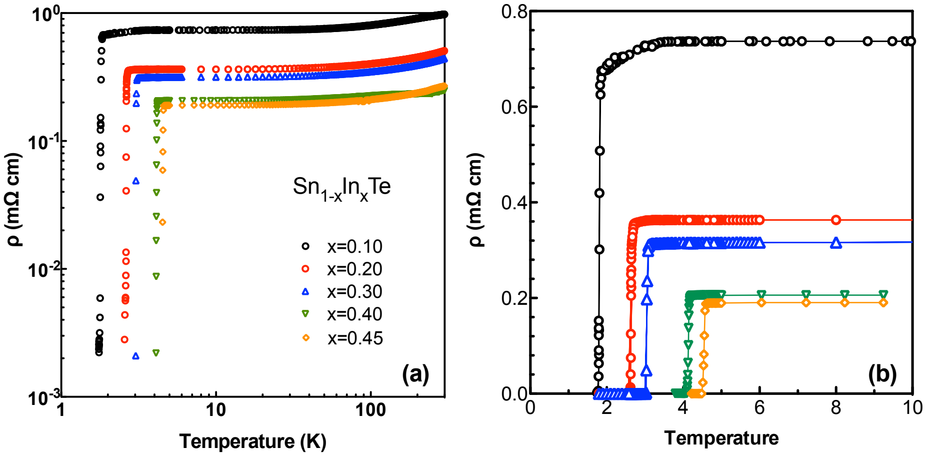

Figure 3.7: (a) Temperature dependence of resistivity for $Sn_{1-x}In_xTe$ single crystals in the normal state up to 300 K. (b) Temperature dependence of resistivity for $Sn_{1-x}In_xTe$ single crystals at low temperature.

M–H curve from its initial linear behavior, can be estimated from the data in the inset of Figure 3.6*b*. With higher indium concentration, $Sn_{1-x}In_xTe$ superconductors are more likely to resist magnetic flux penetration.

The resistivity of $Sn_{1-x}In_xTe$ single-crystal samples is weakly metallic in the normal state up to 300 K (Figure 3.7*a*); the transition to zero resistance is fairly sharp, with a typical width of 0.2 K, as shown in Figure 3.7*b*. The parameter T_c(R) is defined as the onset temperature for the drop in resistivity.

The superconducting critical temperature T_c(M) is defined as the temperature at which the magnetic moment begins to drop sharply. The results for all samples are displayed in Figure 3.8. Starting at small x, the polycrystalline samples show an almost linear relation between T_c and x, reaching the highest T_c of 4.5 K when x=0.4. The variation of T_c with x for single crystals shows a similar relation. This trend confirms and ex-

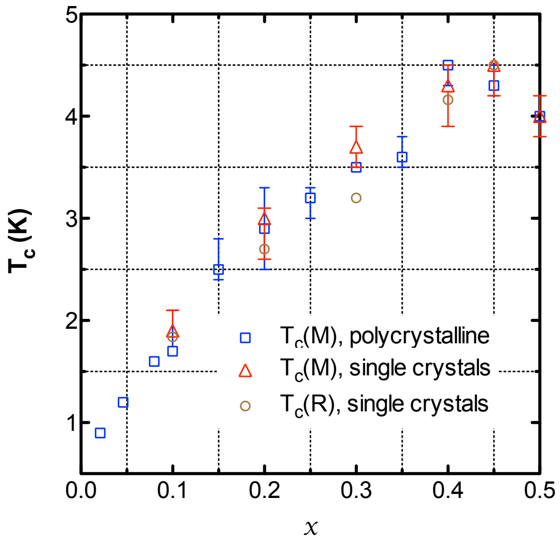

Figure 3.8: Superconducting transition temperature as a function of indium concentration x for both polycrystalline (blue squares) and single-crystal samples (red triangles), obtained from magnetization measurements, and for single crystals (brown circles) from resistivity measurements. For each concentration, different parts of the as-grown crystal rod were measured to give an average value of T_c. Data for indium concentrations less than 110% are taken from Erickson *et al.*[54].

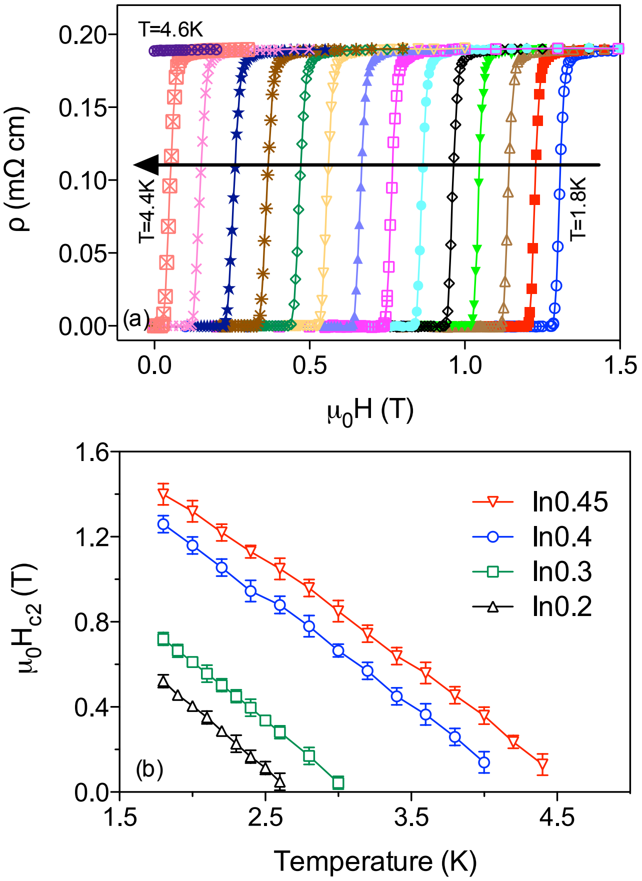

Figure 3.9: (a) Field dependence of the resistivity for the x=0.45 crystal at fixed temperatures from 1.8 to 4.6 K. (b) Upper critical field $H_{c2}(T)$ determined from resistivity measurements on four single crystals.

Table 3.1: Upper critical field at zero temperature $H_{c2}(0)$ for $\mathrm{Sn}_{1-x}\mathrm{In}_x\mathrm{Te}$, estimated using the Werthamer-Helfand-Hohenberg approximation.

In concentration	slope (T/K)	T_c (K)	$\mu_0 H_{c2}(0)$(T)
0.2	-0.58	2.7	1.08
0.3	-0.55	3.1	1.18
0.4	-0.49	4.2	1.42
0.45	-0.48	4.5	1.49

tends the earlier experimental results from several groups, and it occurs within the regime where the XRD results indicate that the samples are essentially single phase. As the indium concentration increases, superconducting critical temperature determined from resistivity measurements T_c(R) changes similarly with T_c(M), as shown in Figure 3.8.

The magnetic-field dependence of the electrical resistivity for single crystals was also measured. Representative data for $\mathrm{Sn}_{0.55}\mathrm{In}_{0.45}\mathrm{Te}$ are shown in Figure 3.9*a*. The upper critical field $H_{c2}(T)$ is defined as the onset of the resistive transition at each fixed temperature; the results are shown in Figure3.9*b*. The upper critical field at zero temperature $H_{c2}(T = 0)$ can be estimated using the Werthamer-Helfand-Hohenberg approximation [72], $\mu_0 H_{c2}(0) = 0.69 T_c |d\mu_0 H_{c2}/dT|_{T=Tc}$. From the measured curves for $\mu_0 H_{c2}(T)$, we obtain the initial slopes (at $T \approx T_c$) and also estimate the upper critical fields, as shown in the table 3.1. These results show that a stronger applied field is needed to completely suppress the superconductivity at 0 K for $\mathrm{Sn}_{1-x}\mathrm{In}_x\mathrm{Te}$ superconductors with higher indium concentrations.

3.2.3 Indium induced superconductivity in $Pb_{0.5}Sn_{0.5}Te$

The critical temperature of each sample are defined as the onset point of the sharp transition of the resistivity (Figure 3.10*a*) and magnetic moment (Figure 3.10*b*). Figure 3.10*b* shows the temperature dependence of zero-field-cooled and field-cooled magnetization under an applied field of 1 mT for the optimal doped single crystal sample $Pb_{0.5}Sn_{0.5}Te$. The onset of the magnetic transition occurs at T_c =4.7 K, with a transition width of about 0.5 K (obtained from the temperatures corresponding to 10% and 90% of the full diamagnetism). This rather sharp transition indicates that the indium content is fairly homogeneously distributed in the measured sample. From the resistivity measurements (Figure 3.10*a*), we see that only the samples with $x \gtrsim 0.10$ show superconductivity at accessible temperatures.

Superconducting transition temperatures T_c for all samples, obtained from magnetization and resistivity measurements, are summarized in Figure 3.11. The variation of T_c with x displays a similar relation as for In-substituted SnTe [1, 55] – with indium successively doped into the system, the superconducting critical temperature is enhanced. In the $(Pb_{0.5}Sn_{0.5})_{0.7}In_{0.3}Te$ solid solutions, a maximum in T_c at 4.7 K is achieved in both the magnetic and resistivity measurements.

To determine the upper critical field, the magnetic-field dependence of the electrical resistivity was also investigated. Representative data for $Pb_{0.35}Sn_{0.35}In_{0.3}Te$ are shown in Figure 3.12*a*. The onset of the resistive transition is plotted as a function of field in Figure 3.12*b* for $(Pb_{1-x}Sn_x)_{1-y}In_yTe$ single crystal samples with x=0.13, 0.16, 0.20 and 0.30. From these measures of $H_{c2}(T)$, we have determined the derivative, $|\partial H_{c2}/\partial T|_{T=T_c}$, as indicated by the fitted straight lines. These dependences provide estimates of the critical magnetic fields at zero temperature, $H_{c2}(T=0)$ [72]. Calculated values for the four superconducting single samples are com-

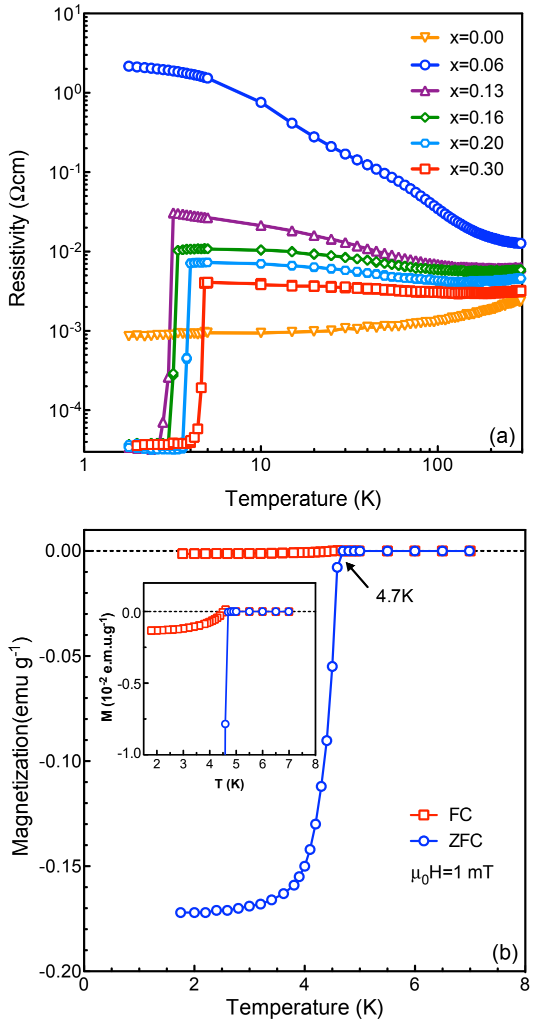

Figure 3.10: (a) Temperature dependence of the resistivity for $(Pb_{0.5}Sn_{0.5})_{1-x}In_xTe$ single crystals with indium contents x=0–0.30. (b) Temperature dependence of magnetic susceptibility for an optimally doped $(Pb_{0.5}Sn_{0.5})_{0.7}In_{0.3}Te$ single crystal measured under conditions of FC (red) and ZFC (blue) in an applied field of 1 mT.

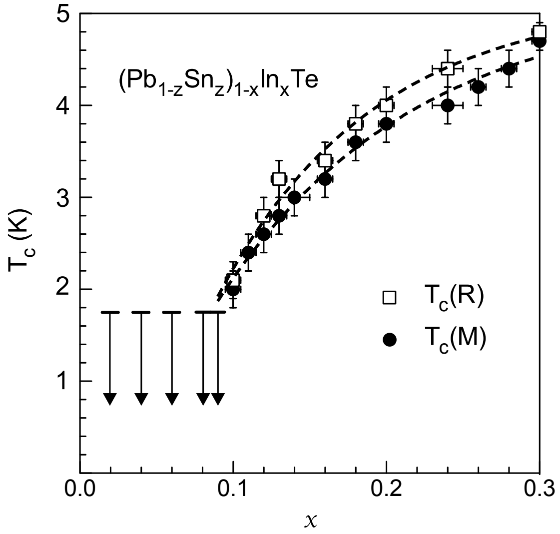

Figure 3.11: Superconducting transition temperature as a function of indium concentration x for $(Pb_{0.5}Sn_{0.5})_{0.7}In_{0.3}Te$ single-crystal samples, obtained from magnetization (solid circles) and resistivity (open squares) measurements. Horizontal error bars reflect the variation of indium concentration measured by EDS. The dashed lines are quides to the eye. Several samples with $x \leq 0.1$ were obtained, but any superconducting critical temperatures were lower than the instrument limit of 1.75 K, represented by arrows.

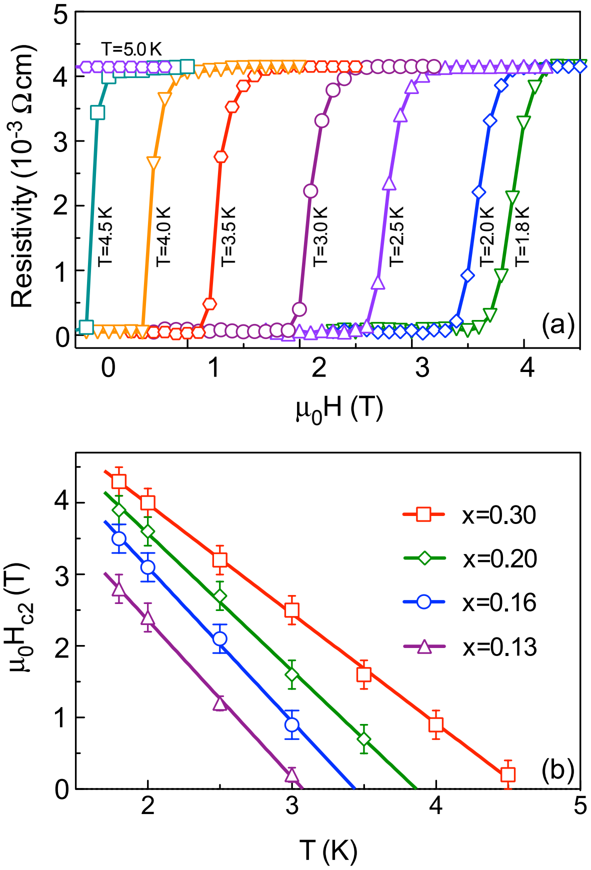

Figure 3.12: (a) Field dependence of the resistivity for the x=0.30 crystal at fixed temperature from 1.8 to 5 K. (b) Upper critical field $H_{c2}(T)$ determined from resistivity measurements on four single crystals.

Table 3.2: Upper critical field at zero temperature $H_{c2}(T = 0)$ for $(Pb_{1-x}Sn_x)_{1-y}In_yTe$.

Indium concentration	T_c (K)	slope (T/K)	$\mu_0 H_{c2}(0)$ (T)
0.13	3.2	-2.20	4.86(7)
0.16	3.4	-2.16	5.07(8)
0.20	4.0	-1.85	5.11(4)
0.30	4.8	-1.54	5.10(3)

pared in Table 3.2. We find that $\mu_0 H_{c2}(0)$ changes relatively little with x in comparison with T_c for the superconducting samples.

3.3 Indium substitution effect on (Pb,Sn)Te: Topological properties

3.3.1 Resistivity behaviors of indium doped $Pb_{1-x}Sn_xTe$

Based on the transport measurements of indium doped $Pb_{0.5}Sn_{0.5}Te$ crystal samples, we noticed the striking, nonmonotonic variation in the normal-state resistivity with x, as illustrated in Figure 3.13. Pure $Pb_{0.5}Sn_{0.5}Te$ shows a metallic-like behavior with a p-type carrier density similar to SnTe. By introducing increasing amounts of indium into the $Pb_{0.5}Sn_{0.5}Te$ system, single crystal samples show quite divergent, nonmonotonic variations in resistivity in the normal state. For the samples with one percent or less indium, the resistivity is weakly metallic, just like the resistivity behavior of pure SnTe [1] or $Pb_{1-x}Sn_xTe$ without indium doping [73]. Increasing y to 0.06, we observe that the resistivity at 10 K rises by five orders of magnitude. With further increases of y, the resistivity drops, but remains

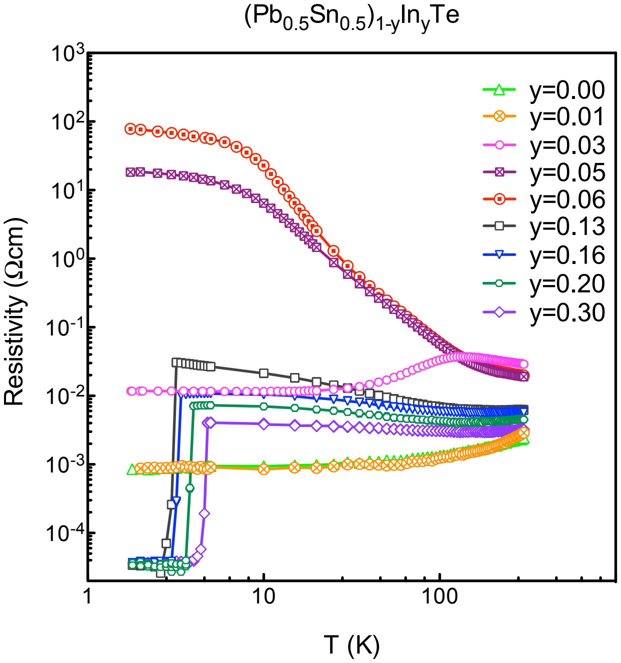

Figure 3.13: Temperature dependence of the resistivity for $(Pb_{0.5}Sn_{0.5})_{1-y}In_yTe$ single crystals with indium contents $0 \leq y \leq 0.30$.

semiconducting, consistent with earlier studies [2, 74, 75]. This resistivity behavior in the normal state is quite different from the case of In doped SnTe [1], where all samples are weakly metallic in the normal sate. At low temperature, samples show true bulk-insulating resistivity and present evidence for nontrivial topological surface states [3]. With higher indium doping levels, superconductivity with a transition temperature T_c positively correlated to the indium concentration was observed, and the highest T_c, $\sim$4.7 K, was achieved for 45% indium doped SnTe samples [1, 55] and 30% indium doped $Pb_{0.5}Sn_{0.5}Te$ samples [3].

The effect of indium substitution is similar for other (Pb,Sn)Te compositions. Nonmonotonic variation in the normal-state resistivity with y is also found in transport measurements of PSIT for many series with different x values. Specifically, x=0.5 is not the only system that shows large bulk resistance when doped with a low concentration of indium. In the whole family of $(Pb_{1-x}Sn_x)_{1-y}In_yTe$, maximum resistivities that surpass 10^6 Ωcm are observed for x=0.25-0.30. Even for x=0.35, doping with 6% In results in a rise in resistivity by 6 orders of magnitude at low temperature. These phenomena can be well explained in a picture where the chemical potential is pinned within the band gap, which will be discussed in detail in a later section 3.3.2.

Past studies [76, 77] of various transport properties in $Pb_{1-x}Sn_xTe$ and the impact of In doping provide a basis for understanding the present results. For In concentrations of $\lesssim$0.06, the In sites introduce localized states at a sharply defined energy that pins the chemical potential. In a small range of Sn concentration centered about $x=$0.25, the chemical potential should be pinned within the band gap. Hence, the very large bulk resistivities observed for $x=$0.25 and 0.3 are consistent with truly insulating bulk character.

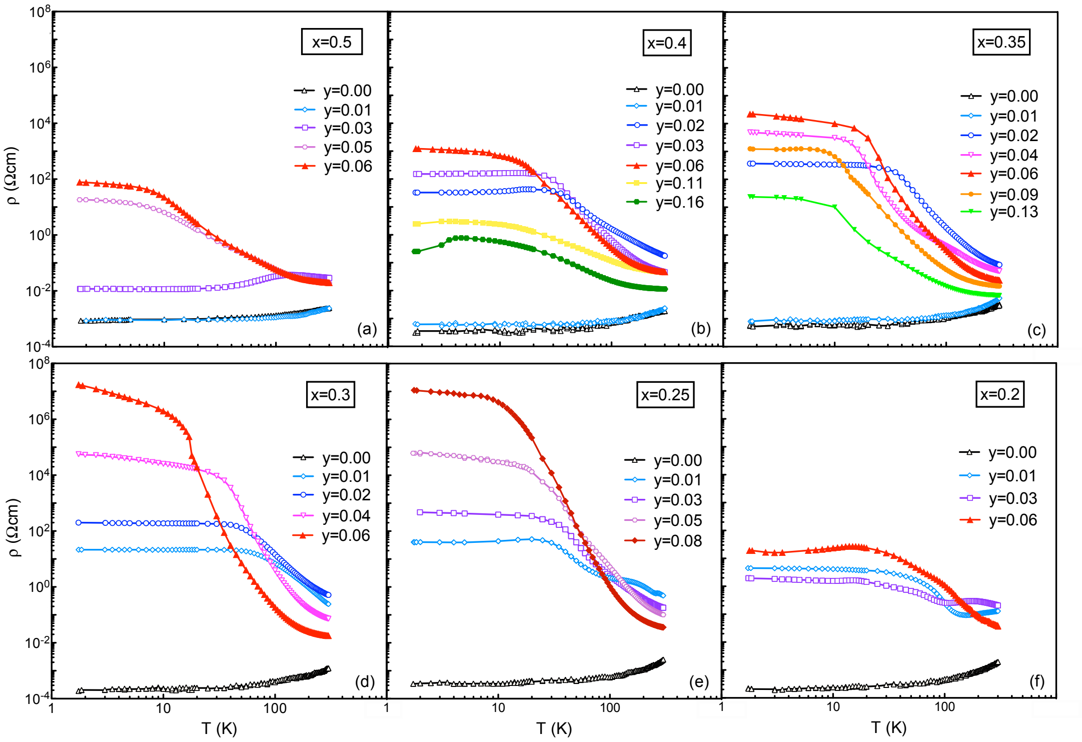

Figure 3.14: Temperature dependence of resistivity in $(\mathrm{Pb}_{1-x}\mathrm{Sn}_x)_{1-y}\mathrm{In}_y\mathrm{Te}$ for (a) x =0.5, (b) x =0.4, (c) x =0.35, (d) x =0.3, (e) x =0.25, and (f) x =0.2; the values of y are labeled separately in each panel. For each value of x, indium doping turns the metallic parent compound into an insulator, with low-temperature resistivity increasing by several orders of magnitude. The saturation of resistivity at temperatures below 30 K suggests that the surface conduction becomes dominant.

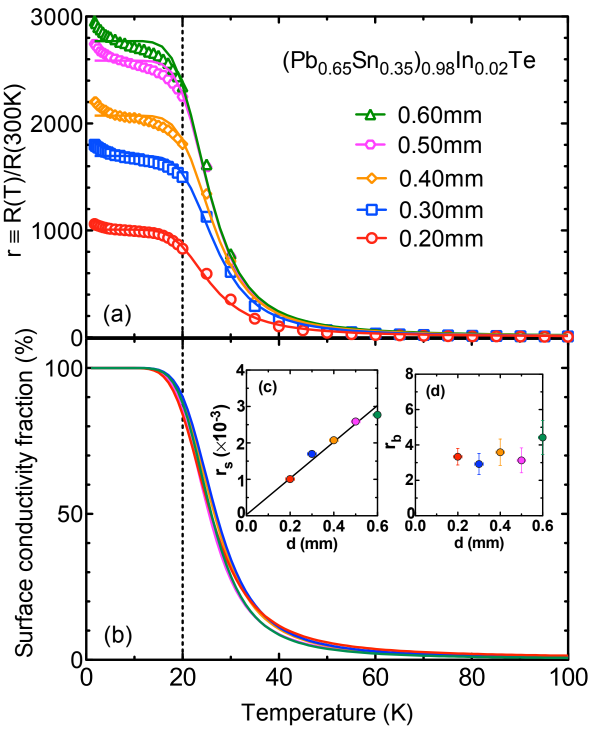

Figure 3.15: (a) Resistance normalized to its room-temperature value for several thickness of $(Pb_{0.65}Sn_{0.35})_{0.98}In_{0.02}Te$. Lines are fits as described in the text. Results for fitting parameters r_s and r_b are shwon in panels (c) and (d), respectively. (b) Fraction of conductivity due to surface states calculated from the fit parameters.

Now we concentrate on testing the character of the $x = 0.35$, $y = 0.02$ sample, where we anticipate topological surface states. To test the contribution of the surface states to the sample conductivity, we have measured the resistance $R(T)$ as a function of sample thickness [78–80]. The measurements involved sanding the bottom surface of the crystal with the top contacts remaining nominally constant. Following Syers *et al.* [80], in Figure 3.15*(a)* we plot the ratio $r \equiv R(T)/R(300\ \mathrm{K})$ for several thicknesses. A simple parallel conductance model is used to extract the relative contributions, with total conductance described by

$$G = G_s + G_b, \tag{3.1}$$

where G_s=$1/R_s$ is the surface contribution–assumed to be temperature independent–and G_b=$1/R_b$ is the bulk contribution–assumed to be activated in temperature due to a bulk energy gap Δ. Therefore, G_b=$Wt(\rho_b L)e^{-\Delta/k_\mathrm{B}T}$ with sample length$L$, with W, and thickness t, bulk resistivity ρ_b in the high-temperature limit, and Boltzmann constant k_b. Thus, for the dimensionless and geometry-independence resistance ratio,

$$r(T)^{-1} = r_s^{-1} + r_b^{-1} e^{\Delta/k_\mathrm{B}T}, \tag{3.2}$$

where subscripts s and b label the surface and bulk contributions, respectively. The fitted results for r_s and r_b are plotted in Figure 3.15*(c)* and *(d)*; for the gap, we obtain $\Delta = 14.6 \pm 0.3$ meV. The parameter r_s, essentially the ratio of the bulk conductance at 300 K to the surface conductance, linearly extrapolates to zero in the limit of zero thickness. Alternatively, we can calculate the fraction of the conductivity in the surface channel, which is plotted in Figure 3.15*(b)*. Despite the fact that the sample thicknesses are quite large, we find that the surface states provide $>$90% of the conduction for T<20 K.

As another test, the Hall effect and zero-field resistivity were measured on a x =0.35, y =0.02 crystal using a Quantum Design Physical Property Measurement System. From those measurements, we obtained the carrier density n and mobility μ shown in Figure 3.16*(a)* and *(b)*, respectively. The carrier density drops rapidly on cooling, falling below $10^{14}/cm^3$ at 5 K, while the mobility rises rapidly below 20 K, eventually surpassing 2000 cm^2 V^{-1} s^{-1}, consistent with metallic conduction by surface states and negligible bulk contribution at low temperature.

As can be seen in Figure 3.16, the surface conduction channel exists and dominates the low temperature transport on both topological and trivial sides of the phase diagram. Therefore, we perform the final test of the topological character of the surface states with magnetoresistance (MR) measurements [81]. The symmetry-protected coupling of spin and momentum for surface states makes them immune to weak localization effects. Application of a transverse magnetic field violates the relevant symmetries [82], thus removing the topological protection and leading to a field-induced decrease in conductance. Combining the longitudinal and transverse resistivity data, we have evaluated the field-dependent longitudinal conductivity. Results at 5 K and 20 K are plotted in Figure 3.16*(c)* and *(d)*, respectively.

For a quantitative analysis, we fit the data with the theoretical formula for weak anti localization (WAL) [83],

$$\Delta G = \frac{\alpha}{\pi}\frac{e^2}{h}[\ln(B_\phi/B) - \psi(\tfrac{1}{2} + B_\phi/B)], \tag{3.3}$$

where ψ is the digamma function and α is a number equal to $1/2$ times the number of conduction channels; $B_\phi = \Phi_0/(8\pi l_\phi^2)$, with $\Phi_0 = h/e$ and

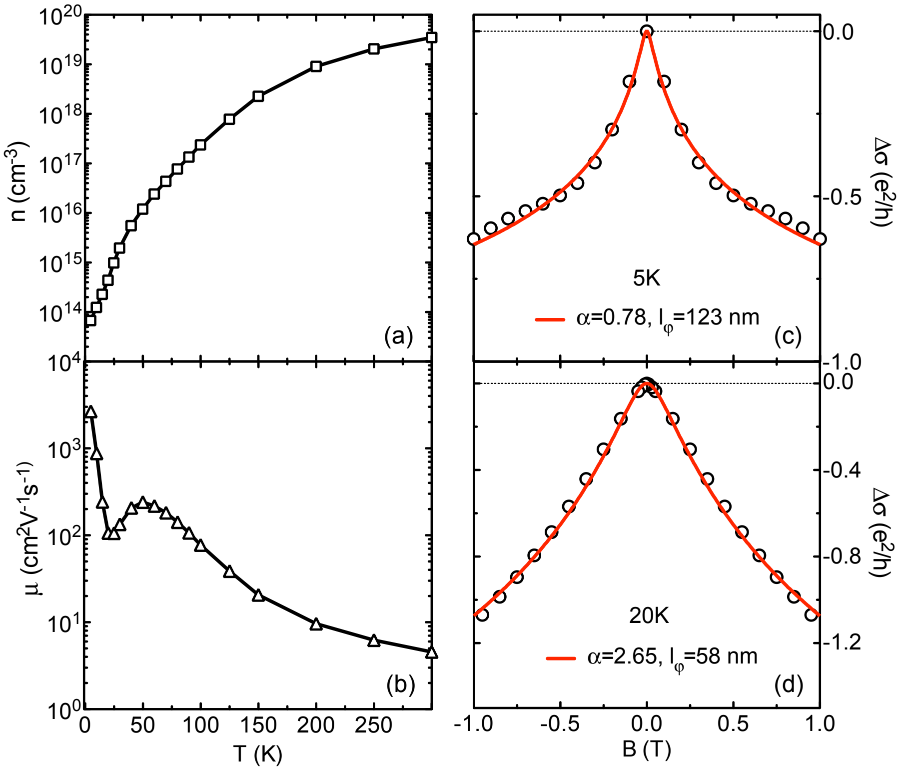

Figure 3.16: Characterizations of the $(Pb_{0.65}Sn_{0.35})_{0.98}In_{0.02}Te$ sample. (a) Carrier density, obtained from Hall effect measurements, and (b) carrier mobility vs. T; lines are guides to the eye. (c) Change in magnetoconductivity with field at 5 K and (d) 20 K. Red lines represent fits to the WAL formula, Eq. 3.3, as discussed in the text. For the initial magnetoresistance data used to obtain $\sigma(B)$, the measurements were performed after a significant waiting time (5 days at 5 K, 2 days at 20 K) due to slow relaxation in the resistance [77].

l_ϕ being the electronic phase coherence length. For our system, one expects 4 Dirac cones crossing the Fermi surface [84, 85], which would give $\alpha = 2$. The fit to the 5-K data yields $\alpha = 0.78$ and $l_\phi = 123$ nm; at 20 K, the fit gives $\alpha = 2.65$ and $l_\phi = 58$ nm. The reduction in coherence length with temperature is consistent with the drop in mobility. The magnitude of α is qualitatively consistent with expectations, though the temperature dependence is unexpected. Note that for the $x = 0.5$, $y = 0.06$ sample, the magnetoresistance was measured at 5 K; a fit of the WAL formula to the data yields $l_\phi = 100$ nm and $\alpha = 2.25$, close to the expected $\alpha = 2$.

3.3.2 Bulk band structure of indium doped $Pb_{1-x}Sn_xTe$

To address the divergent resistivity behaviors, it is helpful to consider the bulk electronic structure. SnTe and other IV-VI materials with the rock-salt structure have long attracted attention as a model for small band gap semiconductors. The topologically distinct band structure of SnTe (non-trivial, $x = 1$) and PbTe (trivial, $x = 0$) involves a change in the ordering of the conduction and valence bands at L points. This implies that the band gap of the alloy $Pb_{1-x}Sn_xTe$ first closes and then re-opens as x increases, as shown in Figure 3.17[4, 77, 86, 87]. It follows that there must be a topological quantum phase transition upon varying the Pb/Sn ratio in $Pb_{1-x}Sn_xTe$, and experiments indicate that it occurs near $x_c \approx 0.35$ at low temperature[32, 86–90].

Generally, it is believed that each In dopant will provide one less valence electron than Sn^{2+} and Pb^{2+}, so that indium should be considered as a p-type dopant. In the case of SnTe, one begins with a p-type semiconductor due to Sn vacancies. With In doping, the number of cation

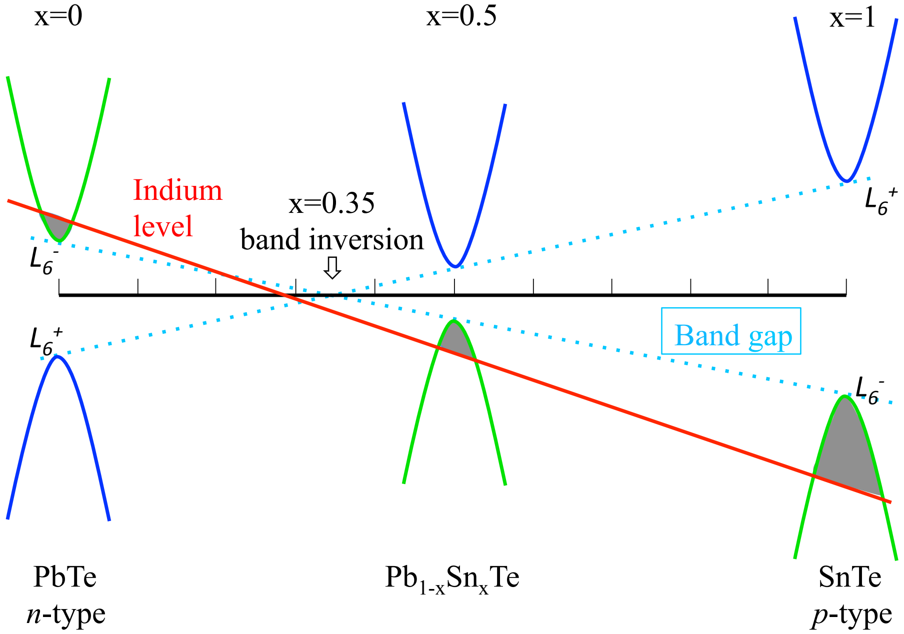

Figure 3.17: Energy diagrams illustrating the relative location of the conduction, valence band and indium induced impurity band in the continuous series of $Pb_{1-x}Sn_xTe$ alloys with low In doping level, where indium can be simply treated as a *p*-type dopant. In SnTe, the conduction band has a symmetry of L_6^+; this undergoes a band inversion at x ~0.35 and the symmetry is inverted in PbTe. The band gap is illustrated with blue dashed lines, with the end member SnTe having 360 meV and PbTe having 190 meV [91]. The Fermi level, controlled by the indium impurity states, is indicated schematically by the red line.

vacancies decreases, which partially compensates the expected impact of the In; nevertheless, the p-type carrier density initially grows with increasing In concentration [56, 92]. The situation becomes more complicates for an Indium concentration above 10%, where the sign of the Hall resistivity changes [70], suggesting the possibility that two types of carriers are simultaneously present. In fact, in indium doped PbTe and $\mathrm{Pb}_{1-x}\mathrm{Sn}_x\mathrm{Te}$, In-doping results in far less than 1 electron per impurity atom, which suggests In doping also introduces an impurity band that causes the effect of pinning the Fermi level[52, 91]. Evidence for the quasi-localized character of indium-induced states has been provided by a recent nuclear magnetic resonance study on $\mathrm{Sn}_{0.9}\mathrm{In}_{0.1}\mathrm{Te}$[93].

In this scenario, the large bulk resistivity in series with x =0.25–0.35 is a consequence of indium sites introducing localized impurity states that pin the chemical potential[77, 86]; the electronic properties then depend on the position and width of the indium level. In the region of compositions where the localized impurity band lies in the band gap, or a position that is very close to the band edge, the free carrier concentration is extremely low at low temperature, which is reflected in the very large bulk resistivities for $x \sim 0.30$ that we observe in the transport measurements.

According to the schematic evolution of the band structure of $\mathrm{Pb}_{1-x}\mathrm{Sn}_x\mathrm{Te}$ and the energy of the In impurity level in Fig. 3.17, the chemical potential sits in the valence band on the Sn side, consistent with p-type metallic behavior, while it moves to the conduction band on the Pb-rich side. With a very small amount of indium doping on the Pb-rich side, the opposing trends of decreasing cation vacancies and increasing In-substitution initially lower the carrier density, leaving the system weakly metallic. With further increases in In content, the Fermi level drops into the band gap, where it gets pinned by the impurity state level. The magnitude of the

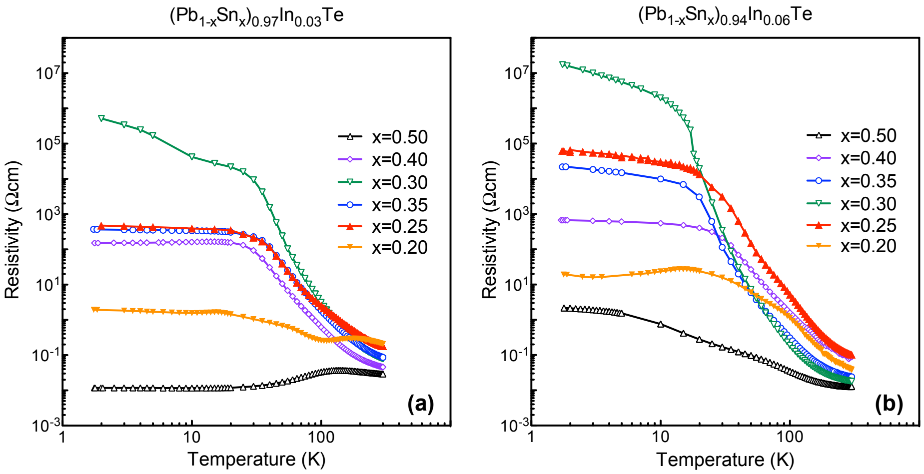

Figure 3.18: Temperature dependence of the resistivity for $(Pb_{1-x}Sn_x)_{0.97}In_{0.03}Te$ (a) and $(Pb_{1-x}Sn_x)_{0.94}In_{0.06}Te$ (b) single crystals. The resistivity value are shown in a logarithmic scale.

resistivity will then depend largely on the size of the band gap, which is determined by the Sn content, x, instead of the indium content, y[77]. Figure 3.18 gives a summary of the variation in resistivity as a function of x in $(Pb_{1-x}Sn_x)_{1-y}In_yTe$ compounds with either 3% or 6% indium doping. The same trends are found as a function of x, although the low-temperature resistivities tend to be higher for y =0.06.

It is worth mentioning that a long relaxation time was observed in the bulk resistance for several samples, especially those that are truly bulk insulators, i.e. x =0.25, 0.30, 0.35. After a sample was quenched down to low temperature (liquid-helium), its resistivity gradually decreased with time. This relaxation phenomenon can last for days until the resistivity reaches a stable value. Previous studies on $Pb_{1-x}Sn_xTe$ doped with group-III elements revealed similar time-dependent behavior, and it was explained in terms of the interaction between the crystal lattice and the non-equilibrium electron densities associated with the pinned chemical potential at the impurity level[86].

3.3.3 Physical property phase diagram of $(\mathrm{Pb}_{1-x}\mathrm{Sn}_x)_{1-y}\mathrm{In}_y\mathrm{Te}$

To summarize the effect of indium substitution on PSIT materials, we present in Figure 3.19 [4], a ternary phase diagram of the system to illustrate trends for several properties: the character of the low-temperature resistivity (metallic, insulating, superconducting) and the solubility limit. Here, the end members are SnTe, PbTe, and InTe. The closer to the end member, the higher concentration of that component. Each of the six dashed lines starting with the same end member InTe represent a series of PSIT with the fixed Sn:Pb ratios, as labeled by x.

For low indium doping (blue region), samples show weak metallic resistivity, as in SnTe. A few percent indium doping turns the $\mathrm{Pb}_{1-x}\mathrm{Sn}_x\mathrm{Te}$ samples into true insulators (orange region). By increasing the In content further, superconductivity may be achieved (green region). When the indium content exceeds the solubility limit in the system (marked with white crosses), where additional In is no longer simply substituting for Pb/Sn, an impurity phase of InTe, with a tetragonal crystal structure, appears and the samples are no longer in single phase. The critical In concentrations that divide these various regions are illustrated with dashed lines.

From the resistivity behavior in the phase diagram, it can be seen that the In substitution effect shows consistent trends. Superconductivity emerges almost immediately with indium doping in SnTe. In $\mathrm{Pb}_{1-x}\mathrm{Sn}_x\mathrm{Te}$, though, with increasing Pb content the amount of In needed to induce superconductivity goes up, and the range of superconductivity with respect

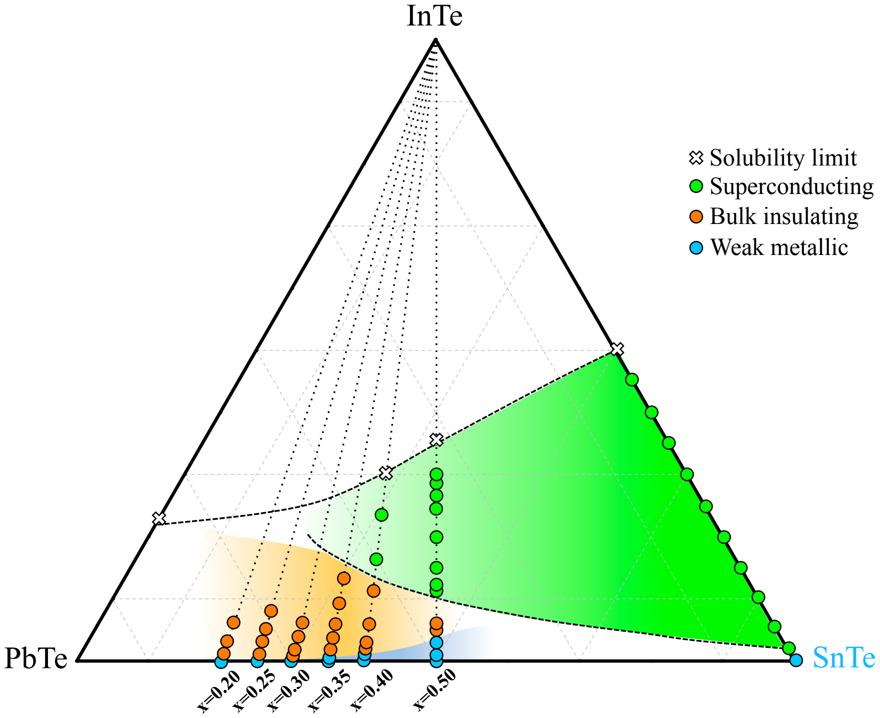

Figure 3.19: A ternary phase diagram summarizing all the resistivity behaviors of $(Pb_{1-x}Sn_x)_{1-y}In_yTe$. Experimental results for SIT with In content up to 10% is obtained from Ref. [54]. The solubility limit of In in PbTe (24%) is obtained from Ref. [77]. Samples with weak metallic resistivity are shown in blue, with insulating resistivity are shown in orange, and with superconductivity are shown in green. White crosses represent the solubility limit of In, beyond which the sample no longer remains in a single phase and secondary InTe phase shows up.

to In-doping shrinks. Meanwhile, the bulk insulating region broadens with increased Pb, and the maximum bulk resistivity that can be achieved in the PSIT family is found in the x=0.30 and x=0.25 series[3]. Those materials along with previously reported bulk insulating TIs Sn-$Bi_{1.1}Sb_{0.9}Te_2S$[94] could provide good platforms to study the true topological 'insulators', in which bulk conduction would not dominate the transport behavior, assuming that their surface states remain topological.

3.4 Probing the nature of the superconducting topological materials by neutron scattering

3.4.1 Debate on topological superconductivity

At higher indium content (>10%), superconductivity emerges in $Pb_{1-x}Sn_xTe$ samples, with a typical superconducting transition temperature in the range of 3 to 5 K. There are intriguing questions about the nature of the superconductivity: is it conventional BCS superconductivity, or unconventional topological superconductivity? Topological superconductors are accompanied by gapless states at the edge or surface, which characterize the nontrivial topology of the bulk state and they may be composed of *Majorana fermions* [39, 40].

The first plausible example of TSC (associated with TI or TCI compounds) was $Cu_xBi_2Se_3$[45]. Experimental evidence from point-contact spectroscopy[49, 95] showing zero-bias conductance peaks coexisting with a superconducting gap may be indicative of the unconventional superconductivity, which is necessary (but not sufficient) for TSC in inversion symmetric, time-reversal-invariant superconductors. Similarly, results for

In-doped SnTe from both point-contact spectroscopy and high-resolution ARPES studies have been interpreted as evidence for odd-parity pairing and topological superconductivity [51, 64].

A markedly different conclusion was drawn, however, in a scanning tunnelling spectroscopy (STS) study on $Cu_{0.2}Bi_2Se_3$ [96], which reported a superconducting gap without any zero bias anomalies. Later studies on the optimally doped TCI system SIT using thermal conductivity [97], magnetization and muon-spin rotation (μSR) measurements [98] also supported the conclusion that SIT has a full superconducting gap in the bulk, and is more likely to be a conventional s-wave superconductor. Similarly, STS measurements [71] of the superconducting state as well as the superconducting energy gap in $(Pb_{0.5}Sn_{0.5})_{0.7}In_{0.3}Te$ on the high-symmetry (001) surface lead to the same conclusion, that the superconducting sample seems to be fully gapped without any in-gap states, contrary to the expectations for a topological superconductor.

These controversies may be due to the complexity of the junctions in point contact measurements, since the spectra that are indicative of an unconventional superconductor can also be interpreted by other mechanisms [71, 95]. On the other hand, the observed fully-gapped tunneling spectra in STM measurements on $Cu_xBi_2Se_3$ and SIT can be also explained by the results of exotic pairing states with additional parameters [96]. In addition, in TCI compounds where the exotic surface states only exist on certain high-symmetry planes guaranteed by the mirror symmetry, the possibility of topological superconductivity feature cannot be ruled out from studies of the (001) plane alone [71]. Besides, due to the poor cleavability of cubic $(Pb_{1-x}Sn_x)_{1-y}In_yTe$, it might be tricky to expose the desired surface for surface-sensitive measurements.

The debate on topological superconductivity has recently been reinvigorated by a nuclear magnetic resonance study of $Cu_{0.3}Bi_2Se_3$ [99]. There the authors find clear evidence for a breaking of the spin-rotation symmetry in the superconducting state, consistent with spin-triplet pairing. This will surely motivated further investigations.

3.4.2 Phonon-mediated superconductivity in In-doped $Pb_{0.5}Sn_{0.5}Te$ studied by neutron scattering

In order to probe the nature of the superconductivity in the topological materials, inelastic neutron scattering may provide another perspective to this long-standing controversy by studying the phonon density of states (DOS) of the superconducting topological materials. An essential issue of the previously mentioned debate is related to the character of the superconducting gap. Typically, electron-phonon coupling should play an essential role in an conventional Bardeen–Cooper–Schrieffer (BCS) superconductor. In this case, one can expect some phonon anomalies across the superconducting transition temperature T_c. In this section, I present inelastic neutron scattering results on the phonon spectra in $(Pb_{0.5}Sn_{0.5})_{0.7}In_{0.3}Te$ to address this issue.

Previous studies have been done on low-energy phonons on the $Sn_{0.8}In_{0.2}Te$ single-crystal sample [100]. The low energy (close to the Bragg tail) of the acoustic phonons makes it difficult to draw a definite conclusion, and there appears to be no clear change on the acoustic phonon modes when crossing T_c. There is a proposal that in the topological superconductor system, the transverse optical (TO) phonon plays a more important role for pairing [64], thus a better way to investigate phonon anomalies is to focus on the optical branches.

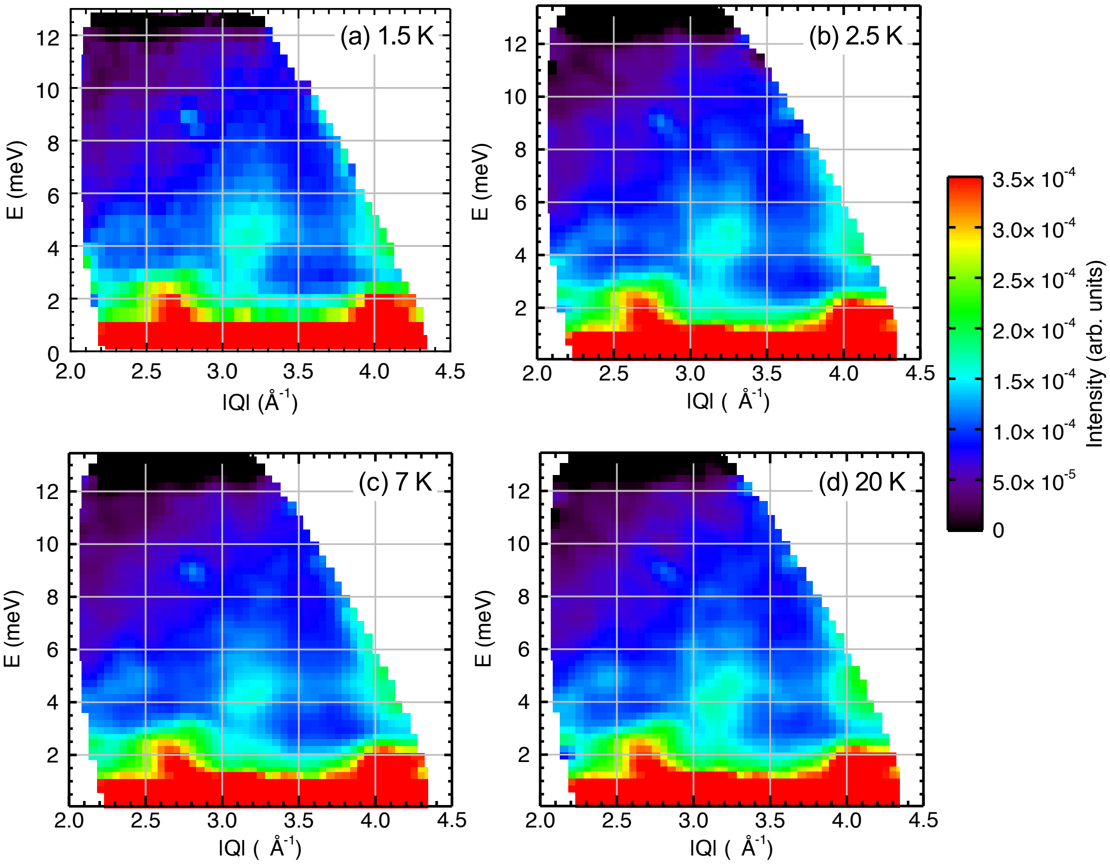

Figure 3.20: |**Q**| dependence of phonon intensity $S(Q, E)$ at all E range measured on $(Pb_{0.5}Sn_{0.5})_{0.7}In_{0.3}Te$ powder sample at temperatures: (a) 1.5 K, (b) 2.5 K, (c) 7 K and (d) 20 K.

In order to understand the role phonons play in the superconductivity in the bulk of $(Pb_{0.5}Sn_{0.5})_{0.7}In_{0.3}Te$, inelastic neutron scattering measurements over a wide **Q**-E range have been performed on the optimally doped topological crystalline insulator $Pb_{1-x}Sn_xTe$, $(Pb_{0.5}Sn_{0.5})_{0.7}In_{0.3}Te$ powder sample (20 g, T_c =4.7 K). Fine structure in its phonon density of states as well as the **Q** dependence of the excitations was revealed by means of a high-energy-resolution chopper spectrometer HYSPEC at a pulsed neutron source SNS, which covers large range of **Q** and also has good resolution at low energy range. In order to achieve best resolution, we selected incident energy E_i=15 meV, Fermi chopper frequency 360 Hz. In this configuration, we can achieve an energy resolution $\approx$0.2 meV.

|**Q**| dependence of phonon intensity $S(Q,E)$ over the accessible E range were measured at four different temperatures, below and above the T_c, as shown in Figure 3.20. The scattering around 5 meV is prominent, with the strength increasing with increasing |**Q**|. Such **Q** dependence of the scattering intensities is consistent with them being resulting from phonons. Though, in order to directly compare the phonon DOS measured at different temperatures, the phonon thermal correction, *i.e.*, Bose factor correction is necessary [101]. Based on the Planck distribution:

$$P(n) = \frac{1}{Z} exp(-\frac{E_n}{k_\mathrm{B} T}) \tag{3.4}$$

where Boltzmann constant k_b=1.3806503$\times$ 10^{-23} J/K, and T is absolute temperature. E_n is the energy carried by the n phonons. Z is the normalization factor, or the partition function. Due to the total probability of

$$\sum_{n=1}^{\infty} P(n) = 1$$

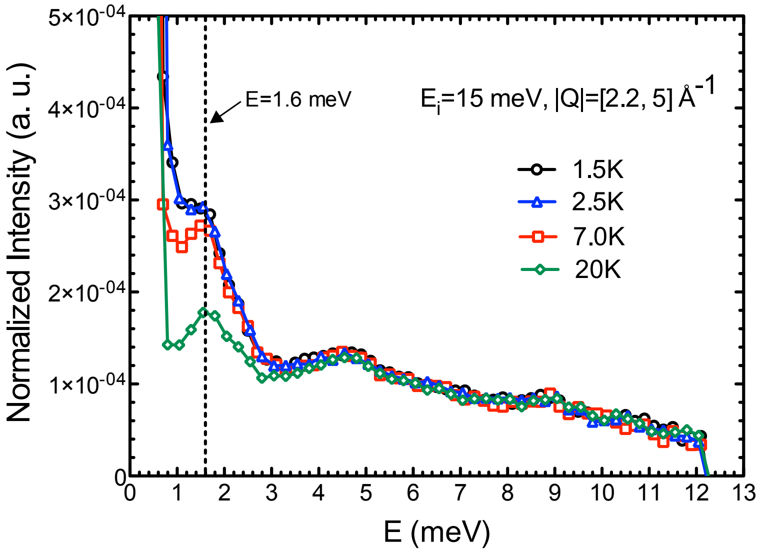

Figure 3.21: Energy dependence of phonon density of states intensity, normalized after phonon thermal correction.

, we have

$$\frac{1}{Z} = 1 - exp(-\frac{E}{k_B T}). \tag{3.5}$$

Thus we can then do the Bose factor correction by

$$S(\mathbf{Q}, \mathbf{E})_{corr.} = S(\mathbf{Q}, \mathbf{E}) \times \frac{1}{Z}. \tag{3.6}$$

We sum the intensities S(**Q**, E) with **Q** ranging from 2.2 to 5 , dividing them by the Bose factor. Figure 3.21 shows the energy dependence of the phonon DOS intensity after Bose factor correction at four different temperatures. We found the E dependence is very similar above and below T$_c$ above 3 meV, but shows differences below 3 meV. Below 3 meV, curves of T=1.5 (black) and 2.5 K (blue) overlap each other, while when above T$_c$, the phonon DOS intensity gets suppressed.

BCS theory predicts the dependence of the value of the energy gap Δ at temperature T on the critical temperature T_c. The ratio between the value of the energy gap at zero temperature and the value of the superconducting transition temperature takes the universal value:

$$\Delta(T=0) = 1.764 k_{\mathrm{B}} T_c, \tag{3.7}$$

Based on this we estimate the possible phonon DOS anomaly should appear at $2\Delta(0) \approx$1.6 meV, which is coincident with the energy where we found the difference in intensity at temperature below and above T_c. The substantial enhancement of the phonon scattering strongly demonstrates that the low-energy phonons are coupled with the superconducting pairing.

Our results show that for the superconducting sample the scattering intensities for phonons with energies $E \leqslant 2\Delta(0)$ (zero-temperature superconducting gap) are significantly enhanced below T_c, and the In-doping effectively alters the phonon density of states. Our results seem to indicate that the phonons play a role in the superconductivity in $(Pb_{0.5}Sn_{0.5})_{0.7}In_{0.3}Te$, and the soft phonons are coupled to the electrons in some way, suggesting they could be relevant to superconductivity. However, a ferroelectric transition also involves in the interactions with low-energy phonons in $Pb_{1-x}Sn_xTe$ materials, thus this is still an open question whether the phonon DOS anomaly observed in our INS experiment suggests the superconductivity in $(Pb_{0.5}Sn_{0.5})_{0.7}In_{0.3}Te$ is a consequence of the electron-phonon interactions, similar as that in conventional BCS superconductor, instead of the unconventional topological superconductor.

3.5 Conclusions and discussions

In recent years, In-doped SnTe and $Pb_{1-x}Sn_xTe$ have been studied extensively both as examples of topological crystalline insulators and potentially-interesting superconductors. Our study of a broad range of compositions in the (Pb,Sn)Te system shows that indium doping has a nonmonotonic effect on the electronic properties, which can be explained from the standpoint of the relative location of the indium-induced impurity band and the bulk band structure. Our studies show that with 1-2% indium doping, the samples remain weakly metallic just as the undoped parent compounds; with a few more percent of indium concentration, the samples become insulating and the low temperature conductance is dominated by the surface states; superconductivity can be achieved with more indium doping, and the superconducting transition temperature increases with increasing indium; the maximum T_c is limited by the indium solubility in the parent compounds. In this dissertation we have presented an overview and summary which recaps our findings and conclusions, which can be instructive for future work on this system.

In the effort of looking for a new topological superconductor, Tl_5Te_3 has been found to be tunable between superconducting and topological surface states by Sn-substitution[102, 103], which is quite similar to the In-substitution effect on the $Pb_{1-x}Sn_xTe$ system. These facts may imply that the topological surface states and the bulk superconductivity are two competing parameters. The goal of mixing the superconducting and topological characters remains a challenge.

A plausible strategy of looking for *Majorana fermions* is to artificially construct topological insulator/conventional superconductor heterostructures and make use of the superconducting proximity effect[104–109].

Both $Sn_{1-x}In_xTe$ and $(Pb_{1-x}Sn_x)_{1-y}In_yTe$ would be perfect platforms for this purpose, since these systems undergo a continuous change from a TCI to a (likely conventional) superconductor. More specifically, the large bulk resistivity shows up in $(Pb_{1-x}Sn_x)_{1-y}In_yTe$ with $x =$0.25–0.5, a p-type matrix can be realized in series the with $x =$0.35–1.0, and superconductivity can also be realized in the latter compounds, which makes this system quite promising for exploitation in heterostructures.

References

[1] R. D. Zhong, J. A. Schneeloch, X. Y. Shi, Z. J. Xu, C. Zhang, J. M. Tranquada, Q. Li, and G. D. Gu. Optimizing the superconducting transition temperature and upper critical field of $Sn_{1-x}In_xTe$. *Phys. Rev. B*, 88:020505, July 2013.

[2] R. D. Zhong, J. A. Schneeloch, T. S. Liu, F. E. Camino, J. M. Tranquada, and G. D. Gu. Superconductivity induced by in substitution into the topological crystalline insulator $Pb_{0.5}Sn_{0.5}Te$. *Phys. Rev. B*, 90:020505, Jul 2014.

[3] Ruidan Zhong, Xugang He, J. A. Schneeloch, Cheng Zhang, Tiansheng Liu, I. Pletikosić, T. Yilmaz, B. Sinkovic, Qiang Li, Wei Ku, T. Valla, J. M. Tranquada, and Genda Gu. Surface-state-dominated transport in crystals of the topological crystalline insulator in-doped $Pb_{1-x}Sn_xTe$. *Phys. Rev. B*, 91:195321, May 2015.

[4] Ruidan Zhong, John Schneeloch, Qiang Li, Wei Ku, John Tranquada, and Genda Gu. Indium substitution effect on the topological crystalline insulator family $(Pb_{1-x}Sn_x)_{1-y}In_yTe$: topological and superconducting properties. *Crystals*, 7(2):55, 2017.

[5] M. Z. Hasan and C. L. Kane. Colloquium: Topological insulators. *Rev. Mod. Phys.*, 82:3045–3067, Nov 2010.

[6] Xiao-Liang Qi and Shou-Cheng Zhang. Topological insulators and superconductors. *Rev. Mod. Phys.*, 83:1057–1110, Oct 2011.

[7] Yoichi Ando. Topological insulator materials. *Journal of the Physical Society of Japan*, 82(10):102001, 2013.

[8] Charles Kane and Joel Moore. Topological insulators. *Physics World*, 24(02):32, 2011.

[9] C. L. Kane and E. J. Mele. Z_2 topological order and the quantum spin Hall effect. *Phys. Rev. Lett.*, 95:146802, 2005.

[10] B. Andrei Bernevig, Taylor L. Hughes, and Shou-Cheng Zhang. Quantum spin hall effect and topological phase transition in HgTe quantum wells. *Science*, 314(5806):1757–1761, 2006.

[11] Liang Fu and C. L. Kane. Topological insulators with inversion symmetry. *Phys. Rev. B*, 76:045302, Jul 2007.

[12] Liang Fu, C. L. Kane, and E. J. Mele. Topological insulators in three dimensions. *Phys. Rev. Lett.*, 98:106803, Mar 2007.

[13] Haijun Zhang, Chao-Xing Liu, Xiao-Liang Qi, Xi Dai, Zhong Fang, and Shou-Cheng Zhang. Topological insulators in Bi_2Se_3, Bi_2Te_3 and Sb_2Te_3 with a single dirac cone on the surface. *Nat Phys*, 5(6):438–442, 06 2009.

[14] Y. Xia, D. Qian, D. Hsieh, L. Wray, A. Pal, H. Lin, A. Bansil, D. Grauer, Y. S. Hor, R. J. Cava, and M. Z. Hasan. Observation of a large-gap topological-insulator class with a single Dirac cone on the surface. *Nat Phys*, 5(6):398–402, 06 2009.

[15] Y. L. Chen, J. G. Analytis, J.-H. Chu, Z. K. Liu, S.-K. Mo, X. L. Qi, H. J. Zhang, D. H. Lu, X. Dai, Z. Fang, S. C. Zhang, I. R. Fisher, Z. Hussain, and Z.-X. Shen. Experimental realization of a three-dimensional topological insulator, Bi_2Te_3. *Science*, 325(5937):178–181, 2009.

[16] Zheng-Cheng Gu and Xiao-Gang Wen. Tensor-entanglement-filtering renormalization approach and symmetry-protected topological order. *Phys. Rev. B*, 80:155131, Oct 2009.

[17] Frank Pollmann, Erez Berg, Ari M. Turner, and Masaki Oshikawa. Symmetry protection of topological phases in one-dimensional quantum spin systems. *Phys. Rev. B*, 85:075125, Feb 2012.

[18] Xie Chen, Zheng-Xin Liu, and Xiao-Gang Wen. Two-dimensional symmetry-protected topological orders and their protected gapless edge excitations. *Phys. Rev. B*, 84:235141, Dec 2011.

[19] H. Lin, R.S. Markiewicz, L.A. Wray, L. Fu, M.Z. Hasan, and A. Bansil. Single-dirac-cone topological surface states on pseudo-IV-VI-semimetal/semiconductors: Thallium-based III-V-VI2 ternary chalcogenides. *arXiv*, 1003.2615, 2010.

[20] Binghai Yan, Chao-Xing Liu, Hai-Jun Zhang, Chi-Yung Yam, Xiao-Liang Qi, Thomas Frauenheim, and Shou-Cheng Zhang. Theoretical prediction of topological insulators in thallium-based III-V-VI 2 ternary chalcogenides. *EPL (Europhysics Letters)*, 90(3):37002, 2010.

[21] Y. L. Chen, Z. K. Liu, J. G. Analytis, J.-H. Chu, H. J. Zhang, B. H. Yan, S.-K. Mo, R. G. Moore, D. H. Lu, I. R. Fisher, S. C. Zhang, Z. Hussain, and Z.-X. Shen. Single Dirac cone topological surface state and unusual thermoelectric property of compounds from a new topological insulator family. *Phys. Rev. Lett.*, 105:266401, Dec 2010.

[22] Takafumi Sato, Kouji Segawa, Hua Guo, Katsuaki Sugawara, Seigo Souma, Takashi Takahashi, and Yoichi Ando. Direct evidence for the

Dirac-cone topological surface states in the ternary chalcogenide $TlBiSe_2$. *Phys. Rev. Lett.*, 105:136802, Sep 2010.

[23] Stanislav Chadov, Xiaoliang Qi, Jürgen Kübler, Gerhard H. Fecher, Claudia Felser, and Shou Cheng Zhang. Tunable multifunctional topological insulators in ternary Heusler compounds. *Nat Mater*, 9(7):541–545, 07 2010.

[24] Hsin Lin, L. Andrew Wray, Yuqi Xia, Suyang Xu, Shuang Jia, Robert J. Cava, Arun Bansil, and M. Zahid Hasan. Half-Heusler ternary compounds as new multifunctional experimental platforms for topological quantum phenomena. *Nat Mater*, 9(7):546–549, 07 2010.

[25] Atsuo Shitade, Hosho Katsura, Jan Kuneš, Xiao-Liang Qi, Shou-Cheng Zhang, and Naoto Nagaosa. Quantum spin hall effect in a transition metal oxide Na_2IrO_3. *Phys. Rev. Lett.*, 102:256403, Jun 2009.

[26] H.-M. Guo and M. Franz. Theory of quasiparticle interference on the surface of a strong topological insulator. *Phys. Rev. B*, 81:041102, Jan 2010.

[27] Xiangang Wan, Ari M. Turner, Ashvin Vishwanath, and Sergey Y. Savrasov. Topological semimetal and fermi-arc surface states in the electronic structure of pyrochlore iridates. *Phys. Rev. B*, 83:205101, May 2011.

[28] Liang Fu. Topological crystalline insulators. *Phys. Rev. Lett.*, 106:106802, Mar 2011.

[29] Timothy H. Hsieh, Hsin Lin, Junwei Liu, Wenhui Duan, Arun Bansil, and Liang Fu. Topological crystalline insulators in the SnTe material class. *Nat Commun*, 3:982, 2012.

[30] Y. Tanaka, Zhi Ren, T. Sato, K. Nakayama, S. Souma, T. Takahashi, Kouji Segawa, and Yoichi Ando. Experimental realization of a topological crystalline insulator in SnTe. *Nat Phys*, 8(11):800–803, 2012. 10.1038/nphys2442.

[31] P. Dziawa, B. J. Kowalski, K. Dybko, R. Buczko, A. Szczerbakow, M. Szot, E. Łusakowska, T. Balasubramanian, B. M. Wojek, M. H. Berntsen, O. Tjernberg, and T. Story. Topological crystalline insulator states in $Pb_{1x}Sn_xSe$. *Nat Mater*, 11(12):1023–1027, 12 2012.

[32] Su-Yang Xu, Chang Liu, N. Alidoust, M. Neupane, D. Qian, I. Belopolski, J. D. Denlinger, Y. J. Wang, H. Lin, L. A. Wray, G. Landolt, B. Slomski, J. H. Dil, A. Marcinkova, E. Morosan, Q. Gibson, R. Sankar, F. C. Chou, R. J. Cava, A. Bansil, and M. Z. Hasan. Observation of a topological crystalline insulator phase and topological phase transition in $Pb_{1-x}Sn_xTe$. *Nat Commun*, 3:1192, 11 2012.

[33] Chenhui Yan, Junwei Liu, Yunyi Zang, Jianfeng Wang, Zhenyu Wang, Peng Wang, Zhi-Dong Zhang, Lili Wang, Xucun Ma, Shuaihua Ji, Ke He, Liang Fu, Wenhui Duan, Qi-Kun Xue, and Xi Chen. Experimental observation of Dirac-like surface states and topological phase transition in $Pb_{1-x}Sn_xTe$ (111) films. *Phys. Rev. Lett.*, 112:186801, May 2014.

[34] Yan Sun, Zhicheng Zhong, Tomonori Shirakawa, Cesare Franchini, Dianzhong Li, Yiyi Li, Seiji Yunoki, and Xing-Qiu Chen. Rocksalt

SnS and SnSe: Native topological crystalline insulators. *Phys. Rev. B*, 88:235122, Dec 2013.

[35] Paolo Barone, Tomá š Rauch, Domenico Di Sante, Jürgen Henk, Ingrid Mertig, and Silvia Picozzi. Pressure-induced topological phase transitions in rocksalt chalcogenides. *Phys. Rev. B*, 88:045207, Jul 2013.

[36] Timothy H. Hsieh, Junwei Liu, and Liang Fu. Topological crystalline insulators and Dirac octets in antiperovskites. *Phys. Rev. B*, 90:081112, Aug 2014.

[37] F. Munoz, M. G. Vergniory, T. Rauch, J. Henk, E. V. Chulkov, I. Mertig, S. Botti, M. A. L. Marques, and A. H. Romero. Topological crystalline insulator in a new Bi semiconducting phase. *Scientific Reports*, 6:21790, 02 2016.

[38] Andreas P. Schnyder, Shinsei Ryu, Akira Furusaki, and Andreas W. W. Ludwig. Classification of topological insulators and superconductors in three spatial dimensions. *Phys. Rev. B*, 78:195125, Nov 2008.

[39] Xiao-Liang Qi, Taylor L. Hughes, S. Raghu, and Shou-Cheng Zhang. Time-reversal-invariant topological superconductors and superfluids in two and three dimensions. *Phys. Rev. Lett.*, 102:187001, May 2009.

[40] Xiao-Liang Qi, Taylor L. Hughes, and Shou-Cheng Zhang. Topological invariants for the fermi surface of a time-reversal-invariant superconductor. *Phys. Rev. B*, 81:134508, Apr 2010.

[41] Jacob Linder, Yukio Tanaka, Takehito Yokoyama, Asle Sudbø, and Naoto Nagaosa. Unconventional superconductivity on a topological insulator. *Phys. Rev. Lett.*, 104:067001, Feb 2010.

[42] N. P. Butch, P. Syers, K. Kirshenbaum, A. P. Hope, and J. Paglione. Superconductivity in the topological semimetal YPtBi. *Phys. Rev. B*, 84:220504, Dec 2011.

[43] G. Goll, M. Marz, A. Hamann, T. Tomanic, K. Grube, T. Yoshino, and T. Takabatake. Thermodynamic and transport properties of the noncentrosymmetric superconductor LaBiPt. *Physica B: Condensed Matter*, 403(5-9):1065 – 1067, 2008. Proceedings of the International Conference on Strongly Correlated Electron Systems.

[44] F. F. Tafti, Takenori Fujii, A. Juneau-Fecteau, S. René de Cotret, N. Doiron-Leyraud, Atsushi Asamitsu, and Louis Taillefer. Superconductivity in the noncentrosymmetric half-heusler compound LuPtBi: A candidate for topological superconductivity. *Phys. Rev. B*, 87:184504, May 2013.

[45] Liang Fu and Erez Berg. Odd-parity topological superconductors: Theory and application to $Cu_xBi_2Se_3$. *Phys. Rev. Lett.*, 105:097001, Aug 2010.

[46] Y. S. Hor, A. J. Williams, J. G. Checkelsky, P. Roushan, J. Seo, Q. Xu, H. W. Zandbergen, A. Yazdani, N. P. Ong, and R. J. Cava. Superconductivity in $Cu_xBi_2Se_3$ and its implications for pairing in the undoped topological insulator. *Phys. Rev. Lett.*, 104:057001, Feb 2010.

[47] L. Andrew Wray, Su-Yang Xu, Yuqi Xia, Yew San Hor, Dong Qian, Alexei V. Fedorov, Hsin Lin, Arun Bansil, Robert J. Cava, and M. Za-

hid Hasan. Observation of topological order in a superconducting doped topological insulator. *Nat Phys*, 6(11):855–859, 11 2010.

[48] M. Kriener, Kouji Segawa, Zhi Ren, Satoshi Sasaki, and Yoichi Ando. Bulk superconducting phase with a full energy gap in the doped topological insulator $Cu_xBi_2Se_3$. *Phys. Rev. Lett.*, 106:127004, Mar 2011.

[49] Satoshi Sasaki, M. Kriener, Kouji Segawa, Keiji Yada, Yukio Tanaka, Masatoshi Sato, and Yoichi Ando. Topological superconductivity in $Cu_xBi_2Se_3$. *Phys. Rev. Lett.*, 107:217001, Nov 2011.

[50] J. A. Schneeloch, R. D. Zhong, Z. J. Xu, G. D. Gu, and J. M. Tranquada. Dependence of superconductivity in $Cu_xBi_2Se_3$ on quenching conditions. *Phys. Rev. B*, 91:144506, Apr 2015.

[51] T. Sato, Y. Tanaka, K. Nakayama, S. Souma, T. Takahashi, S. Sasaki, Z. Ren, A. A. Taskin, Kouji Segawa, and Yoichi Ando. Fermiology of the strongly spin-orbit coupled superconductor $Sn_{1-x}In_xTe$: Implications for topological superconductivity. *Phys. Rev. Lett.*, 110:206804, May 2013.

[52] GS Bushmarina, IA Drabkin, DV Mashovets, RV Parfeniev, DV Shamshur, and MA Shachov. Superconducting properties of the SnTe-PbTe system doped with indium. *Physica B: Condensed Matter*, 169(1-4):687–688, 1991.

[53] R.V. Parfeniev, D.V. Shamshur, M.A. Shakhov, and Zb. Chrapkiewicz. Superconductivity and magnetism in in-doped lead-tin tellurides. *Journal of Alloys and Compounds*, 219(1):313 – 315, 1995.

[54] A. S. Erickson, J.-H. Chu, M. F. Toney, T. H. Geballe, and I. R. Fisher. Enhanced superconducting pairing interaction in indium-doped tin telluride. *Phys. Rev. B*, 79:024520, Jan 2009.

[55] G. Balakrishnan, L. Bawden, S. Cavendish, and M. R. Lees. Superconducting properties of the in-substituted topological crystalline insulator SnTe. *Phys. Rev. B*, 87:140507, Apr 2013.

[56] Mario Novak, Satoshi Sasaki, Markus Kriener, Kouji Segawa, and Yoichi Ando. Unusual nature of fully gapped superconductivity in in-doped SnTe. *Phys. Rev. B*, 88:140502, Oct 2013.

[57] Brian Skinner, Tianran Chen, and BI Shklovskii. Why is the bulk resistivity of topological insulators so small? *Physical review letters*, 109(17):176801, 2012.

[58] N. P. Butch, K. Kirshenbaum, P. Syers, A. B. Sushkov, G. S. Jenkins, H. D. Drew, and J. Paglione. Strong surface scattering in ultrahigh-mobility Bi_2Se_3 topological insulator crystals. *Phys. Rev. B*, 81:241301, Jun 2010.

[59] Shuang Jia, Huiwen Ji, E. Climent-Pascual, M. K. Fuccillo, M. E. Charles, Jun Xiong, N. P. Ong, and R. J. Cava. Low-carrier-concentration crystals of the topological insulator $Bi_2Te_2Se_3$. *Phys. Rev. B*, 84:235206, Dec 2011.

[60] Hailin Peng, Keji Lai, Desheng Kong, Stefan Meister, Yulin Chen, Xiao-Liang Qi, Shou-Cheng Zhang, Zhi-Xun Shen, and Yi Cui. Aharonov-bohm interference in topological insulator nanoribbons. *Nature materials*, 9(3):225–229, 2010.

[61] Y. S. Hor, A. Richardella, P. Roushan, Y. Xia, J. G. Checkelsky, A. Yazdani, M. Z. Hasan, N. P. Ong, and R. J. Cava. p-type Bi_2Se_3 for topological insulator and low-temperature thermoelectric applications. *Phys. Rev. B*, 79:195208, May 2009.

[62] James G Analytis, Ross D McDonald, Scott C Riggs, Jiun-Haw Chu, GS Boebinger, and Ian R Fisher. Two-dimensional surface state in the quantum limit of a topological insulator. *Nature Physics*, 6(12):960–964, 2010.

[63] J. G. Checkelsky, Y. S. Hor, R. J. Cava, and N. P. Ong. Bulk band gap and surface state conduction observed in voltage-tuned crystals of the topological insulator Bi_2Se_3. *Phys. Rev. Lett.*, 106:196801, May 2011.

[64] Satoshi Sasaki, Zhi Ren, A. A. Taskin, Kouji Segawa, Liang Fu, and Yoichi Ando. Odd-parity pairing and topological superconductivity in a strongly spin-orbit coupled semiconductor. *Phys. Rev. Lett.*, 109:217004, Nov 2012.

[65] J. J. de Rooi, N. M. van der Pers, R. W. A. Hendrikx, R. Delhez, A. J. Bottger, and P. H. C. Eilers.

[66] A. J. Darnell and W. F. Libby. Artificial metals: InSb, the Sn Alloys with InSb, and Metallic InTe. *Phys. Rev.*, 135:A1453–A1459, Aug 1964.

[67] R. V. Parfen'ev, D. V. Shamshur, and S. A. Nemov. Dependence of the superconducting transition parameters on the solid-solution composition and Te excess in $Sn_{1-z}Pb_zTe$:In. *Physics of the Solid State*, 41(12):1956–1958, 1999.

[68] D. V. Shamshur, R. V. Parfen'ev, A. V. Chernyaev, and S. A. Nemov. Low-temperature electrical conductivity and the superconductor-insulator transition induced by indium impurity states in $(Pb_{0.5}Sn_{0.5})_{1-y}In_yTe$ solid solutions. *Physics of the Solid State*, 52(9):1815–1819, 2010.

[69] G. O. Andrianov, S. A. Nemov, R. V. Parfen'ev, D. V. Shamshur, and A. V. Chernyaev. Effect of hydrostatic compression on the indium-impurity-induced superconducting transition in $Pb_{0.3}Sn_{0.7}Te$. *Physics of the Solid State*, 52(9):1810–1814, 2010.

[70] Neel Haldolaarachchige, Quinn Gibson, Weiwei Xie, Morten Bormann Nielsen, Satya Kushwaha, and R. J. Cava. Anomalous composition dependence of the superconductivity in In-doped SnTe. *Phys. Rev. B*, 93:024520, Jan 2016.

[71] Guan Du, Zengyi Du, Delong Fang, Huan Yang, R. D. Zhong, J. Schneeloch, G. D. Gu, and Hai-Hu Wen. Fully gapped superconductivity in In-doped topological crystalline insulator $Pb_{0.5}Sn_{0.5}Te$. *Phys. Rev. B*, 92:020512, Jul 2015.

[72] N. R. Werthamer, E. Helfand, and P. C. Hohenberg. Temperature and purity dependence of the superconducting critical field, H_{c2}. III. electron spin and spin-orbit effects. *Phys. Rev.*, 147:295–302, Jul 1966.

[73] J. R. Dixon and R. F. Bis. Band inversion and the electrical properties of $Pb_xSn_{1-x}Te$. *Phys. Rev.*, 176:942–949, Dec 1968.

[74] V. I. Kozub, R. V. Parfen'ev, D. V. Shamshur, D. V. Shakura, A. V. Chernyaev, and S. A. Nemov. Superconductor-insulator transition in $(Pb_zSn_{1-z})_{0.84}In_{0.16}Te$. *JETP Letters*, 84(1):35–40, 2006.

[75] D. V. Shamshur, S. A. Nemov, R. V. Parfen'ev, M. S. Kononchuk, and V. I. Nizhankovskii. Low-temperature conductivity and the Hall effect in $(Pb_zSn_{1-z})_{0.84}In_{0.16}Te$ semiconducting solid solutions. *Physics of the Solid State*, 50(11):2028, 2008.

[76] B. A. Akimov, N. B. Brandt, L. I. Ryabova, V. V. Sokovishin, and S. M. Chudinov. Band edge motion in quantizing magnetic field and nonequilibrium states in $Pb_{1-x}Sn_xTe$ alloys doped with In. *Journal of Low Temperature Physics*, 51(1):9–32, 1983.

[77] Yu. I. Ravich and S. A. Nemov. Hopping conduction via strongly localized impurity states of indium in PbTe and its solid solutions. *Semiconductors*, 36(1):1–20, 2002.

[78] A. A. Taskin, Zhi Ren, Satoshi Sasaki, Kouji Segawa, and Yoichi Ando. Observation of Dirac holes and electrons in a topological insulator. *Phys. Rev. Lett.*, 107:016801, Jun 2011.

[79] D. J. Kim, J. Xia, and Z. Fisk. Topological surface state in the Kondo insulator samarium hexaboride. *Nat Mater*, 13(5):466–470, May 2014.

[80] Paul Syers, Dohun Kim, Michael S. Fuhrer, and Johnpierre Paglione. Tuning bulk and surface conduction in the proposed topological Kondo insulator SmB_6. *Phys. Rev. Lett.*, 114:096601, Mar 2015.

[81] Namrata Bansal, Yong Seung Kim, Matthew Brahlek, Eliav Edrey, and Seongshik Oh. Thickness-independent transport channels in topological insulator Bi_2Se_3 thin films. *Phys. Rev. Lett.*, 109:116804, Sep 2012.

[82] Maksym Serbyn and Liang Fu. Symmetry breaking and landau quantization in topological crystalline insulators. *Phys. Rev. B*, 90:035402, Jul 2014.

[83] Shinobu Hikami, Anatoly I Larkin, and Yosuke Nagaoka. Spin-orbit interaction and magnetoresistance in the two dimensional random system. *Progress of Theoretical Physics*, 63(2):707–710, 1980.

[84] Junwei Liu, Wenhui Duan, and Liang Fu. Two types of surface states in topological crystalline insulators. *Phys. Rev. B*, 88:241303, Dec 2013.

[85] Badih A Assaf, Ferhat Katmis, Peng Wei, Biswarup Satpati, Zhan Zhang, Steven P Bennett, Vincent G Harris, Jagadeesh S Moodera, and Don Heiman. Quantum coherent transport in SnTe topological crystalline insulator thin films. *Applied Physics Letters*, 105(10):102108, 2014.

[86] V. I. Kaidanov and Yurii Isakovich Ravich. Deep and resonance states in AIV BVI semiconductors. *Sov. Phys. Usp.*, 28(1):31–53, 1985.

[87] O. A. Pankratov, S. V. Pakhomov, and B. A. Volkov. Supersymmetry in heterojunctions: Band-inverting contact on the basis of $Pb_{1-x}Sn_xTe$ and $Hg_{1-x}Cd_xTe$. *Solid state communications*, 61(2):93–96, 1987.

[88] J. O. Dimmock, I. Melngailis, and A. J. Strauss. Band structure and laser action in $Pb_{1-x}Sn_xTe$. *Phys. Rev. Lett.*, 16:1193–1196, Jun 1966.

[89] Xing Gao and Murray S. Daw. Investigation of band inversion in (pb,sn)te alloys using ab initio calculations. *Phys. Rev. B*, 77:033103, Jan 2008.

[90] Y. Tanaka, T. Sato, K. Nakayama, S. Souma, T. Takahashi, Zhi Ren, M. Novak, Kouji Segawa, and Yoichi Ando. Tunability of the k-space location of the Dirac cones in the topological crystalline insulator $Pb_{1-x}Sn_xTe$. *Phys. Rev. B*, 87:155105, Apr 2013.

[91] Joseph P Heremans, Bartlomiej Wiendlocha, and Audrey M Chamoire. Resonant levels in bulk thermoelectric semiconductors. *Energy & Environmental Science*, 5(2):5510–5530, 2012.

[92] Qian Zhang, Bolin Liao, Yucheng Lan, Kevin Lukas, Weishu Liu, Keivan Esfarjani, Cyril Opeil, David Broido, Gang Chen, and Zhifeng Ren. High thermoelectric performance by resonant dopant indium in nanostructured SnTe. *Proceedings of the National Academy of Sciences*, 110(33):13261–13266, 2013.

[93] Satoki Maeda, Shota Katsube, and Guo-qing Zheng. Quasi-localized impurity state in doped topological crystalline insulator $Sn_{0.9}In_{0.1}Te$ Probed by ^{125}Te-NMR. *Journal of the Physical Society of Japan*, 86(2):024702, 2016.

[94] SK Kushwaha, I Pletikosić, T Liang, A Gyenis, SH Lapidus, Yao Tian, He Zhao, KS Burch, Jingjing Lin, Wudi Wang, et al. Sn-doped $Bi_{1.1}Sb_{0.9}Te_2S$ bulk crystal topological insulator with excellent properties. *Nature communications*, 7, 2016.

[95] T. Kirzhner, E. Lahoud, K. B. Chaska, Z. Salman, and A. Kanigel. Point-contact spectroscopy of $Cu_{0.2}Bi_2Se_3$ single crystals. *Phys. Rev. B*, 86:064517, Aug 2012.

[96] Niv Levy, Tong Zhang, Jeonghoon Ha, Fred Sharifi, A. Alec Talin, Young Kuk, and Joseph A. Stroscio. Experimental evidence for s-wave pairing symmetry in superconducting $\mathrm{Cu}_x\mathrm{Bi}_2\mathrm{Se}_3$ single crystals using a scanning tunneling microscope. *Phys. Rev. Lett.*, 110:117001, Mar 2013.

[97] L. P. He, Z. Zhang, J. Pan, X. C. Hong, S. Y. Zhou, and S. Y. Li. Full superconducting gap in the doped topological crystalline insulator $\mathrm{Sn}_{0.6}\mathrm{In}_{0.4}\mathrm{Te}$. *Phys. Rev. B*, 88:014523, Jul 2013.

[98] M. Saghir, J. A. T. Barker, G. Balakrishnan, A. D. Hillier, and M. R. Lees. Superconducting properties of $\mathrm{Sn}_{1-x}\mathrm{In}_x\mathrm{Te}$ $(x = 0.38 - -0.45)$ studied using muon-spin spectroscopy. *Phys. Rev. B*, 90:064508, Aug 2014.

[99] K Matano, M Kriener, K Segawa, Y Ando, and Guo-qing Zheng. Spin-rotation symmetry breaking in the superconducting state of $\mathrm{Cu}_x\mathrm{Bi}_2\mathrm{Se}_3$. *Nature Physics*, 12(9):852–854, 2016.

[100] Zhijun Xu, J. A. Schneeloch, R. D. Zhong, J. A. Rodriguez-Rivera, L. W. Harriger, R. J. Birgeneau, G. D. Gu, J. M. Tranquada, and Guangyong Xu. Low-energy phonons and superconductivity in $\mathrm{Sn}_{0.8}\mathrm{In}_{0.2}\mathrm{Te}$. *Phys. Rev. B*, 91:054522, Feb 2015.

[101] Gen Shirane, Stephen M Shapiro, and John M Tranquada. *Neutron scattering with a triple-axis spectrometer: basic techniques*. Cambridge University Press, 2002.

[102] K. E. Arpino, D. C. Wallace, Y. F. Nie, T. Birol, P. D. C. King, S. Chatterjee, M. Uchida, S. M. Koohpayeh, J.-J. Wen, K. Page, C. J. Fennie, K. M. Shen, and T. M. McQueen. Evidence for topologically protected surface states and a superconducting phase in

$[Tl_4]Tl_{1-x}Sn_xTe_3$ using photoemission, specific heat, and magnetization measurements, and density functional theory. *Phys. Rev. Lett.*, 112:017002, Jan 2014.

[103] KE Arpino, BD Wasser, and TM McQueen. Superconducting dome and crossover to an insulating state in $[Tl_4]Tl_{1-x}Sn_xTe_3$. *APL materials*, 3(4):041507, 2015.

[104] Liang Fu and C. L. Kane. Superconducting proximity effect and majorana fermions at the surface of a topological insulator. *Phys. Rev. Lett.*, 100:096407, Mar 2008.

[105] Mei-Xiao Wang, Canhua Liu, Jin-Peng Xu, Fang Yang, Lin Miao, Meng-Yu Yao, CL Gao, Chenyi Shen, Xucun Ma, X Chen, et al. The coexistence of superconductivity and topological order in the Bi_2Se_3 thin films. *Science*, 336(6077):52–55, 2012.

[106] Eryin Wang, Hao Ding, Alexei V Fedorov, Wei Yao, Zhi Li, Yan-Feng Lv, Kun Zhao, Li-Guo Zhang, Zhijun Xu, John Schneeloch, et al. Fully gapped topological surface states in Bi_2Se_3 films induced by a d-wave high-temperature superconductor. *Nature physics*, 9(10):621–625, 2013.

[107] Jin-Peng Xu, Canhua Liu, Mei-Xiao Wang, Jianfeng Ge, Zhi-Long Liu, Xiaojun Yang, Yan Chen, Ying Liu, Zhu-An Xu, Chun-Lei Gao, et al. Artificial topological superconductor by the proximity effect. *Physical Review Letters*, 112(21):217001, 2014.

[108] Zheng-Zao Li, Fu-Chun Zhang, and Qiang-Hua Wang. Majorana modes in a topological insulator/s-wave superconductor heterostructure. *Scientific reports*, 4, 2014.

[109] Jin-Peng Xu, Mei-Xiao Wang, Zhi Long Liu, Jian-Feng Ge, Xiaojun Yang, Canhua Liu, Zhu An Xu, Dandan Guan, Chun Lei Gao, Dong Qian, et al. Experimental detection of a Majorana mode in the core of a magnetic vortex inside a topological insulator-superconductor Bi_2Se_3/$NbSe_2$ heterostructure. *Physical review letters*, 114(1):017001, 2015.

Chapter 4

Explorations of Dynamic Correlations in Materials Related to High Temperature Superconductors

In this Chapter, I present our studies on the dynamic structural correlations in $La_{1.875}Ba_{0.125}CuO_{4+\delta}$, as well as the dynamic electronic correlations in $La_{1.75}Sr_{0.25}NiO_{4+\delta}$. This Chapter is largely reprinted from my published articles, Ref. [1, 2]; copyright is held by the American Physical Society.

4.1 High temperature cuprate superconductors

High T_c superconductivity in copper oxides (cuprates) is one of the most intriguing phenomena in the strongly correlated electron systems. It has attracted great attention since its discover in 1986 [3], because T_c can exceed the boiling temperature of liquid nitrogen, and is much higher than the predicted upper limit of T_c from BCS theory for conventional superconductivity.

The typical crystal structure of a cuprate superconductor is a multi-layered perovskite structure, shown in Figure 4.1*(a)*. The crucial structural subunit is the Cu-O_2 plane, which extends in the a-b direction. Electronic couplings in plane are strong, while along the interplane (c-direction) the couplings are very weak. In a certain CuO_2 plane, squares of O^{2-} ions with a Cu^{2+} ion at the center of each square from checkerboard lattices (Figure 4.1*(b)*). The layers of CuO_2 are believed to be the key structure in high T_c superconductivity. Before the discovery of iron-based superconductor in 2008, most of ceramic high T_c superconductors are cuprates. In the La_2CuO_4 family of materials, hole doping is achieved by substituting Sr or Ba ions for some of the La ions indicated, or by adding interstitial oxygen. In other families of high T_c materials such as $YBa_2Cu_3O_{6+\delta}$, the crystal structure and mechanism of doping are slightly different, but all materials share the feature of CuO_2 planes weakly coupled in the transverse

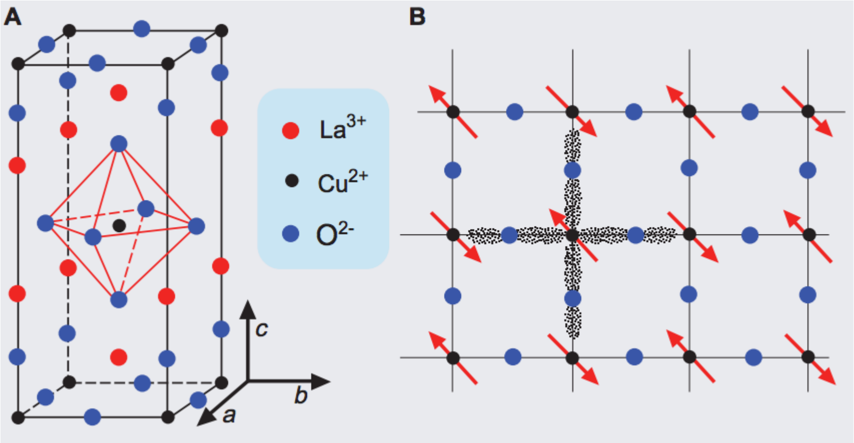

Figure 4.1: (a) Crystal structure of La_2CuO_4, the parent compound of the hole (Ba, Sr) doped cuprate superconductors. (b) Schematic of copper-oxide plane. The red arrows represent a possible alignment of spins in the antiferromagnetic ground state of La_2CuO_4. Figure from Ref. [4].

direction [4]. It has been proposed that the combination of proximity to a Mott insulating phase and low dimensionality would cause the doped materials to exhibit fundamentally new behavior, not explicable in terms of conventional metal physics [4].

On doping holes, the antiferromagnetic Mott insulator phase of the parent compounds disappers and superconductivity emerges. T_c follows a dome-like shape as a function of doping, with a maximum T_c around 16% holes per CuO_2 plaquette [5]. A similar phase diagram is seen on doping electrons, albeit with a more robust antiferromagnetic phase and a lower T_c. On the hole-doped side, there exists an enigmatic state above T_c called the pseudogap, where the electron density of states within certain momentum region is suppressed [6]. A schematic phase diagram of both hole- and electron-doped cuprates are shown in Figure 4.2. The cuprate superconductors not only manifest superconducting transition temperatures inconceivable decades ago, but also exhibit many other properties

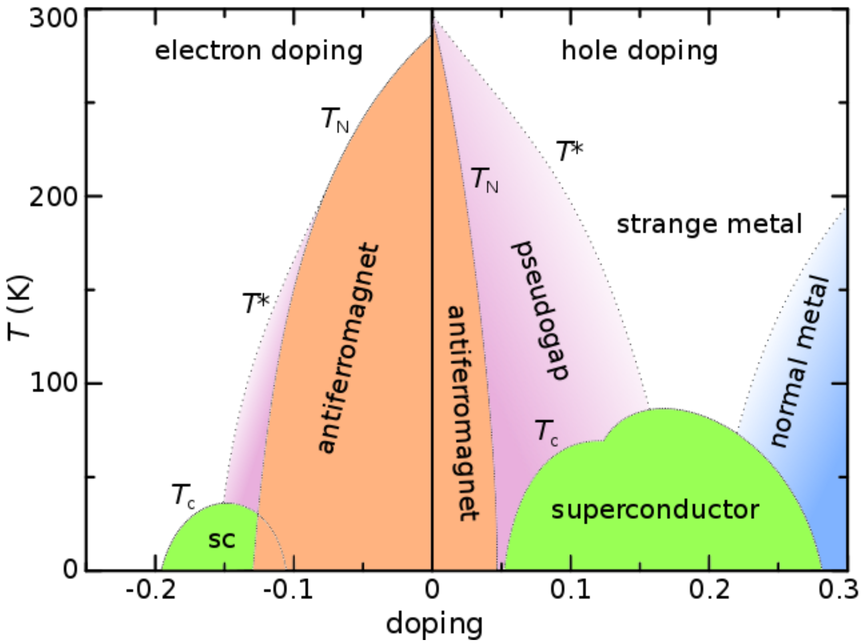

Figure 4.2: Schematic doping phase diagram of high T_c cuprate superconductors.

apparently incompatible with the conventional superconductor physics, which stimulates the development of new experimental techniques and theoretical concepts.

An increasingly well-documented feature of high temperature superconductors is a tendency towards a variety of orders in addition to superconductivity. Neutron scattering studies in the mid-1990s led to the experimental discovery of electronic 'stripes' in the $La_{2-x}Sr_xCuO_4$ (LSCO) [7]. A theoretical perspective was based on the observation that doping an insulating antiferromagnet produces a tendency to phase sepa-

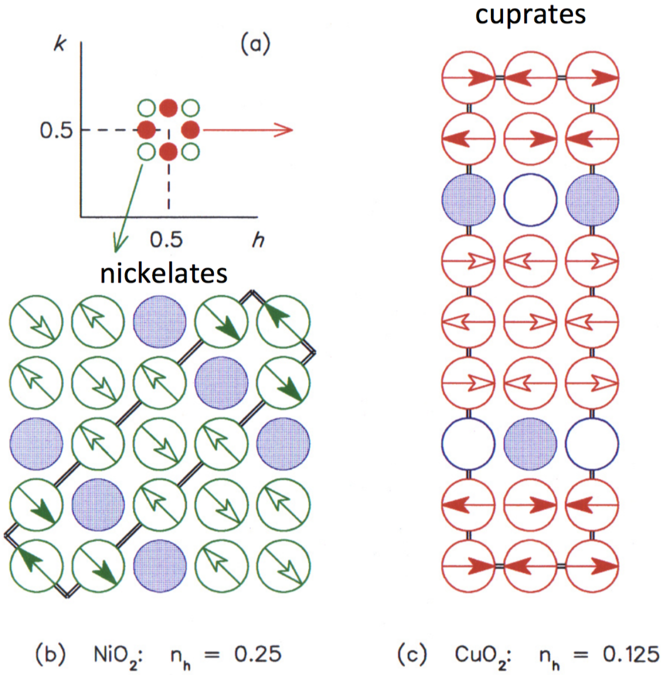

Figure 4.3: (a) Relative position of the incommensurate stripe patterns in LSNO and LBCO, plotted in the momentum space. Diagram of the spin and charge stripe pattern with in a NiO_2 or CuO_2 plane observed in hole-doped La_2NiO_4 (b) and La_2CuO_4 (c).

ration that is frustrated by the long-range Coulomb interaction, and resulting on conducting stripe-like textures [8]. The stripe order, characterized by incommensurate antiferromagnetic order and charge segregation, was initially found in the underdoped versions of LSCO, where a low-temperature-tetragonal (LTT) lattice deformation apparently pins the stripes [7]. In cuprates, static stripe order and uniform superconductivity are two competing parameters: in $La_{1.6-x}Nd_{0.4}Sr_xCuO_4$ superconducting transition temperature T_c decreases as the staggered magnetization increases[9]; bulk superconductivity is anomalously suppressed in materials such as $La_{2-x}Ba_xCuO_4$ $x = \frac{1}{8}$ that exhibit static stripe order [10–12]; the stability of both orders in high T_c cuprates is enhanced when the superconductivity is suppressed by magnetic field or impurity substitution[13]. On the other hand, fluctuating stripes can coexist with superconductivity and could play a role in the superconducting pairing mechanism[14, 15]. Unfortunately, even though substantial evidence for static stripes have been detected by diffraction techniques in cuprate materials[13, 16, 17], stripe dynamics and their role in high T_c superconductivity have long been controversial.

Since about two decades ago the static charge and spin stripes were first discovered in the same sample $La_4NiO_{4.125}$ by neutron diffraction[18, 19], there have also been comprehensive studies for static spin and charge modulations in related nickel system, $La_{2-x}Sr_xNiO_{4+\delta}$[20–27]. Unlike most cuprates in which charges are observed to segregate in stripes running along the Cu-O bonds (horizontal or vertical stripes), in the nickelates stripes tend to run along the diagnonal direction with respect to the Ni-O bonds (diagonal stripes). Diagonal magnetic stripes also have been observed in slightly-doped $La_{2-x}Sr_xCuO_4$[28], which is an exceptional case in cuprates. Progress has been made on exploring the dynamic magnetic correlations in nickelates, and the survival of dynamic incommensurate spin stripes above the ordering temperature implies that the dynamic charge stripe correlations should play an underlying role[29, 30]. In past years great effort has been made on the phonon anomalies at the charge stripe ordering vectors[31–33], trying to understand underlying correlations of the dynamic charge fluctuations, but a direct characterization of the dynamic charge stripes has been lacking.

In fact, directly probing the fluctuating charge stripe order in cuprates is complicated by their metallic properties, and it thus seems most interesting to investigate stripes in related compounds, such as non-superconducting, insulating nickelates with similar stripe-phase structure. Compared to cuprates, moderately doped $La_{2-x}Sr_xNiO_4$ (LSNO) has reduced conductivity and charge mobility since the spin value S = 1. Besides, in nickelates the stronger stripe ordering at higher hole density, and the coupling to lattice is stronger[34]. Thus lattice fluctuations due to the dynamic charges should be easier to observe. Diffraction measurements have shown that the corresponding lattice modulation is much larger in nickelates than in cuprates[35, 36]. All these reasons make LSNO a model system to study the charge fluctuations.

In this chapter I will focus on the dynamic correlations at high temperature, where the static correlations are in the disordered state. To illustrate the characteristics of the dynamic correlations, two selected examples will be discussed. The first example is from the structural view, to study the LTT-like tilt fluctuations above the LTO-LTT transitions in $La_{2-x}Ba_xCuO_{4+\delta}$ with $x = 1/8$. The second one is from the electronic view, to look at the dynamic charge stripes above the stripe ordering temperature in the $La_{2-x}Sr_xNiO_{4+\delta}$ with $x = 1/4$. Although both $La_{2-x}Ba_xCuO_{4+\delta}$ and $La_{2-x}Sr_xNiO_{4+\delta}$ have layered structures as well as the stripe phase, there is one big difference on the stripe direction. Figure 4.3 is plotted in the tetragonal one copper unit cell. In cuprates, the stripes run in horizontal or vertical direction, while in nickelates, the stripes run in diagonal direction. There is no affirmative explanation about this difference, but it has been found that the diagonal stripes are preferred in a more localized insulating material, such as nickelates and even some slightly doped cuprates.

4.2 Structural view: LTT-like tilt fluctuations above the LTO-LTT transition in $La_{2-x}Ba_xCuO_{4+\delta}$, $x = 1/8$

4.2.1 Structural transitions in the LBCO, 1/8

Figure 4.4*(a)* shows the crystal structure of the Ba doped La-214 cuprates at room temperature. At high temperature, the CuO_6 octahedra are untilted so the top and bottom CuO_2 planes are flat. This is called the **high-temperature-tetragonal (HTT)** phase. Upon cooling, the HTT phase undergoes two phase transitions: First, the flat octahedra tilt about the <110> direction, namely, along the Cu-Cu bonds. Due to the superlattice tilting the overall crystal structure becomes distorted, and changes to an orthorhombic structure. This is called the **low-temperature-orthorhombic (LTO)** phase. As the temperature continues to decrease, it goes through the second phase transition and the octahedra start to tilt along either <100> or <010> directions, or in another word, the Cu-O bonds. Since the overall crystal structure changes back to the tetragonal again, we call it the **low-temperature-tetragonal (LTT)** phase. The tilt direction changes

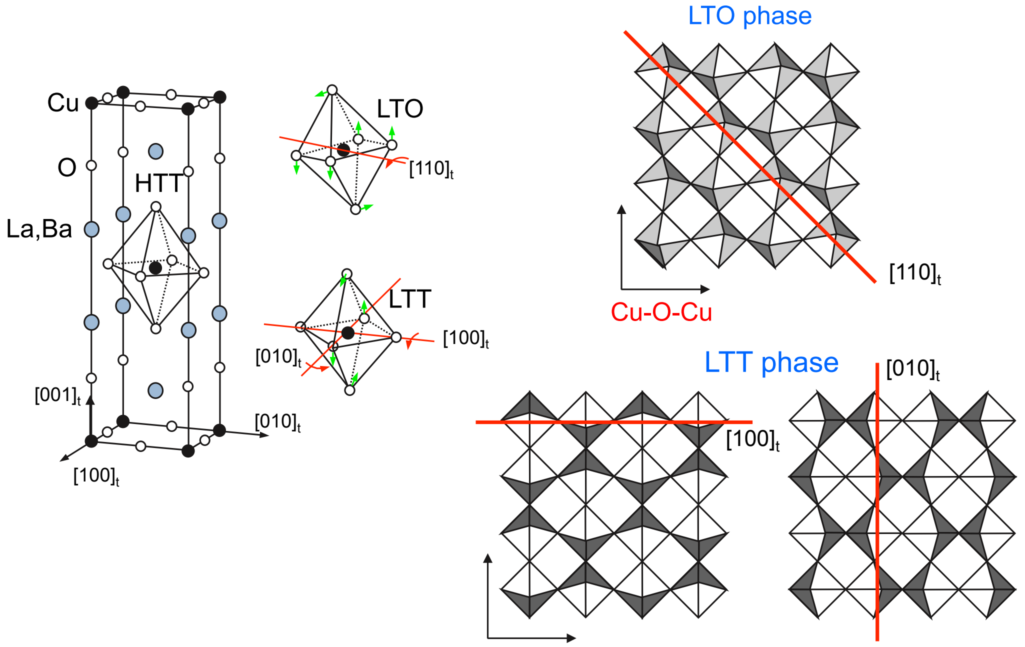

Figure 4.4: (a) A schematic illustrating the tilting patterns of the CuO_6 octahedra in the HTT, LTO, and LTT phase in LBCO. (b) The deformed CuO_2 planes in the LTO and LTT phase at low temperature. Figure created on the basis of Fig. 2 in Ref. [37].

alternatively between these two directions in adjacent planes. As shown in Figure 4.4*(b)*, in both of the two low temperature phases, the CuO_2 planes deform and become bent or twisted out of shape [37]. The tilted LTT phase is believed to be the reason for the stripe pinning [38].

There are many other phase transitions that take place in the doped LBCO, and the structural transitions and the electronic properties are closely related, as shown in Figure 4.5. By hole doping, the long-range AF order is destroyed, but magnetic correlations persist in the superconducting region, which is actually induced by doping. At very low temperature, stripes become static, and there is a superconductivity anomaly in the 1/8 doped LBCO, where the stripe ordering becomes most pronounced, while the

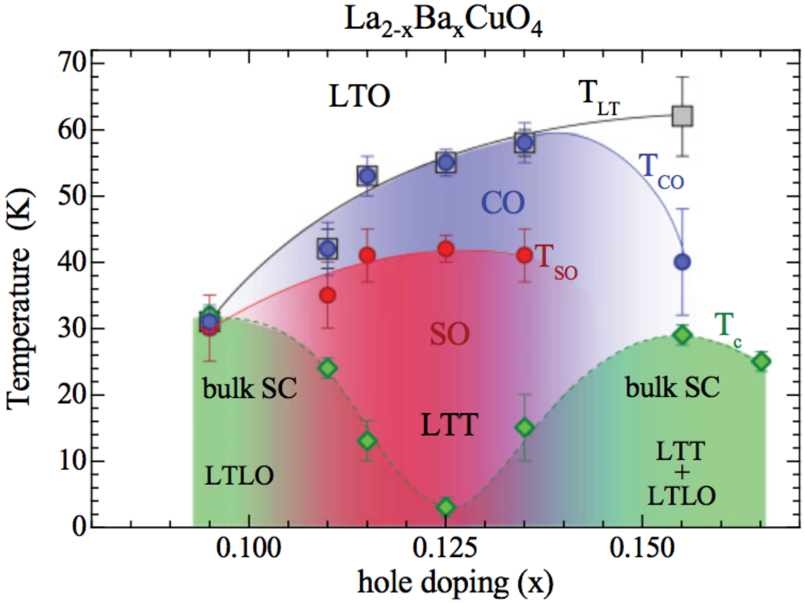

Figure 4.5: Temperature *v.s.* hole-doping phase diagram of $La_{2-x}Ba_xCuO_{4+\delta}$ single crystals. Onset temperatures: T_c of bulk superconductivity (SC), T_{CO} of charge stripe order (CO), T_{SO} of spin stripe order (SO), and T_{LT} of the low-temperature structural phases LTT and LTLO. Figure from Ref. [37]

bulk superconductivity gets mostly suppressed. Also as described earlier, upon cooling, there is a tilting pattern change of the CuO_6 octahedra from LTO to LTT at the transition temperature T_{LT}, which is coincident with the charge ordering temperature T_{CO} for a wide doping range. Actually the nature of this tilting pattern change while crossing the transition temperature is still controversial. So, in this section we would focus on these superlattice dynamics in the LBCO materials while crossing the transition temperature.

4.2.2 Local and long-range tilt correlation dispute

There is a long-standing puzzle regarding the disparity of local and long-range CuO_6 octahedral tilt correlations in the underdoped regime of $La_{2-x}Ba_xCuO_{4+\delta}$. Careful powder diffraction studies [39–41] of the structural phase diagram revealed a low-temperature transition (≈60 K) to a crystal structure with inequivalent Cu-O bonds in orthogonal directions within the CuO_2 planes. This structural anisotropy is associated with a particular pattern of tilts of the CuO_6 octahedra, that pins charge stripes [38]. Given the strong relation between the electronic properties and the crystal symmetry, it is important to understand the nature of the structural transitions in $La_{2-x}Ba_xCuO_{4+\delta}$.

In the LBCO materials, there is a phase transition from the LTT-like tilt to the LTO-like tilt. From the powder [40, 41] and single-crystal diffraction studies [37, 42], it is believed to be a first order transition that involves a change in the tilt direction of the CuO_6 octahedra, which means when heating up to the LTO phase, the tilt direction suddenly changes from the [100] to the [110] direction. However, pair-distribution-function [43] and X-ray absorption fine structure analysis [44], which look at the short-range local correlations, gave a quite different conclusion about this transition. They found the LTT-like tilt remains unaffected by warming through the transition, retaining the low-temperature tilt pattern to higher temperature. In order to understand the origin of this dispute on the local and long-range tilt correlations, we use neutron scattering to trace the behaviors of a LTT superlattice peak (330), when heating up to the high-temperature LTO phase.

Inelastic neutron scattering experiment was conducted using the HYSPEC instrument at the Spallation Neutron Source, Oak Ridge National Laboratory. For the experiment on HYSPEC, the crystal was mounted in a Displex closed-cycle cryostat. With the c axis vertical, scattering wave vectors **Q**=$(H, K, 0)$ are in the horizontal scattering plane. A fixed incident energy of 27 meV and a chopper frequency of 300 Hz were used for all data, and the graphite-crystal array in the incident beam was put in the flat mode (no vertical focusing) to improve the resolution along Q_z. For a typical measurement, the position-sensitive detector tank was placed at a particular mean scattering angle, and then measurements were collected for a series of sample orientations, involving rotations about the vertical axis in steps of 0.2deg. Slices of data corresponding to particular planes in energy and wave-vector space can then be plotted from the large data set. Wave-vector will be expressed in units of $(2\pi/a, 2\pi/b, 2\pi/c)$ with $a = b =$ 5.355 A and c=13.2 A, corresponding to the LTT phase.

The measurements of the soft phonon that tilts along the Cu-O bonds were performed in the vicinity of the (330) position, which corresponds to a superlattice peak in the LTT but not the LTO phase. To sample the fluctuations associated with the tilts of the LTO phase, it was necessary to tilt the sample so as to put (032) in the scattering plane. We then looked at the behavior along (H,3,2).

4.2.3 Temperature dependence of LTT-superlattice peak dispersion at low energy

The inelastic scattering about the (330) reciprocal point of our $\mathrm{La}_{1.875}\mathrm{Ba}_{0.125}\mathrm{CuO}_{4+\delta}$ is shown in Figure 4.6. The cuts in reciprocal space that were taken are shown schematically in Figure 4.6*(a)*. Fig. 4.6*(b)* and 4.6*(d)* show the dispersion of excitations along the transverse and longitudinal directions, respectively, within the LTO phase at T=180 K. In both cases, one can see a soft phonon with intensity that can be resolved between 2 and 10 meV. In the transverse direction, these excitations connect to the transverse acoustic modes dispersing from the neighboring (240) and (420) fundamental Bragg points. Figure 4.6*(c)* shows that the excitations, integrated between 2 and 4 meV, have a finite width along Q_z, demonstrating that the LTT tilt fluctuations have 3D character.

Another perspective is given by the constant-energy slices shown in Figure 4.7 for several different energies, where we compare with results at 60 K, slightly above the low-temperature transition. For dispersion in the longitudinal direction, the intensity becomes quite weak as one moves away from the (330) point.

The temperature dependence of the scattering near (330) is presented in Figure 4.8. There is a clear superlattice reflection at (330) in the LTT phase at 50 K. Warming to 60 K, just across the transition to the LTO phase, very weak elastic scattering is still detectable; however, this is completely gone at 120 K. In contrast, soft phonon fluctuations (integrated over 2 to 5 meV) centered at (330) are clearly seen in the LTO phase and even in the HTT, at 250K. At 50 K, the intensity from the soft fluctuations has all condensed into the elastic superlattice peak. The temperature dependence of both the elastic and inelastic signals are summarized in Figure

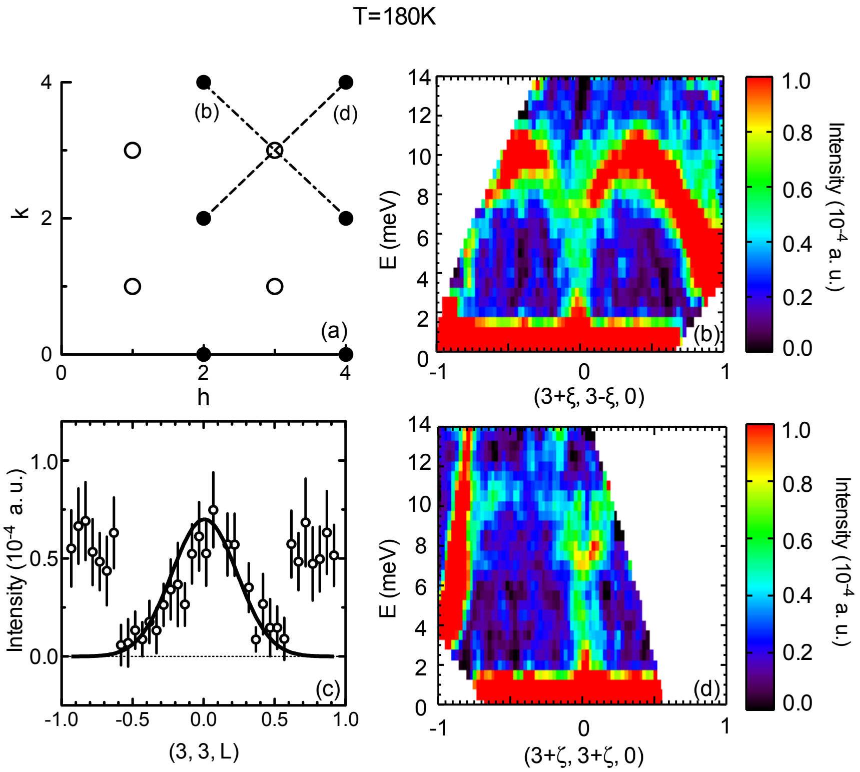

Figure 4.6: (a) Diagram of the (HK0) plane of reciprocal space indivating fundamental Bragg peaks (filled circles) and LTT superlattice peaks (open circles), with dot-dashed (dashed) line indicating the orientation of the data slice in (b)[(d)]. (b) Map of scattering intensity for E vs $\mathbf{Q}$= $(3+\xi, 3-\xi, 0)$. (c) Intensity (integrated over $2 \leq E \leq 4$ meV) vs $\mathbf{Q}$=$(3, 3, L)$. (d) Intensity map for E vs $\mathbf{Q}$= $(3+\zeta, 3-\zeta, 0)$. All measurements are at T=180 K, in the LTO phase.

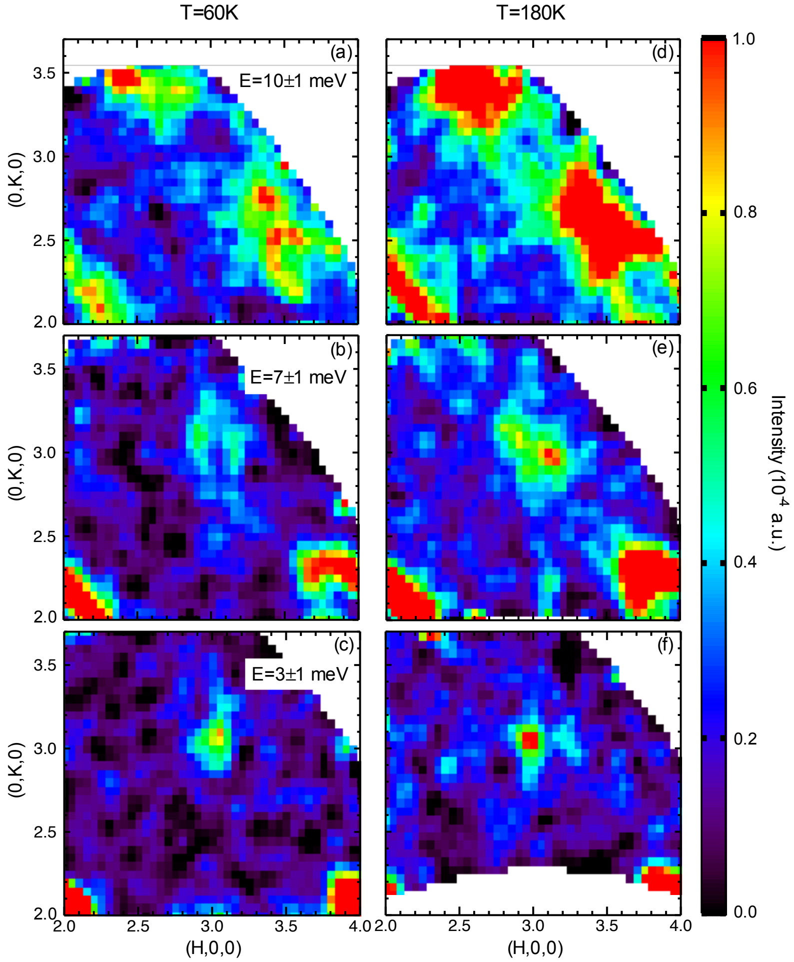

Figure 4.7: Constant-energy slices, with signal integrated over ±1 meV, through the soft-phonon scattering around (330). (a),(d) *E*=10 meV; (b),(e) *E*=7 meV; (c),(f) *E*=3 meV. Data obtained at T=60 K for (a)-(c) and 180 K for (d)-(f).

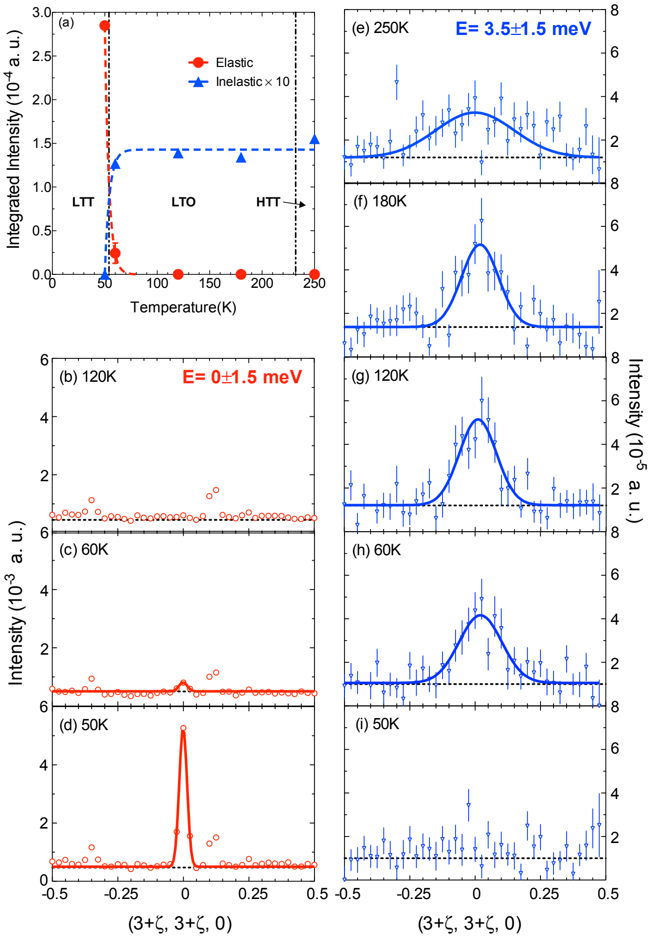

Figure 4.8: Single-crystal results at the (330) LTT superlattice position for $La_{1.875}Ba_{0.125}CuO_{4+\delta}$. (a) Summary of the temperature dependence of the elastic (red circles) and inelastic (blue triangles) integrated intensities obtained from the following panels; vertical dashed lines denote phase boundaries, while dashed lines through data points are guides to the eye. (b)-(d) Elastic channel (integrated over ± 1.5 meV) measured along the longitudinal direction at 120, 60, and 50 K, respectively. Solid lines are Gaussian-peak fits, used to determine the integrated intensity; weak, T-independent peaks are diffraction from the aluminum sample holder. (e)-(i) Inelastic signal from the soft-phonon fluctuations (2-5 meV integration) measured at 250, 180, 120, 60, and 50 K, respectively. Lines are Gaussian-peak fits.

4.8*(a)*.

The correlation length for the LTT-like tilts within the LTO phase can be estimated from the Q width of the soft-phonon scattering. Taking the inverse of the half width at half maximum for the fitted peaks in Figure 4.8*(e-h)*, we find an effective correlation length of $\approx$5 A in the LTO phase, decreasing to about half of that in the HTT phase. This is consistent with the estimate of <9 A obtained from previous PDF analysis [1].

For comparison, Figure 4.9*(a)* and 4.9*(b)* show the dispersion of tilt fluctuations in the transverse direction about the (032) position (an LTO superlattice peak) in the LTO and HTT phases, respectively. The intensity is much stronger than at (330) because of a much larger structure factor. There is a substantial intensity from soft tilt fluctuations, and even quasielastic scattering, at 250 K in the HTT phase, as seen previously [45]. In the LTO phase at 180 K, much of the low-energy weight is due to the residual soft mode that condensed at the LTT transition. We note that scattering at (032) is allowed in both the LTO and LTT phases; it follows that one cannot uniquely distinguish between orthogonal equivalent (OE) and orthogonal inequivalent (OI) soft tilt fluctuations at this **Q** point, in contrast to fluctuations at (330).

4.2.4 A possible explanation to the dispute

From the previous results, our conclusion is that the LTT-like tilt always exists, even far above the transition temperature. Despite the average structure becoming orthorhombic above T_{LT} as evidenced by Rietveld refinements of neutron scattering data, PDF analysis of the same data shows that the local structure retains its base temperature signatures consistent

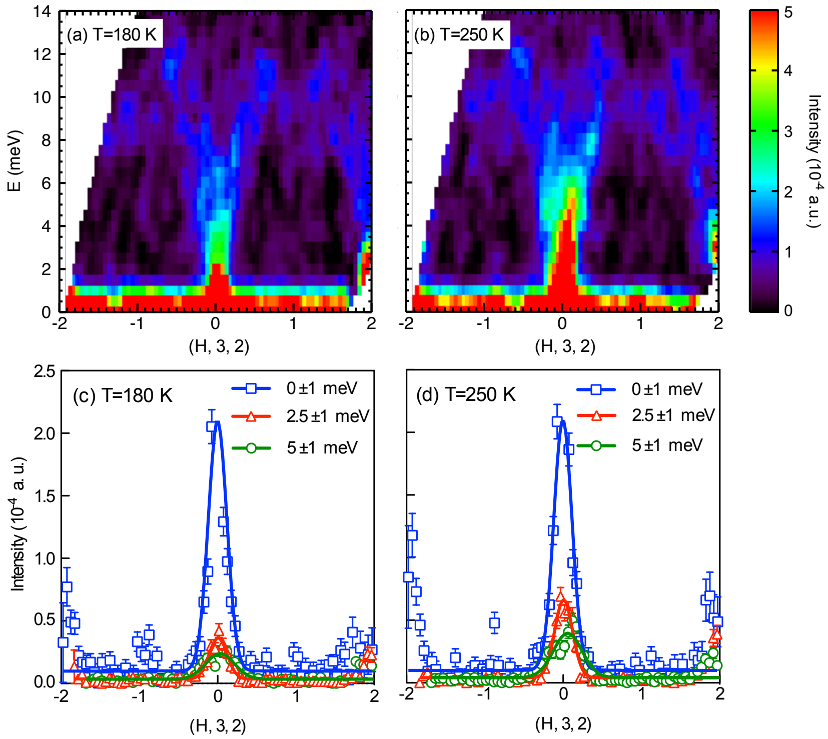

Figure 4.9: (a),(b) Intensity map as a function of energy vs **Q**=(H.3.2), shoing the transverse dispersion of tilt modes along the (032) superlattice peak position of the LTO phase, obtained at T=180 and 250 K, respectively. (c),(d) Intensity integrated over a window of ±1 meV along the transverse direction, for E=0 (blue squares), 2.5 (red triangles), and 5 meV (green circles), at T=180 and 250 K, respectively.

with orthogonal ineuivalent state up to at least T_{HT}, where LTO transforms to HTT [1]. Our neutron scattering measurements on the 1/8 doped LBCO single crystal reveal that upon heating across T_{LT} the tilt correlations become extremely short-range and dynamic. The finite width of excitations around **Q**=(3,3,L) along Q_z further indicates that the LTT tilt fluctuations have 3D character.

To address the long-existing dispute on the tilt correlations, inelastic neutron scattering provides a possible explanation. In the LTT phase, the octahedra has two kinds of tilting axis, either in [100] or [010]. When the temperature is low, these tilts remain static. As heating above the transition temperature, those tilts become dynamic. As a result, from a long-range view, or an averaged view, the CuO_6 octahedra tilt along the combined [110] direction. However, if we integrated a short-range of energy, we observe the LTT-like tilts still exist, except that they become dynamic and extremely short-range. Probes like X-ray absorption fine structure analysis, which is similar to taking a snapshot of the octahedral dynamics, could thus provide us the result that the tilting pattern remains unchanged.

To summarize, from this neutron experiment we have learned more about what really happened to the octahedral tilts and how we got the conflicting conclusions from long-range or short-range probes. We have known that by heating across the transition temperature, the LTT-like tilt correlations still exist, but become dynamic and extremely short-range. To be more specific, these LTT tilt fluctuations have a 3D character.

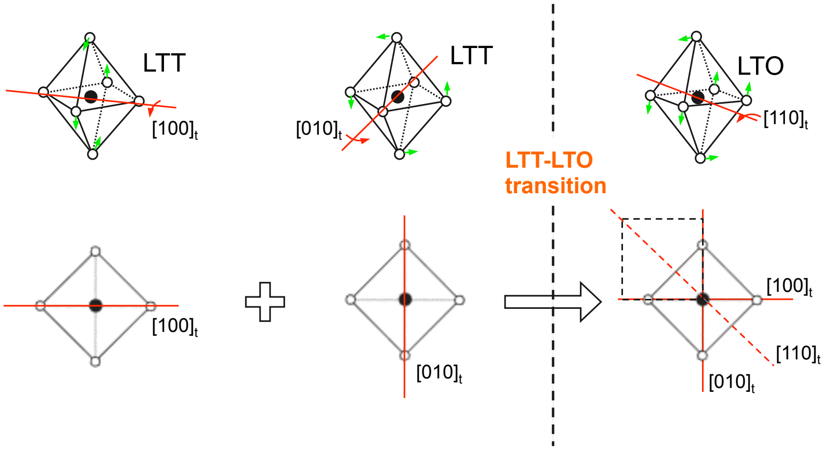

Figure 4.10: A possible explanation to resolve the conflicts on the LTT-like tilt correlations while crossing the LTT-LTO transition.

4.3 Electronic view: Dynamic charge stripes above stripe-ordering transition in $La_{2-x}Sr_xNiO_{4+\delta}$, x=1/4

4.3.1 Stripes in La-214 cuprates and nickelates

From the cuprate phase diagram, one can see that with hole doping, the long-range AF order is destroyed and the undoped magnetic domains are separated by the walls of hole. These self-organized atomic scale patterns are called stripes, including the charge stripes and spin stripes (Figure 4.3) [17, 24, 46, 47]. Neutron scattering studies in the mid-1990s led to the experimental discovery of electronic 'stripe' in the $La_{2-x}Sr_xCuO_4$ family [7]. Later studies indicate that this stripe phase is clear in layered transition-metal-oxide compounds, especially in the La-214 cuprates and nickelates.

The discovery of stripe-like magnetic and charge orders gives a new perspective on understanding the nature of high T_c superconductors [7, 48]. In cuprates, static stripe order and superconductivity are two competing parameters, since superconductivity is anomalously suppressed in materials such as $La_{2-x}Ba_xCuO_{4+\delta}$ x=1/8 that exhibit static stripe order [11, 12, 49]. While the charge stripes are compatible with superconducting correlations within the CuO_2 planes, the 90° rotation of the structural anisotropy in the adjacent CuO_2 planes [50, 51] leads to frustration of the interlayer Josephson coupling and the depression of the onset of bulk superconducting order [52, 53].

When above the stripe ordering temperature, the static, long-range stripe correlations disappear. However, the dynamic spin stripes still exist at high temperature, as reported by many groups. There has been considerable experimental work characterizing the spin and charge order of $La_2NiO_{4+\delta}$ and $La_{2-x}Sr_xNiO_{4+\delta}$ [17, 54], but the situation is much less clear when one considers the state from which the stripes develop on cooling. Also, it is still not clear how does the dynamic charge stripe correlations behave at high T, since the intensity associated with these fluctuations is very weak to detect. On the other hand, fluctuating stripes could coexist with superconductivity and play a role in the superconducting pairing mechanism [14, 15]. Unfortunately, even though substantial evidence for static stripes have been detected by diffraction techniques in cuprate materials [13, 16, 17], stripe dynamics and their role in high T_c superconductivity have long been controversial.

Directly probing the charge stripes in cuprates is complicated by their metallic properties, as well as their superconductivity. So in order to understand the dynamic stripe correlations, we decide to look at the insulating nickelates, which are isostructural with the cuprates. Besides, in nickelates, the stripe ordering and coupling to the lattice is much stronger, so lattice fluctuations due to the dynamic charges should be easier to observe.

All the above reasons make LSNO a model system to study the charge fluctuations. In fact, the first spectroscopic evidence of fluctuating charge stripes in nickelates has been provided in the pioneering work, on a 1/3 doped LSNO [55]. In light of this, we decided to look for dynamic charge stripes in $La_{2-x}Sr_xNiO_{4+\delta}$, x=0.25 sample, and to then carefully mapping out their dispersion spectrum. In the present case, we study a regime where the correlation lengths associated with charge stripes are short, so that there is no long-range translational symmetry breaking. At the same time, we show that the dispersion of the charge-stripe fluctuations is anisotropic, with a lower effective velocity along the modulation direction, comparable to that of transverse acoustic phonons. This anisotropy establishes that the electronic rotational symmetry within the NiO_2 planes is reduced to C_2, whereas the atomic structure retains C_4 symmetry. Hence, the high-temperature electronic phase appears to have nematic order [56–58].

Neutron scattering measurements were carried out on the time-of-flight spectrometer HYSPEC at beamline-14B of SNS at ORNL. The $La_{1.75}Sr_{0.25}NiO_{4+\delta}$ single crystal sample, with a mass of $\approx$10 g, was grown by the TSFZ method. For this experiment, it was mounted in a Displex closed-cycle cryostatic with (HK0) plane horizontal and c axis vertical, perpendicular to the incident neutron beam. The incident energy was fixed at 50 meV, with a Fermi chopper frequency of 360 Hz. Data were collected while rotating the sample about the vertical axis in steps of 0.5° to map a volume in reciprocal space. The detector, which covers 60° of scattering angle, was positioned with its center at 35° or 90° to cover either small or large wave-vector **Q** ranges.

4.3.2 Looking for signatures of dynamic charge stripes

The charge and spin stripes that develop in LSNO run diagonally with respect to the square lattice of Ni atoms in the NiO_2 planes. While the average crystal structure is tetragonal (space group $I4/mmm$) in the relevant doping range [59], it is easier to characterize the stripe wave vectors if we use a unit cell of doubled volume (space group $F4/mmm$); for $x = 0.25$, this corresponds to lattice parameters $a = b = 5.42$ Å and $c = 12.64$ Å. With this choice, the charge and spin wave vectors are

$$\mathbf{q}_{\text{co}} = (2\epsilon, 0, 1), \qquad \mathbf{q}_{\text{so}} = (1 \pm \epsilon, 0, 0), \tag{4.1}$$

where the coordinates are in reciprocal lattice units $(2\pi/a, 2\pi/a, 2\pi/c)$; there is also a stripe twin domain rotated by 90° in the NiO_2 plane. For the fundamental Bragg peaks, $\mathbf{G} = (H, K, L)$ the indices must be all even or all odd. It follows that the allowed superlattice peaks in the $(H, K, 0)$ reciprocal plane are

$$\mathbf{G}' \pm \mathbf{q}_{\text{co}} = (2m + 1 \pm 2\epsilon, 2n + 1, 0), \tag{4.2}$$

$$\mathbf{G} \pm \mathbf{q}_{\text{so}} = (2m + 1 \pm \epsilon, 2n, 0), \tag{4.3}$$

with $m, n =$ integers. These positions are illustrated in Figure 4.11*(a)*, in which the bright spots circled in yellow (green) represent the dynamic spin (charge) stripes at small (large) **Q**. For the case of $x = 0.33$, where the incommensurability $\epsilon = 0.33$ [47], the charge and spin peaks overlap, making it difficult to establish the relative contributions to each peak. For this reason, we have chosen to focus on $x = 0.25$ (with $\epsilon = 0.28$ [55]) where the charge and spin peaks are distinct.

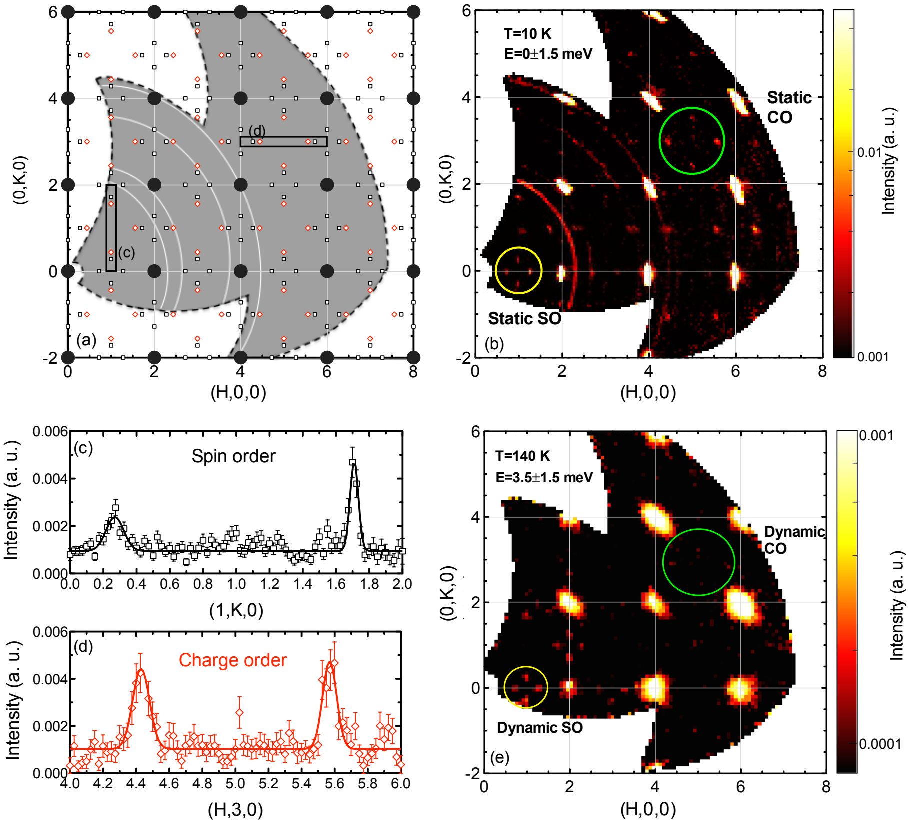

Figure 4.11: (a) A schematic diagram indicating the relative locations of fundamental Bragg peaks (black solid circles), charge-order peaks (red hollow diamonds) and spin-order peaks (black hollow squares) in the (HK0) plane of $La_{1.75}Sr_{0.25}NiO_{4+\delta}$. Shaded area illustrates the scanning range where data have been collected at 10 K. White arcs represent the aluminum powder rings. (b) Constant energy slice of (HK0) plane at 10 K. Elastic scattering intensities have been integrated with $-0.2 \leq L \leq 0.2$ and $-1.5 \leq E \leq 1.5$ meV. (c) Scans through magnetic peaks along **Q**=(1,K,0). (d) Scans through charge-order peaks along **Q**=(H,3,0). (e) Inelastic neutron scattering (integrated over $2 \leq E \leq 5$ meV, $-0.2 \leq L \leq 0.2$) measured at T_{SO}=140 K.

Characterizations of the spin and charge scattering are summarized in Figure 4.11. The magnetic peaks should be strong at small Q and decrease in intensity at large Q due to the fall of the magnetic form factor [55]. In contrast, the charge order scattering is detected through associated atomic displacements, for which the intensity should grow roughly as Q^2. In the map of low-temperature elastic scattering shown in Figure 4.11*(b)*, we expect that the peaks within the small and large circles should correspond to spin and charge order, respectively. This is confirmed by looking at particular line cuts: Figure 4.11*(c)* shows spin order peaks at $(1, \epsilon, 0)$ and $(1, 2-\epsilon, 0)$ with no significant weight at the charge order positions $(1, 1 \pm 2\epsilon, 0)$, while Figure 4.11*(c)* shows only charge order peaks at $(5 \pm 2\epsilon, 3, 0)$; Gaussian peak fitting gives $\epsilon = 0.28$. From the map of low-energy inelastic scattering obtained at 140 K, shown in Figure 4.11*(e)*, we see that the spin fluctuation scattering also falls off with Q, as expected, so that the incommensurate peaks in the large circle must correspond to charge stripe fluctuations. From here on, we will focus on the scattering near $\mathbf{Q}^*_{\rm co} = (4.44, 3, 0)$.

4.3.3 Temperature dependence of dynamic charge stripes

The temperature dependence of the elastic and low-energy inelastic scattering at $\mathbf{Q}^*_{\rm co}$ are presented in the form of line cuts in Figure 4.12*(a)* and *(b)*. From the fitted Gaussian peaks, indicated by the solid lines, we obtain the integrated elastic and inelastic intensities that are plotted vs. temperature in Figure 4.12*(c)*; for comparison, the previous triple-axis measurements of the elastic charge-order intensity are included [55]. While it is established that the charge modulation is unidirectional [60, 61], the presence of finite correlation lengths for charge order within and between planes [24, 62] means that we have, at best, a stripe (or smectic) glass, due to the quenched disorder associated with the Sr dopant ions. The elastic charge-order scattering decreases rapidly as the spin order disappears at $T_{\mathrm{so}} \approx 140$ K. Previous studies have shown that, above this point, correlation lengths shrink [29, 62–64] and finite optical conductivity turns on [65–67], indicating the importance of fluctuations and the absence of long-range order. Consistent with this, the charge-stripe fluctuations detected by inelastic scattering only become significant above T_{so}. (The small but finite "elastic" signal above 210 K appears to come from integration over quasi-elastic scattering.) While any semblance of proper smectic order is certainly destroyed above T_{so} [68], there remains the possibility of vestigial nematic order [58].

In an actual liquid-crystal system, one would distinguish the nematic from the smectic phase by the development of anisotropic peak widths. Here, the finite width due to disorder prevents that; instead, we look for anisotropy in the dispersion of the charge stripe fluctuations. Of course, because of the crystal's tetragonal symmetry, we can never observe long-range nematic order; nevertheless, by measuring at a wave vector corresponding to charge density modulations, we can selectively look at domains with the same modulation orientation.

4.3.4 Low-energy dispersion of dynamic charge stripes

To obtain meaningful data, it is necessary to measure at locations and temperatures where the signal is significant. Figure 4.13 shows a reciprocal-space map of low-energy excitations in the vicinity of $\mathbf{Q}^{*}_{\mathrm{co}}$ measured at

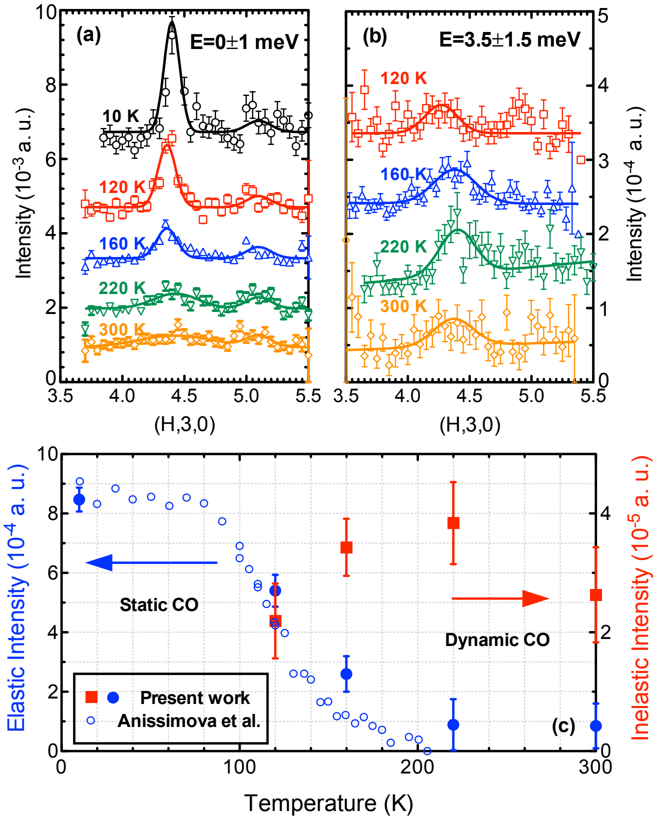

Figure 4.12: (a) Elastic scattering (integrated over $-1 \leq E \leq 1$ meV, $-0.2 \leq L \leq 0.2$) associated with static charge order along (H,3,0) measured at different temperatures. The temperature-independent peaks around $(5.1, 3, 0)$ are powder diffraction from the aluminum sample holder. (b) Inelastic signal from dynamical charge order ($-0.2 \leq L \leq 0.2$ and $2 \leq E \leq 5$ meV) measured at different temperatures. In both (a) and (b), neutron data has been normalized by the same proton charge at all temperature for a comparison. Data sets have been shift for clarity, and solid lines represent the Gaussian fitting of the data. (c) Temperature dependence of the integrated intensity of static (blue filled circles) and dynamic (red filled squares) charge-stripe correlations. For comparison, triple-axis results of static charge order (blue open circles) from Anissimova et al.[55] are interpolated.

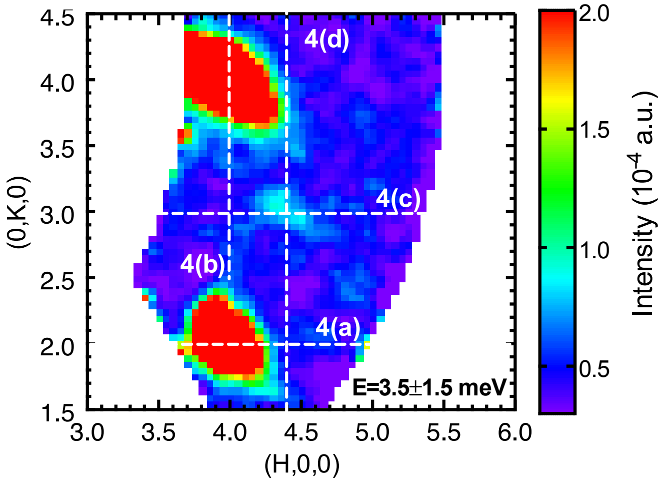

Figure 4.13: Constant energy slice ($2 \leq E \leq 5$ meV, with $-0.2 \leq L \leq 0.2$) around the charge-stripe peak at $(4.44, 3, 0)$ at 160 K for $La_{1.75}Sr_{0.25}NiO_{4+\delta}$, plotted in the $(HK0)$ plane. The strongest scattering centered at $\mathbf{G} = (4, 4, 0)$ and $(2, 4, 0)$ comes from acoustic phonons. White dashed lines and letters indicate the direction of corresponding slices in Figure 4.14.

160 K, where the fluctuation intensity initially rises to a reasonable level. The dashed lines denote the paths of the energy vs. **Q** slices plotted in Figure 4.13. Measurements at 160 K along and transverse to the modulation direction are plotted in Figure 4.14*(c)* and *(d)*, respectively; in each case, the stripe fluctuations are circled, and in Figure 4.13*(d)* they sit between acoustic phonons dispersing from neighboring Bragg peaks (see Figure 4.14). Figures 4.14(e) and (f) show constant-energy cuts through the dispersion, integrated over 2-meV bands.

Results of the low-energy excitations of charge stripes in $La_{1.75}Sr_{0.25}NiO_{4+\delta}$ have been obtained at 220 K, as shown in Figure 4.15. in Figure 4.15*(a)* and *(b)*, scattered intensity as a function of E vs **Q** through the charge-order position $\mathbf{Q}^*_{\text{co}} = (4.44, 3, 0)$ along both [100] and [010] directions.

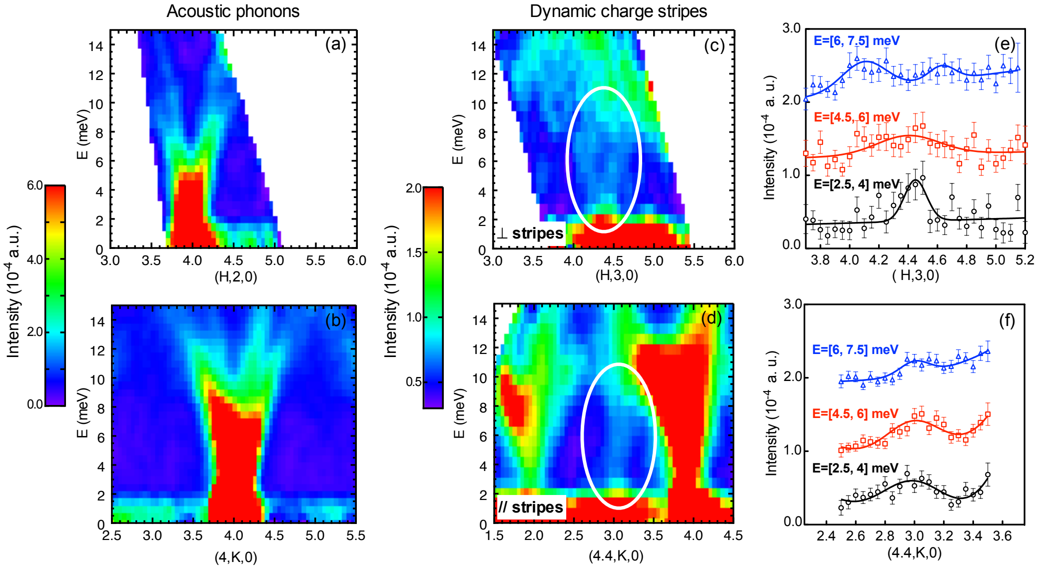

Figure 4.14: Low-energy excitations of lattice and charge stripes in La$_{1.75}$Sr$_{0.25}$NiO$_{4+\delta}$ at 160 K. (a,b) Acoustic phonon dispersing from the Bragg peak $\mathbf{Q} = (4, 2, 0)$ along the [100] direction, with integration over 1.9$\leq K \leq$2.1 (a), and from the Bragg peak $\mathbf{Q} = (4, 4, 0)$ along the [010] direction, with integration over 3.75$\leq H \leq$4.25 (b). (c,d) Scattered intensity as a function of E vs $\mathbf{Q}$ through the charge-order position $\mathbf{Q} = (4.44, 3, 0)$ along [100] direction, with integration over 2.9$\leq K \leq$3.1 (c) and [010] direction, with integration over 4.1$\leq H \leq$4.7 (d). Charge-stripe fluctuations at $(4.44, 3, 0)$ are indicated by white ovals. (e,f) Integrated scattering intensity associated with dynamic charge stripes $(4.44, 3, 0)$ measured at different energies plotted along [100] (e) and [010] (f) directions. In all cases, integration are made over -0.2$\leq L \leq$0.2 to minimize the spectral weight contributed from (5,3,1) Bragg peak. A constant incoherent elastic scattering contribution, broadened by instrumental energy resolution, has been subtracted.

Similar to the results at 160 K, we observed the anisotropic dispersion along or perpendicular to the stripes. Cuts through *(a)* and *(b)* integrated over 1.5-meV in energy are plotted in Figure 4.15*(c)* and *(d)*. The integrated energy ranges are noted in the labels, and the curves are shifted vertically for clarity. Lines in *(c)* and *(d)* are least-squares fits to Gaussian peaks plus a background. In all cases, the data have been integrated over $-0.2 \leq L \leq 0.2$, and a **Q**-independent incoherent elastic scattering contribution, broadened by instrumental energy resolution, has been subtracted.

Compared to the low-energy dispersion spectrum obtained at 160 K (see Figure 4.14), the charge-stripe fluctuations at 220 K are slightly more intense, and somewhat broader in H and K than those at 160 K, but the anisotropy of the dispersion is still clear.

In Figure 4.15*(a)* and *(c)*, there is a spurious feature near (5,3,0) for energies between 4 and 7 meV. This feature might be due to noise, but it could also be associated with the tail of phonons dispersing about the allowed Bragg peak at (5,3,1). To illustrate this issue, we compare in Figure 4.16 data slices along **Q**=(H,3,0) and (H,3,1). Besides the acoustic phonons at (5,3,1), one can also see soft phonons, associated with tilting modes of the NiO_6 octahedra at (4,3,1) and (6,3,1). Keep in mind that we have coarse resolution due to vertical focusing in the [001] direction and that the phonon dispersion is generally weaker in that direction. The charge fluctuation scattering is definitely broad in L; however, we have to integrate over a restricted L range in order to minimize the contamination from various lattice excitations with minima at $L = \pm 1$.

The data in Figure 4.14*(a)* and *(b)* show acoustic phonons at fundamental Bragg reflections for reference; note that these panels have an intensity scale that is 10 times greater than that for *(c)* and *(d)*, and that the stripe fluctuations have an intensity that is about two orders of magnitude

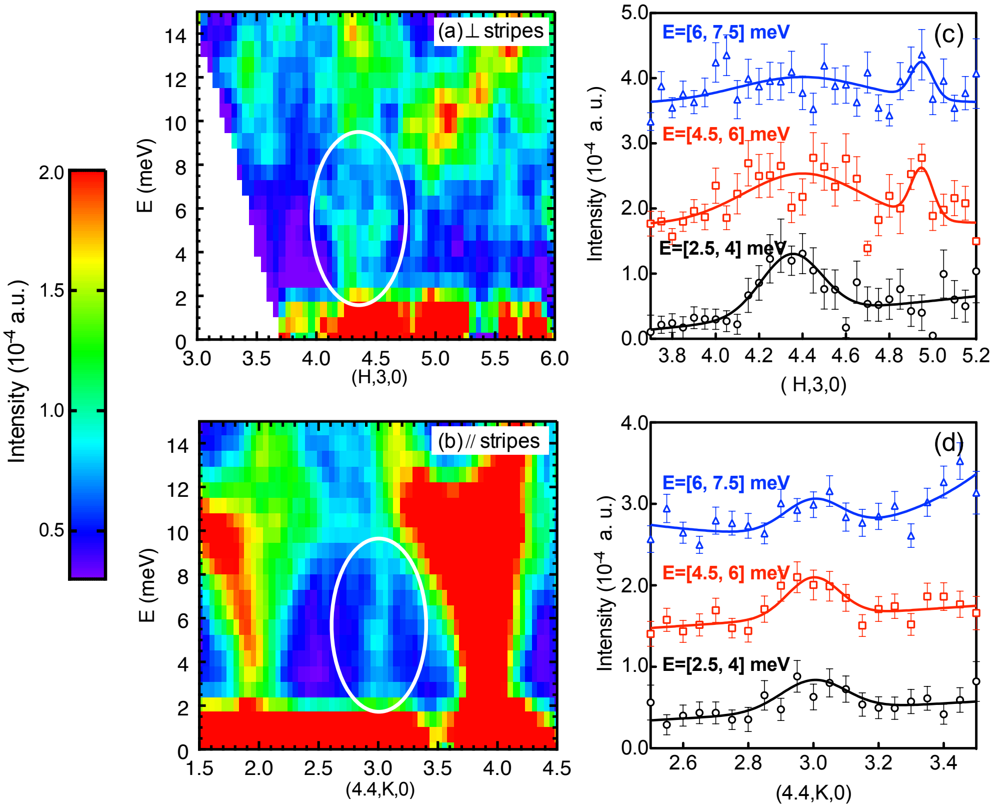

Figure 4.15: Low-energy excitations of lattice and charge stripes in $La_{1.75}Sr_{0.25}NiO_{4+\delta}$ at 220 K.

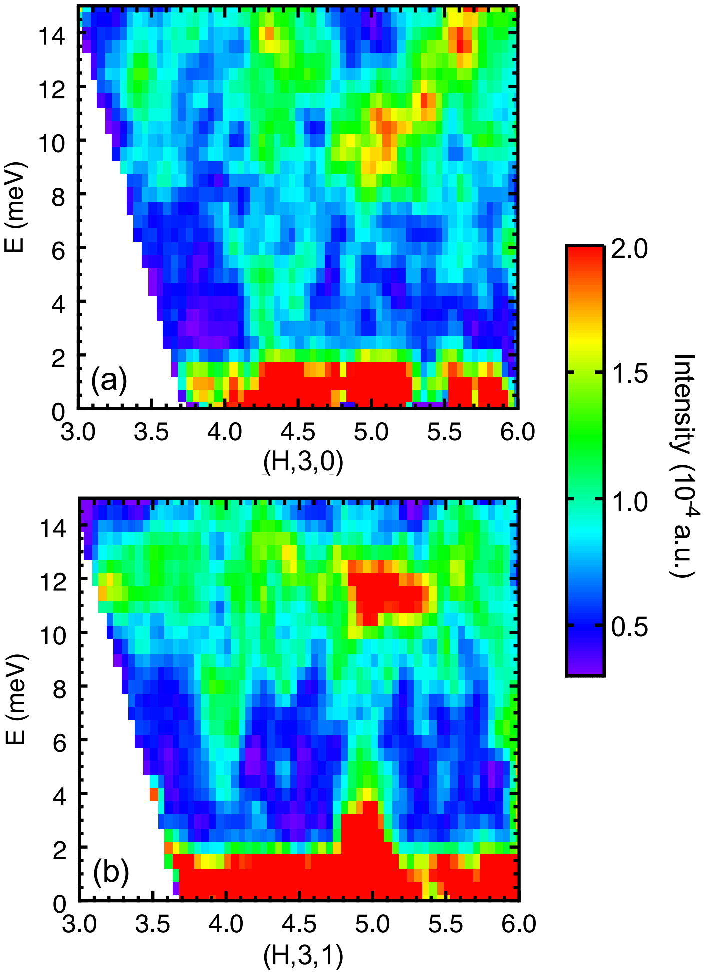

Figure 4.16: Data slices at 220 K along **Q**=(H,3,0) (a) and (H,3,1) (b), with integration over $2.9 \leq K \leq 3.1$

weaker than that of the acoustic modes.

The window for viewing the stripe fluctuations is small—by an energy of 9 meV or so they run into the transverse acoustic modes dispersing from the $(4, 4, 0)$ Bragg peak (see Fig. 4.13). It is notable that we do not see any significant interaction between the stripe fluctuations and the acoustic mode. In contrast to the soft-mode behavior detected in association with the charge-density-wave order in underdoped $YBa_2Cu_3O_{6+x}$ [69, 70], we appear to have overlapping dispersions. The slowest dispersion is in the direction perpendicular to the stripes, where the effective velocity is comparable to that of transverse acoustic modes shown in Figure 4.14*(b)*. As this is the modulation direction, it is also associated with the observation that the incommensurability ϵ increases towards $1/3$ as the temperature approaches T_{co} [62, 71]. The velocity parallel to the stripes is not resolved but might be comparable to that of the longitudinal acoustic mode that is resolved at energies above 10 meV in Figure 4.14*(a)* and *(b)*. Note, however, that the comparison with phonon velocities is only to provide relevant scale. The specific anisotropy of the fluctuations is not consistent with what one observes for normal acoustic phonons about a structural superlattice peak.

While the stripe fluctuations are more diffuse at 220 K, where static stripe order is absent, the anisotropy is still apparent and the excitations show no sign of a gap. The combination of the characteristic modulation wave vector and the dispersion anisotropy provide a strong case for the presence of electronic nematic order. This is of particular significance given the four-fold rotational symmetry of the average crystal structure. (Note that some of the best evidence for nematic order in cuprates occurs in samples where the crystal structure has reduced rotational symmetry [72].) The nematic order in this case is formed of fluctuating charge stripes, as in the original proposal by Kivelson, Fradkin, and Emery [56]. The response at 160 K is compatible with nematic order as a vestigial version of static charge density waves [58] similar to what has been observed by scanning tunneling microscopy in $Bi_2Sr_2CaCu_2O_{6+\delta}$ [73, 74]. The charge stripe correlations certainly involve a coupling to the lattice, as without nuclear displacements we would not be able to detect the charge stripes with neutrons. In a sense, this is polaronic; however, it is not made up of individually dressed holes, but is, instead, an emergent collective state, one not easily captured by current *ab initio* techniques.

4.4 Conclusions and discussions

In the 1/4 doped $La_{2-x}Sr_xNiO_{4+\delta}$, the observed inelastic scattering intensity associated with the charge-stripe fluctuations at high temperature is a sign of the existence of a local-like stripe phase. In another word, usually we consider that above the stripe ordering temperature, the stripes get melted and then the materials should no longer remain in the stripe phase. Our results suggests that even when above the stripe ordering temperature, the local-like stripes become dynamic but still exist. Actually the ultrafast studies also have shown the dynamic precursors of stripe formation in the nickelates [66]. And also, the fluctuating charge order seems to be universal in both cuprates and iron based superconductors [75]. Thus, the fluctuations of charge order may provide an alternative to spin fluctuations as a underlying mechanism to understand the unconventional superconductivity. Besides, by mapping out the dispersion spectrum of the dynamic charge stripes the anisotropic low-energy dispersion above the stripe-ordering transition has been observed for the first time, providing evidence for the presence of electronic nematic order.

In summary, from the two inelastic neutron scattering experiments described in this chapter, we found a common feature in the LBCO and LSNO materials. From the structural view, in LBCO, the dynamic LTT-like tilts can be found within the LTO and even HTT phase, and the correlations become dynamic and short-range. From the electronic view, in LSNO, dynamic charge stripe correlations, which develop from the static charge stripe at low T, can be found far above the stripe ordering temperature. In these two cases, we found something in common. The correlations that were static and long-range at low temperature do not disappear at high temperature. Surprisingly, they exist locally and become dynamic. This makes us notice the universal phenomena in the strong correlated system: dynamic precursors of stripe formations appear far above the long-range ordering temperature. And we could consider those structural transitions as a disorder to order transition, instead of the conventional first or second order transition, because there may be no change in the ordering parameter.

References

[1] Emil S. Bozin, Ruidan Zhong, Kevin R. Knox, Genda Gu, John P. Hill, John M. Tranquada, and Simon J. L. Billinge. Reconciliation of local and long-range tilt correlations in underdoped $La_{2-x}Ba_xCuO_4$ $(0 \leq x \leq 0.155)$. *Phys. Rev. B*, 91:054521, Feb 2015.

[2] Ruidan Zhong, Barry L. Winn, Genda Gu, Dmitry Reznik, and J. M. Tranquada. Evidence for a nematic phase in $\mathrm{La_{1.75}Sr_{0.25}NiO_4}$. *Phys. Rev. Lett.*, 118:177601, Apr 2017.

[3] J. G. Bednorz and K. A. Müller. Possible high Tc superconductivity in the Ba-La-Cu-O system. *Zeitschrift für Physik B Condensed Matter*, 64(2):189–193, 1986.

[4] J Orenstein and AJ Millis. Advances in the physics of high-temperature superconductivity. *Science*, 288(5465):468–474, 2000.

[5] Damian Rybicki, Michael Jurkutat, Steven Reichardt, Czesław Kapusta, and Jürgen Haase. Perspective on the phase diagram of cuprate high-temperature superconductors. *Nature Communications*, 7:11413 EP –, 05 2016.

[6] H. Saadaoui, Z. Salman, H. Luetkens, T. Prokscha, A. Suter, W. A. MacFarlane, Y. Jiang, K. Jin, R. L. Greene, E. Morenzoni, and R. F. Kiefl. The phase diagram of electron-doped $La_{2-x}Ce_xCuO_{4-\delta}$. *Nature Communications*, 6:6041 EP, 01 2015.

[7] J. M. Tranquada, B. J. Sternlieb, J. D. Axe, Y. Nakamura, and S. Uchida. Evidence for stripe correlations of spins and holes in copper oxide superconductors. *Nature*, 375(6532):561–563, 06 1995.

[8] Victor J Emery and SA Kivelson. Frustrated electronic phase separation and high-temperature superconductors. *Physica C: Superconductivity*, 209(4):597–621, 1993.

[9] J. M. Tranquada, J. D. Axe, N. Ichikawa, A. R. Moodenbaugh, Y. Nakamura, and S. Uchida. Coexistence of, and competition between, superconductivity and charge-stripe order in $La_{1.6-x}Nd_{0.4}Sr_xCuO_4$. *Phys. Rev. Lett.*, 78:338–341, Jan 1997.

[10] A. R. Moodenbaugh, Youwen Xu, M. Suenaga, T. J. Folkerts, and R. N. Shelton. Superconducting properties of $La_{2-x}Ba_xCuO_4$. *Phys. Rev. B*, 38:4596–4600, Sep 1988.

[11] B. BÃijchner, M. Cramm, M. Braden, W. Braunisch, O. Hoffels, W. Schnelle, R. MÃijller, A. Freimuth, W. Schlabitz, G. Heger, D. I. Khomskii, and D. Wohlleben. Competition between structural and superconducting transition in (LaNd)-Sr-Cu-O. *EPL (Europhysics Letters)*, 21(9):953, 1993.

[12] N. Ichikawa, S. Uchida, J. M. Tranquada, T. Niemöller, P. M. Gehring, S.-H. Lee, and J. R. Schneider. Local magnetic order vs superconductivity in a layered cuprate. *Phys. Rev. Lett.*, 85:1738–1741, Aug 2000.

[13] Masaki Fujita. Neutron scattering studies of stripe correlations in curate oxide superconductors. *Physica C: Superconductivity*, 481:23 – 30, 2012. Stripes and Electronic Liquid Crystals in Strongly Correlated Materials.

[14] V. J. Emery and S. A. Kivelson. Importance of phase fluctuations in superconductors with small superfluid density. *Nature*, 374(6521):434–437, 03 1995.

[15] S. A. Kivelson, I. P. Bindloss, E. Fradkin, V. Oganesyan, J. M. Tranquada, A. Kapitulnik, and C. Howald. How to detect fluctuating stripes in the high-temperature superconductors. *Rev. Mod. Phys.*, 75:1201–1241, Oct 2003.

[16] M. HÃijcker. Structural aspects of materials with static stripe order. *Physica C: Superconductivity*, 481:3 – 14, 2012. Stripes and Electronic Liquid Crystals in Strongly Correlated Materials.

[17] Holger Ulbrich and Markus Braden. Neutron scattering studies on stripe phases in non-cuprate materials. *Physica C: Superconductivity*, 481:31 – 45, 2012. Stripes and Electronic Liquid Crystals in Strongly Correlated Materials.

[18] J. M. Tranquada, D. J. Buttrey, V. Sachan, and J. E. Lorenzo. Simultaneous ordering of holes and spins in $\mathrm{La_2NiO_{4.125}}$. *Phys. Rev. Lett.*, 73:1003–1006, Aug 1994.

[19] J. M. Tranquada, J. E. Lorenzo, D. J. Buttrey, and V. Sachan. Cooperative ordering of holes and spins in $\mathrm{La_2NiO_{4.125}}$. *Phys. Rev. B*, 52:3581–3595, Aug 1995.

[20] S. M. Hayden, G. H. Lander, J. Zarestky, P. J. Brown, C. Stassis, P. Metcalf, and J. M. Honig. Incommensurate magnetic correlations in $\mathrm{La_{1.8}Sr_{0.2}NiO_4}$. *Phys. Rev. Lett.*, 68:1061–1064, Feb 1992.

[21] V. Sachan, D. J. Buttrey, J. M. Tranquada, J. E. Lorenzo, and G. Shirane. Charge and spin ordering in $\mathrm{La_{2-x}Sr_xNiO_{4.00}}$ with x =0.135 and 0.20. *Phys. Rev. B*, 51:12742–12746, May 1995.

[22] C. H. Chen, S-W. Cheong, and A. S. Cooper. Charge modulations in $\mathrm{La}_{2-x}\mathrm{Sr}_x\mathrm{NiO}_{4+y}$: Ordering of polarons. *Phys. Rev. Lett.*, 71:2461–2464, Oct 1993.

[23] A. P. Ramirez, P. L. Gammel, S-W. Cheong, D. J. Bishop, and P. Chandra. Charge modulation in $\mathrm{La}_{1.67}\mathrm{Sr}_{0.33}\mathrm{NiO}_4$: A bulk thermodynamic study. *Phys. Rev. Lett.*, 76:447–450, Jan 1996.

[24] H. Yoshizawa, T. Kakeshita, R. Kajimoto, T. Tanabe, T. Katsufuji, and Y. Tokura. Stripe order at low temperatures in $\mathrm{La}_{2-x}\mathrm{Sr}_x\mathrm{NiO}_4$ with $0.289 \lesssim x \lesssim 0.5$. *Phys. Rev. B*, 61:R854–R857, Jan 2000.

[25] R. Kajimoto, T. Kakeshita, H. Yoshizawa, T. Tanabe, T. Katsufuji, and Y. Tokura. Hole concentration dependence of the ordering process of the stripe order in $\mathrm{La}_{2-x}\mathrm{Sr}_x\mathrm{NiO}_4$. *Phys. Rev. B*, 64:144432, Sep 2001.

[26] Yasuaki Oohara, Ryoichi Kajimoto, Teruhisa Kakeshita, Hideki Yoshizawa, Takaya Tanabe, Takuro Katsufuji, Kyoko Ishizaka, Yasujiro Taguchi, and Yoshinori Tokura. Neutron scattering study of the charge and the magnetic ordering in $\mathrm{La}_{2-x}\mathrm{Sr}_x\mathrm{NiO}_4$. *Physica B: Condensed Matter*, 329 - 333, Part 2:725 – 726, Jan 2003. Proceedings of the 23rd International Conference on Low Temperature Physics.

[27] K. Ishizaka, T. Arima, Y. Murakami, R. Kajimoto, H. Yoshizawa, N. Nagaosa, and Y. Tokura. Commensurate-incommensurate crossover of charge stripe in $\mathrm{La}_{2-x}\mathrm{Sr}_x\mathrm{NiO}_4$ $(x \sim 1/3)$. *Phys. Rev. Lett.*, 92:196404, May 2004.

[28] S. Wakimoto, G. Shirane, Y. Endoh, K. Hirota, S. Ueki, K. Yamada, R. J. Birgeneau, M. A. Kastner, Y. S. Lee, P. M. Gehring, and S. H. Lee. Observation of incommensurate magnetic correlations at the

lower critical concentration for superconductivity in $\mathrm{La}_{2-x}\mathrm{Sr}_x\mathrm{CuO}_4$ $(x = 0.05)$. *Phys. Rev. B*, 60:R769–R772, Jul 1999.

[29] S.-H. Lee, J. M. Tranquada, K. Yamada, D. J. Buttrey, Q. Li, and S.-W. Cheong. Freezing of a stripe liquid. *Phys. Rev. Lett.*, 88:126401, Mar 2002.

[30] P. Bourges, Y. Sidis, M. Braden, K. Nakajima, and J. M. Tranquada. High-energy spin dynamics in $\mathrm{La}_{1.69}\mathrm{Sr}_{0.31}\mathrm{NiO}_4$. *Phys. Rev. Lett.*, 90:147202, Apr 2003.

[31] J. M. Tranquada, K. Nakajima, M. Braden, L. Pintschovius, and R. J. McQueeney. Bond-stretching-phonon anomalies in stripe-ordered $\mathrm{La}_{1.69}\mathrm{Sr}_{0.31}\mathrm{NiO}_4$. *Phys. Rev. Lett.*, 88:075505, Jan 2002.

[32] Eiji Kaneshita, Masanori Ichioka, and Kazushige Machida. Phonon anomalies due to collective stripe modes in high T_c cuprates. *Phys. Rev. Lett.*, 88:115501, Feb 2002.

[33] D. Reznik. Phonon anomalies and dynamic stripes. *Physica C: Superconductivity*, 481:75 – 92, 2012. Stripes and Electronic Liquid Crystals in Strongly Correlated Materials.

[34] T. Katsufuji, T. Tanabe, T. Ishikawa, Y. Fukuda, T. Arima, and Y. Tokura. Optical spectroscopy of the charge-ordering transition in $\mathrm{La}_{1.67}\mathrm{Sr}_{0.33}\mathrm{NiO}_4$. *Phys. Rev. B*, 54:R14230–R14233, Nov 1996.

[35] J. M. Tranquada, J. D. Axe, N. Ichikawa, Y. Nakamura, S. Uchida, and B. Nachumi. Neutron-scattering study of stripe-phase order of holes and spins in $\mathrm{La}_{1.48}\mathrm{Nd}_{0.4}\mathrm{Sr}_{0.12}\mathrm{CuO}_4$. *Phys. Rev. B*, 54:7489–7499, Sep 1996.

[36] M. v. Zimmermann, A. Vigliante, T. NiemÃűller, N. Ichikawa, T. Frello, J. Madsen, P. Wochner, S. Uchida, N. H. Andersen, J. M. Tranquada, D. Gibbs, and J. R. Schneider. Hard-X-ray diffraction study of charge stripe order in $La_{1.48}Nd_{0.4}Sr_{0.12}CuO_4$. *EPL (Europhysics Letters)*, 41(6):629, 1998.

[37] M. Hücker, M. v. Zimmermann, G. D. Gu, Z. J. Xu, J. S. Wen, Guangyong Xu, H. J. Kang, A. Zheludev, and J. M. Tranquada. Stripe order in superconducting $La_{2-x}Ba_xCuO_4$ $(0.095 \leqslant x \leqslant 0.155)$. *Phys. Rev. B*, 83:104506, Mar 2011.

[38] M. Fujita, H. Goka, K. Yamada, J. M. Tranquada, and L. P. Regnault. Stripe order, depinning, and fluctuations in $La_{1.875}Ba_{0.125}CuO_{4+\delta}$ and $La_{1.875}Ba_{0.075}Sr_{0.050}CuO_4$. *Phys. Rev. B*, 70:104517, Sep 2004.

[39] J. D. Axe, A. H. Moudden, D. Hohlwein, D. E. Cox, K. M. Mohanty, A. R. Moodenbaugh, and Youwen Xu. Structural phase transformations and superconductivity in $La_{2-x}Ba_xCuO_{4+\delta}$. *Phys. Rev. Lett.*, 62:2751–2754, Jun 1989.

[40] Takashi Suzuki and Toshizo Fujita. Anomalous change in crystalline structure of $La_{2-x}Ba_xCuO_{4+\delta}$. *Journal of the Physical Society of Japan*, 58(6):1883–1886, 1989.

[41] S. J. L. Billinge, G. H. Kwei, A. C. Lawson, J. D. Thompson, and H. Takagi. Superconductivity and the low-temperature orthorhombic to tetragonal phase transition in $La_{2-x}Ba_xCuO_{4+\delta}$. *Phys. Rev. Lett.*, 71:1903–1906, Sep 1993.

[42] Y. Zhao, B. D. Gaulin, J. P. Castellan, J. P. C. Ruff, S. R. Dunsiger, G. D. Gu, and H. A. Dabkowska. High-resolution x-ray scattering stud-

ies of structural phase transitions in underdoped $La_{2-x}Ba_xCuO_{4+\delta}$. *Phys. Rev. B*, 76:184121, Nov 2007.

[43] S. J. L. Billinge, G. H. Kwei, and H. Takagi. Local octahedral tilts in $La_{2-x}Ba_xCuO_{4+\delta}$: Evidence for a new structural length scale. *Phys. Rev. Lett.*, 72:2282–2285, Apr 1994.

[44] D. Haskel, E. A. Stern, F. Dogan, and A. R. Moodenbaugh. XAFS study of the low-temperature tetragonal phase of $La_{2-x}Ba_xCuO_{4+\delta}$: Disorder, stripes, and T_c suppression at $x = 0.125$. *Phys. Rev. B*, 61:7055–7076, Mar 2000.

[45] Hiroyuki Kimura, Yukio Noda, Hideto Goka, Masaki Fujita, Kazuyoshi Yamada, and Gen Shirane. Soft phonons and structural phase transitions in $La_{1.875}Ba_{0.125}CuO_{4+\delta}$. *Journal of the Physical Society of Japan*, 74(1):445–449, 2005.

[46] JM Tranquada, DJ Buttrey, V Sachan, and JE Lorenzo. Simultaneous ordering of holes and spins in $La_2NiO_{4.125}$. *Physical review letters*, 73(7):1003, 1994.

[47] S.-H. Lee and S-W. Cheong. Melting of quasi-two-dimensional charge stripes in $La_{5/3}Sr_{1/3}NiO_4$. *Phys. Rev. Lett.*, 79:2514–2517, Sep 1997.

[48] J. M. Tranquada, J. D. Axe, N. Ichikawa, A. R. Moodenbaugh, Y. Nakamura, and S. Uchida. Coexistence of, and competition between, superconductivity and charge-stripe order in $La_{1.6-x}Nd_{0.4}Sr_xCuO_4$. *Phys. Rev. Lett.*, 78:338–341, Jan 1997.

[49] A. R. Moodenbaugh, Youwen Xu, M. Suenaga, T. J. Folkerts, and R. N. Shelton. Superconducting properties of $La_{2-x}Ba_xCuO_{4+\delta}$. *Phys. Rev. B*, 38:4596–4600, Sep 1988.

[50] Q. Li, M. Hücker, G. D. Gu, A. M. Tsvelik, and J. M. Tranquada. Two-dimensional superconducting fluctuations in stripe-ordered $La_{1.875}Ba_{0.125}CuO_4$. *Phys. Rev. Lett.*, 99:067001, Aug 2007.

[51] J. M. Tranquada, G. D. Gu, M. Hücker, Q. Jie, H.-J. Kang, R. Klingeler, Q. Li, N. Tristan, J. S. Wen, G. Y. Xu, Z. J. Xu, J. Zhou, and M. v. Zimmermann. Evidence for unusual superconducting correlations coexisting with stripe order in $La_{1.875}Ba_{0.125}CuO_{4+\delta}$. *Phys. Rev. B*, 78:174529, Nov 2008.

[52] Erez Berg, Eduardo Fradkin, Steven A Kivelson, and John M Tranquada. Striped superconductors: how spin, charge and superconducting orders intertwine in the cuprates. *New Journal of Physics*, 11(11):115004, 2009.

[53] A. Himeda, T. Kato, and M. Ogata. Stripe states with spatially oscillating d-wave superconductivity in the two-dimensional $t - t' - j$ model. *Phys. Rev. Lett.*, 88:117001, Feb 2002.

[54] John M Tranquada, Adolfo Avella, and Ferdinando Mancini. Spins, stripes, and superconductivity in hole-doped cuprates. In *AIP Conference Proceedings*, volume 1550, pages 114–187. AIP, 2013.

[55] S. Anissimova, D. Parshall, G. D. Gu, K. Marty, M. D. Lumsden, Songxue Chi, J. A. Fernandez-Baca, D. L. Abernathy, D. Lamago, J. M. Tranquada, and D. Reznik. Direct observation of dynamic charge stripes in $La_{2-x}Sr_xNiO_{4+\delta}$. *Nature Communications*, 5:3467 EP –, 03 2014.

[56] S. A. Kivelson, E. Fradkin, and V. J. Emery. Electronic liquid-crystal phases of a doped Mott insulator. *Nature*, 393(6685):550–553, 06 1998.

[57] Eduardo Fradkin, Steven A Kivelson, Michael J Lawler, James P Eisenstein, and Andrew P Mackenzie. Nematic fermi fluids in condensed matter physics. *Annu. Rev. Condens. Matter Phys.*, 1(1):153–178, 2010.

[58] Laimei Nie, Gilles Tarjus, and Steven Allan Kivelson. Quenched disorder and vestigial nematicity in the pseudogap regime of the cuprates. *Proceedings of the National Academy of Sciences*, 111(22):7980–7985, 2014.

[59] M Hücker, K Chung, M Chand, T Vogt, JM Tranquada, and DJ Buttrey. Oxygen and strontium codoping of La_2NiO_4: Room-temperature phase diagrams. *Physical Review B*, 70(6):064105, 2004.

[60] Jianqi Li, Yimei Zhu, J. M. Tranquada, K. Yamada, and D. J. Buttrey. Transmission-electron-microscopy study of charge-stripe order in $La_{1.725}Sr_{0.275}NiO_4$. *Phys. Rev. B*, 67:012404, Jan 2003.

[61] M. Hücker, M. v. Zimmermann, R. Klingeler, S. Kiele, J. Geck, S. N. Bakehe, J. Z. Zhang, J. P. Hill, A. Revcolevschi, D. J. Buttrey, B. Büchner, and J. M. Tranquada. Unidirectional diagonal order and three-dimensional stacking of charge stripes in orthorhombic $Pr_{1.67}Sr_{0.33}NiO_4$ and $Nd_{1.67}Sr_{0.33}NiO_4$. *Phys. Rev. B*, 74:085112, Aug 2006.

[62] J. M. Tranquada, D. J. Buttrey, and V. Sachan. Incommensurate stripe order in $La_{2-x}Sr_xNiO_{4+\delta}$ with x=0.225. *Phys. Rev. B*, 54:12318–12323, Nov 1996.

[63] PD Spencer, ME Ghazi, SB Wilkins, PD Hatton, SD Brown, D Prabhakaran, and AT Boothroyd. Charge stripe glasses in $La_{2-x}Sr_xNiO_{4+\delta}$

for 0.20< x< 0.25. *The European Physical Journal B-Condensed Matter and Complex Systems*, 46(1):27–32, 2005.

[64] Wei-Sheng Lee, YD Chuang, RG Moore, Y Zhu, L Patthey, M Trigo, DH Lu, PS Kirchmann, O Krupin, M Yi, et al. Phase fluctuations and the absence of topological defects in a photo-excited charge-ordered nickelate. *Nature communications*, 3:838, 2012.

[65] C. C. Homes, J. M. Tranquada, Q. Li, A. R. Moodenbaugh, and D. J. Buttrey. Mid-infrared conductivity from mid-gap states associated with charge stripes. *Phys. Rev. B*, 67:184516, May 2003.

[66] Giacomo Coslovich, Bernhard Huber, W-S Lee, Y-D Chuang, Y Zhu, T Sasagawa, Z Hussain, HA Bechtel, MC Martin, Z-X Shen, et al. Ultrafast charge localization in a stripe-phase nickelate. *Nature communications*, 4, 2013.

[67] J. Lloyd-Hughes, D. Prabhakaran, A. T. Boothroyd, and M. B. Johnston. Low-energy collective dynamics of charge stripes in the doped nickelate $La_{2-x}Sr_xNiO_{4+\delta}$ observed with optical conductivity measurements. *Phys. Rev. B*, 77:195114, May 2008.

[68] Oron Zachar and Igor Zaliznyak. Dimensional crossover and charge order in half-doped manganites and cobaltites. *Phys. Rev. Lett.*, 91:036401, Jul 2003.

[69] M Le Tacon, A Bosak, SM Souliou, G Dellea, T Loew, R Heid, KP Bohnen, G Ghiringhelli, M Krisch, and B Keimer. Inelastic X-ray scattering in $YBa_2Cu_3O_{6.6}$ reveals giant phonon anomalies and elastic central peak due to charge-density-wave formation. *Nature Physics*, 10(1):52–58, 2014.

[70] Elizabeth Blackburn, Johan Chang, AH Said, BM Leu, Ruixing Liang, DA Bonn, WN Hardy, EM Forgan, and SM Hayden. Inelastic x-ray study of phonon broadening and charge-density wave formation in ortho-II-ordered $YBa_2Cu_3O_{6.54}$. *Physical Review B*, 88(5):054506, 2013.

[71] K Ishizaka, T Arima, Y Murakami, R Kajimoto, H Yoshizawa, N Nagaosa, and Y Tokura. Commensurate-incommensurate crossover of charge stripe in $La_{2-x}Sr_xNiO_{4+\delta}$ (x∼1/3). *Physical review letters*, 92(19):196404, 2004.

[72] R Daou, J Chang, David LeBoeuf, Olivier Cyr-Choiniere, Francis Laliberté, Nicolas Doiron-Leyraud, BJ Ramshaw, Ruixing Liang, DA Bonn, WN Hardy, et al. Broken rotational symmetry in the pseudogap phase of a high-Tc superconductor. *Nature*, 463(7280):519–522, 2010.

[73] MJ Lawler, K Fujita, Jhinhwan Lee, AR Schmidt, Y Kohsaka, Chung Koo Kim, H Eisaki, S Uchida, JC Davis, JP Sethna, et al. Intra-unit-cell electronic nematicity of the high-Tc copper-oxide pseudogap states. *Nature*, 466(7304):347–351, 2010.

[74] A Mesaros, K Fujita, H Eisaki, S Uchida, JC Davis, S Sachdev, J Zaanen, MJ Lawler, and Eun-Ah Kim. Topological defects coupling smectic modulations to intra-unit-cell nematicity in cuprates. *Science*, 333(6041):426–430, 2011.

[75] Erminald Bertel and Alexander Menzel. Fluctuating charge order: A universal phenomenon in unconventional superconductivity? *Symmetry*, 8(6):45, 2016.

Chapter 5

Conclusions

This dissertation has covered research on two disparate quantum materials, the topological insulators (Chapter 3) and the high temperature superconductors (Chapter 4). All experiments are aimed at exploring and having a better understanding about the unconventional superconductors.

In topological crystalline insulators SnTe and $Pb_{1-x}Sn_xTe$, we found indium substitution with the Sn or Pb atoms results in significant changes in the superconducting and topological properties. Our study of a broad range of compositions in the (Pb,Sn)Te system shows that indium doping has a nonmonotonic effect on the electronic properties, which can be explained from the standpoint of the relative location of the indium-induced impurity band and the bulk band structure. For low indium doping, samples show weak metallic resistivity as in the undoped compounds SnTe and $Pb_{1-x}Sn_xTe$. A few percent indium doping turns the $Pb_{1-x}Sn_xTe$ samples into true bulk insulators, which provides suitable platforms to study the exotic surface states that will not dominated by the bulk conduction. By increasing the In content further, superconductivity may be achieved, and the superconducting transition temperature increases with increasing In concentration. The maximum T_c is thus limited by the indium solubility in the undoped compounds. In the effort of looking for a new topological superconductor, we found that the In-substitution on the $Pb_{1-x}Sn_xTe$ system results in either bulk superconductivity or topological surface states. The goal of mixing the two characters in the same materials remains a challenge.

The Pb concentration $(1 - x)$ in the parent compound is another factor that affect the indium substitution effect on the $Pb_{1-x}Sn_xTe$. Superconductivity emerges almost immediately with indium doping in SnTe. With increasing Pb content the amount of In needed to induce superconductivity goes up, and the indium solubility suppressed. Thus the range of superconductivity with respect to indium-doping shrinks. Meanwhile, the bulk insulating region is broadens with increased Pb, and the maximum bulk resistivity that can be achieved in the $(Pb_{1-x}Sn_x)_{1-y}In_yTe$ family in the x=0.30 and 0.25 series. Those materials could provide good platforms to study the true topological 'insulators' with exotic topological surface states, in which bulk conduction would not dominate the the surface transport behavior.

To understand the nature of the indium-induced superconductivity, inelastic neutron scattering was applied to study the anomalies in the phonon density of states of the superconducting $(Pb_{1-x}Sn_x)_{1-y}In_yTe$, and the results indicate the superconductivity in the $(Pb_{1-x}Sn_x)_{1-y}In_yTe$ compounds are mediated by phonons, which suggests they are more likely conventional BCS superconductors instead of topological superconductors that we are looking for. However, the conventional superconductivity in the indium doped $Pb_{1-x}Sn_xTe$ might provides another strategy to look for the topological superconductor, that is, to artificially construct topological insulator/conventional superconductor heterostructures and make use of the superconducting proximity effect. In this case, both $Sn_{1-x}In_xTe$ and $(Pb_{1-x}Sn_x)_{1-y}In_yTe$ would be perfect systems to realize this purpose, since these materials undergo a continuous change from a TCI to a (likely conventional) superconductor.

In strongly correlated systems $La_{1.875}Ba_{0.125}CuO_{4+\delta}$ and $La_{1.75}Sr_{0.25}NiO_{4+\delta}$, inelastic neutron scattering was applied to explore the dynamic correlations. Although neither of them are three-dimensional high temperature superconductors, their ordered and static stripe phase simplified the studies on the dynamic correlations that are similar in the high temperature superconductors that we are really interested in. $La_{2-x}Ba_xCuO_{4+\delta}$ is a family of high temperature superconductors, but with 1/8 Ba-doping, the three-dimensional superconductivity is mostly suppressed due to the formation of ordered, static stripes. The static nature is caused by pinning due to the LTT-like tilting of the CuO_6 octahedra. In the disordered state, the tilting patterns above the LTO-LTT transition in the $La_{1.875}Ba_{0.125}CuO_{4+\delta}$ has been studied, and the results show that the dynamic LTT-like correlations exist even at high temperature. In the LTT phase, the octahedra has two kinds of tilting axis, either in [100] or [010]. When the temperature is low, these tilts remain static. As heating above the transition temperature, those tilts become vibrating. As a result, from a long-range view, or an averaged view such as probes like powder and single-crystal diffraction, the CuO_6 octahedra looks like tilting along the combined [110] direction. However, if we integrated a short-range of energy in the inelastic neutron scattering measurements, we observe the LTT-like tilts still exist, but become dynamic and extremely short-range, similar to the conclusions people obtained from powder-distribution-function and X-ray absorption fine structure analysis.

The $La_{2-x}Sr_xNiO_{4+\delta}$ has similar stripe structure as the high temperature cuprate superconductors except that their stripe orientation rotates 45 degree, and their insulating nature facilitates studying the dynamic charge stripes. In $La_{1.75}Sr_{0.25}NiO_{4+\delta}$, the observed inelastic scattering intensity associated with the charge-stripe fluctuations at high temperature is a sign of the existence of local-like stripe phase. In another word, usually we consider that above the stripe ordering temperature, the stripes get melted and then the materials should be no longer remain the stripe phase. But our results suggests that even when above the stripe ordering temperature, the local-like stripes become dynamic but still exist. The fluctuating charge order seems to be universal in both cuprates and iron based superconductors. Thus the fluctuations of charge order may provide an alternative to spin fluctuations as a underlying mechanism to understand the unconventional high temperature superconductivity. Besides, by mapping out the dispersion spectrum of the dynamic charge stripes the anisotropic low-energy dispersion above the stripe-ordering transition has been observed for the first time, providing evidence for the presence of electronic nematic order.

With our inelastic neutron experiments on these two materials, dynamic correlations related to high temperature superconductors are studies from two aspect: The first one is from the structural view, obtained from studying the LTT-like tilt fluctuations above the LTO-LTT transition in $La_{1.875}Ba_{0.125}CuO_{4+\delta}$. We known that by heating across the transition temperature, the LTT-like tilt correlations still exist, but become dynamic and extremely short-range. The second is from the electronic view, obtained from studying dynamic charge stripes above the stripe-ordering transition in $La_{1.75}Sr_{0.25}NiO_{4+\delta}$. In these two cases, we found that the correlations that was static and long-range at low temperature, doesn't disappear at high temperature. Instead, they exist locally and become dynamic. This makes us notice the universal phenomena in the strong correlated system: dynamic precursors of stripe formations appear far above the long-range ordering temperature.

ï£ij ï£ij